

REPORT ON PROGRESS

## Non-standard Hubbard models in optical lattices: a review

To cite this article: Omjyoti Dutta *et al* 2015 *Rep. Prog. Phys.* **78** 066001

View the [article online](#) for updates and enhancements.

### Related content

- [Physics of higher orbital bands in optical lattices: a review](#)

Xiaopeng Li and W Vincent Liu

- [Engineering novel optical lattices](#)

Patrick Windpassinger and Klaus Sengstock

- [The physics of dipolar bosonic quantum gases](#)

T Lahaye, C Menotti, L Santos et al.

### Recent citations

- [Fractional time crystals](#)

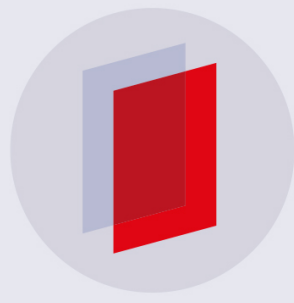
Pawel et al

- [Generalized effective-potential Landau theory for the two-dimensional extended Bose-Hubbard model](#)

Zhi Lin and Ming Yang

- [Phase structure of the interacting Su-Schrieffer-Heeger model and the relationship with the Gross-Neveu model on lattice](#)

Yoshihito Kuno



**IOP** | **ebooks**<sup>TM</sup>

Bringing you innovative digital publishing with leading voices to create your essential collection of books in STEM research.

Start exploring the collection - download the first chapter of every title for free.

## Reports on Progress

# Non-standard Hubbard models in optical lattices: a review

Omjyoti Dutta<sup>1</sup>, Mariusz Gajda<sup>2,3</sup>, Philipp Hauke<sup>4,5</sup>, Maciej Lewenstein<sup>6,7</sup>,  
Dirk-Sören Lühmann<sup>8</sup>, Boris A Malomed<sup>6,9</sup>, Tomasz Sowiński<sup>2,3</sup> and  
Jakub Zakrzewski<sup>1,10</sup>

<sup>1</sup> Instytut Fizyki imienia Mariana Smoluchowskiego, Uniwersytet Jagielloński, Łojasiewicza 11,  
30-348 Kraków, Poland

<sup>2</sup> Institute of Physics of the Polish Academy of Sciences, Al. Lotników 32/46, PL-02-668 Warsaw, Poland

<sup>3</sup> Center for Theoretical Physics of the Polish Academy of Sciences, Al. Lotników 32/46, PL-02-668  
Warsaw, Poland

<sup>4</sup> Institute for Quantum Optics and Quantum Information of the Austrian Academy of Sciences,  
A-6020 Innsbruck, Austria

<sup>5</sup> Institute for Theoretical Physics, Innsbruck University, A-6020 Innsbruck, Austria

<sup>6</sup> ICFO—Institut de Ciències Fotòniques, Mediterranean Technology Park, Av. C.F. Gauss 3,  
E-08860 Castelldefels (Barcelona), Spain

<sup>7</sup> ICREA—Institució Catalana de Recerca i Estudis Avançats, Lluís Company 23, E-08011 Barcelona,  
Spain

<sup>8</sup> Institut für Laser-Physik, Universität Hamburg, Luruper Chaussee 149, 22761 Hamburg, Germany

<sup>9</sup> Department of Physical Electronics, School of Electrical Engineering, Faculty of Engineering,  
Tel Aviv University, Tel Aviv 69978, Israel

<sup>10</sup> Mark Kac Complex Systems Research Center, Jagiellonian University, ul. Łojasiewicza 11,  
30-348 Kraków, Poland

E-mail: [Jakub.Zakrzewski@uj.edu.pl](mailto:Jakub.Zakrzewski@uj.edu.pl)

Received 12 June 2014, revised 23 October 2014

Accepted for publication 18 December 2014

Published 28 May 2015



CrossMark

## Abstract

Originally, the Hubbard model was derived for describing the behavior of strongly correlated electrons in solids. However, for over a decade now, variations of it have also routinely been implemented with ultracold atoms in optical lattices, allowing their study in a clean, essentially defect-free environment. Here, we review some of the vast literature on this subject, with a focus on more recent non-standard forms of the Hubbard model. After giving an introduction to standard (fermionic and bosonic) Hubbard models, we discuss briefly common models for mixtures, as well as the so-called extended Bose–Hubbard models, that include interactions between neighboring sites, next-neighbor sites, and so on. The main part of the review discusses the importance of additional terms appearing when refining the tight-binding approximation for the original physical Hamiltonian. Even when restricting the models to the lowest Bloch band is justified, the standard approach neglects the density-induced tunneling (which has the same origin as the usual on-site interaction). The importance of these contributions is discussed for both contact and dipolar interactions. For sufficiently strong interactions, the effects related to higher Bloch bands also become important even for deep optical lattices. Different approaches that aim at incorporating these effects, mainly via dressing the basis, Wannier functions with interactions, leading to effective, density-dependent Hubbard-type models, are reviewed. We discuss also examples of Hubbard-like models that explicitly involve higher  $p$  orbitals, as well as models that dynamically couple spin and orbital degrees of freedom. Finally, we review mean-field nonlinear Schrödinger models of the

Salerno type that share with the non-standard Hubbard models nonlinear coupling between the adjacent sites. In that part, discrete solitons are the main subject of consideration. We conclude by listing some open problems, to be addressed in the future.

Keywords: Hubbard model, optical lattices, ultracold atoms

(Some figures may appear in colour only in the online journal)

## 1. Introduction

### 1.1. Hubbard models

Hubbard models are relatively simple, yet complex enough, lattice models of theoretical physics, capable of providing a description of strongly correlated states of quantum many-body systems. Quoting Wikipedia<sup>11</sup>: *the Hubbard model is an approximate model used, especially in solid state physics, to describe the transition between conducting and insulating systems. The Hubbard model, named after John Hubbard, is the simplest model of interacting particles in a lattice, with only two terms in the Hamiltonian (Hubbard 1963): a kinetic term allowing for tunneling ('hopping') of particles between sites of the lattice and a potential term consisting of an on-site interaction. The particles can be either fermions, as in Hubbard's original work, or bosons, when the model is referred to as the 'Bose-Hubbard model' or the boson Hubbard model.* Let us note that the lattice model for bosons was first derived by Gersch and Knollman (1963), prior to the derivation of Hubbard's fermionic counterpart.

The Hubbard model is a good approximation for particles in a periodic potential at sufficiently low temperatures. All the particles are then in the lowest Bloch band, as long as any long-range interactions between the particles can be ignored. If interactions between particles on different sites of the lattice are included, the model is often referred to as the 'extended Hubbard model'.

John Hubbard introduced the Fermi–Hubbard models in 1963 to describe electrons, i.e. spin 1/2 fermions in solids. The model has been intensively studied, although there are no really efficient methods for simulating it numerically in dimensions greater than 1. Because of this complexity, various calculational methods, for instance using exact diagonalization, perturbative expansions, mean-field/pairing theory, mean-field/cluster expansions, slave boson theory, fermionic quantum Monte Carlo approaches (Troyer and Wiese 2005, Lee *et al* 2006, Lee 2008), or the more recently presented tensor network approaches (see Corboz *et al* 2010a, 2010b and references therein), lead to contradicting quantitative, and even qualitative, results. Only the one-dimensional Fermi–Hubbard model is analytically soluble with the help of the Bethe ansatz (Essler *et al* 2005). The 2D Fermi–Hubbard model, or, better stated, a weakly coupled array of 2D Fermi–Hubbard models, is at the center of interest in contemporary condensed-matter physics, since it is believed to describe the high temperature superconductivity of cuprates. At the end of the last century, the studies of various kinds of Hubbard models intensified

enormously, due to the developments in the physics of ultracold atoms, ions, and molecules.

### 1.2. Ultracold atoms in optical lattices

The studies of ultracold atoms constitute one of the hottest areas of atomic, molecular, and optical (AMO) physics and quantum optics. They have been rewarded with the 1997 Nobel Prize in physics for Chu (1998), Cohen-Tannoudji (1998) and Phillips (1998) for laser cooling, and the 2001 Nobel Prize for Cornell and Wieman (2002) and Ketterle (2002) for the first observation of the Bose–Einstein condensation (BEC). All of these developments, despite their indisputable importance and beauty, concern the physics of weakly interacting systems. Many AMO theoreticians working in this area suffered from the (unfortunately to some extent justified) criticism from their condensed-matter colleagues that 'all of that was known before'. The recent progress in this area, however, is by no means less spectacular. Particularly impressive are recent advances in the studies of ultracold gases in optical lattices. Optical lattices are formed from several laser beams in standing wave configurations. They provide practically ideal, loss-free potentials, in which ultracold atoms may move and interact with one another (Grimm *et al* 2000, Windpassinger and Sengstock 2013). In 1998, a theoretical paper of Jaksch and co-workers Jaksch *et al* (1998), following the seminal work by condensed-matter theorists (Fisher *et al* 1989), showed that ultracold atoms in optical lattices may enter the regime of strongly correlated systems, and exhibit a so-called superfluid-Mott insulator quantum phase transition. The subsequent experiment at the Ludwig-Maximilian Universität in Munich confirmed this prediction, and in this manner the physics of ultracold atoms got an invitation to the 'High Table'—the frontiers of modern condensed-matter physics and quantum field theory. Nowadays it is routinely possible to create systems of ultracold bosonic or fermionic atoms, and their mixtures, in one-, two-, or three-dimensional optical lattices in strongly correlated states (Auerbach 1994), i.e. states in which genuine quantum correlations, such as entanglement, extend over large distances (for recent reviews see Bloch *et al* 2008, Giorgini *et al* 2008, Lewenstein *et al* 2007, 2012). Generic examples of such states are found when the system in question undergoes a so-called quantum phase transition (Sachdev 1999). The transition from the Bose superfluid (where all atoms form a macroscopic coherent wave packet that is spread over the entire lattice) to the Mott insulator state (where a fixed number of atoms are localized in every lattice site) is a paradigmatic example of such a quantum phase transition. While the systems observed in experiments, such

<sup>11</sup> <http://en.wikipedia.org/> as of 30 May 2014

as that of Greiner *et al* (2002), are of finite size, and are typically confined in some trapping potential, hence they may not exhibit a critical behavior in the rigorous sense, there is no doubt about their strongly correlated nature.

### 1.3. Ultracold matter and quantum technologies

The unprecedented control and precision with which one can engineer ultracold gases inspired many researchers to consider such systems as possible candidates for implementing quantum technologies—in particular, quantum information processing and high precision metrology. In the 1990s, the main effort of the community was directed towards the realization of a universal scalable quantum computer, stimulated by the seminal work of Cirac and Zoller (1995), who proposed the first experimental realization of a universal two-qubit gate with trapped ions. In order to follow a similar approach with atoms, one would first choose specific states of atoms, or groups of atoms, as states of qubits (two-level systems), or qudits (elementary systems with more than two internal quantum states). The second step would then consist in implementing quantum logical gates on the single-qubit and two-qubit level. Finally, one would aim at implementing complete quantum protocols and quantum error correction in such systems by employing interatomic interactions and/or interactions with external (electric, magnetic, laser) fields. Perhaps the first paper presenting such a vision with the atoms proposed, in fact, was realized in quantum computing using ultracold atoms in an optical lattice (Jaksch *et al* 1999). It is also worth stressing that the pioneering paper of Jaksch *et al* (1998) was motivated by the quest for quantum computing: the transition to a Mott insulator state was supposed to be, in this context, an efficient way of preparing a quantum register with a fixed number of atoms per site.

In recent years, however, it became clear that while universal quantum computing is still elusive, another approach to quantum computing, suggested by Feynman *et al* (1986), may already now be realized with ultracold atoms and ions in laboratories. This approach employs these highly controllable systems as quantum computers with special purposes, or, in other words, as quantum simulators (Jaksch and Zoller 2005). There has been considerable interest recently to both of these approaches both in theory and experiment. In particular, it has been widely discussed that ultracold atoms, ions, photons, or superconducting circuits could serve as quantum simulators of various types of the Bose–Hubbard or Fermi–Hubbard models and related lattice spin models (Aspuru-Guzik and Walther 2012, Blatt and Roos 2012, Bloch *et al* 2012, Cirac and Zoller 2004, 2012, Houck *et al* 2012, Jaksch and Zoller 2005, Lewenstein *et al* 2007, 2012, Hauke *et al* 2012a). The basic idea of quantum simulators can be condensed into four points (see, e.g. Hauke *et al* 2012a):

- A quantum simulator is an experimental system that mimics a simple model, or a family of simple models, of condensed-matter physics, high energy physics, quantum chemistry etc.

- The simulated models have to be of some relevance for applications and/or our understanding of the challenges of contemporary physics.
- The simulated models should be computationally very hard for classical computers. Exceptions from this rule are possible for quantum simulators that exhibit novel, so far only theoretically predicted, phenomena.
- A quantum simulator should allow for a broad control of the parameters of the simulated model, and for control of the preparation, manipulation, and detection of states of the system. It should allow for validation (calibration)!

Practically all Hubbard models can hardly be simulated at all by classical computers for very large systems; at least some of them are hard to simulate even for moderate system sizes due to the lack of scalable classical algorithms, caused for instance by the infamous sign problem in quantum Monte Carlo (QMC) codes, or complexity caused by disorder. These Hubbard models describe a variety of condensed-matter systems (but not only these), and thus are directly related to challenging problems of modern condensed-matter physics, concerning for instance high temperature superconductivity (see Lee 2008), Fermi superfluids (see Bloch *et al* 2008, Giorgini *et al* 2008), and lattice gauge theories and quark confinement (Montvay and Münster 1997) (for recent works in the area of ultracold atoms and lattice gauge theories, see Banerjee *et al* 2013, Tagliacozzo *et al* 2013a,b, Wiese 2013 and Zohar *et al* 2013). The family of Hubbard models thus easily satisfies the relevance and hardness criteria mentioned above, moving them into the focus of attempts at building quantum simulators. For these reasons, a better understanding of the experimental feasibility of quantum simulation of Hubbard models is of great practical and technological importance.

### 1.4. Beyond standard Hubbard models

As a natural first step, one would like to realize standard Bose–Hubbard and Fermi–Hubbard models, i.e. those models that have only a kinetic term and one type of interaction, as mentioned in the introduction. The static properties of the Bose–Hubbard model are accessible to QMC simulations, but only for systems that are not too large and not too cold, while the out-of-equilibrium dynamics of this model can only be computed efficiently for short times. The case of the Fermi–Hubbard model is even more difficult: here neither static nor dynamical properties can be simulated efficiently, even for moderate system sizes. These models are thus paradigm examples of systems that can be studied by means of quantum simulations with ultracold atoms in optical lattices (Lewenstein *et al* 2007), provided that they can be realized with sufficient precision and control in laboratories.

Interestingly, however, many Hubbard models that are simulated with ultracold atoms do not have a standard form; the corresponding Hamiltonians frequently contain terms that include correlated and occupation-dependent tunnelings within the lowest band, as well as correlated tunnelings and

occupation of higher bands. These effects have been observed in the past decade in many different experiments, concerning:

- observations of density-induced tunneling (Meinert *et al* 2013, Jürgensen *et al* 2014);
- shift of the Mott transition in Fermi–Bose mixtures (Ospelkaus *et al* 2006a, Günter *et al* 2006, Best *et al* 2009, Heinze *et al* 2011);
- a Mott insulator in the bosonic system (Mark *et al* 2011);
- modifications of on-site interactions (Campbell *et al* 2006, Will *et al* 2010, Bakr *et al* 2011, Mark *et al* 2011, Mark *et al* 2012, Uehlinger *et al* 2013);
- effects of excited bands (Browaeys *et al* 2005, Köhl 2005, Anderlini *et al* 2007, Müller *et al* 2007, Wirth *et al* 2010, Ölschläger *et al* 2011, Ölschläger *et al* 2012, Ölschläger *et al* 2013);
- dynamical spin effects (Pasquiou *et al* 2010, 2011, de Paz *et al* 2013a, 2013b).

One can view these non-standard terms in two ways: as an obstacle, or as an opportunity. On one hand, one has to be careful in attempts to quantum simulate standard Hubbard models. On the other hand, non-standard Hubbard models are extremely interesting by themselves: they exhibit novel exotic quantum phases, quantum phase transitions, and other quantum properties. Quantum simulating these features is itself a formidable task! Since such models are now within experimental reach, it is necessary to study and understand them in order to describe experimental findings and make new predictions for ultracold quantum gases. For this reason, there has been quite a bit of progress in such studies in recent years, and this is the main motivation for this review.

Our paper is organized as follows. Before we explain what the non-standard Hubbard models considered are, we discuss briefly the form and variants of standard and standard extended Hubbard models in section 2. In section 3 we present the main *dramatis personae* of this review: non-standard single-band and non-single-band Hubbard models. The section starts with a short historical glimpse describing models introduced in the 1980s by Hirsch and others. All of the models discussed here have the form of single-band models, in the sense that the effect of higher bands is included in an effective manner, for instance through many-body modifications of the Wannier functions describing single-particle states at a given lattice site. In contrast, the non-standard models considered in section 4 include explicit contributions of excited bands, which, however, at least in some situations, can still be cast within ‘effective single-band models’ cases (for instance, via appropriate modifications of the Wannier functions).

Section 5 deals with p band Hubbard models, while section 6 deals with Hubbard models appearing in the theory of ultracold dipolar gases and the phenomenon of the Einstein–de Haas effect. Section 7 is devoted to mean-field versions of non-standard Hubbard models, and in particular to various kinds of exotic solitons that can be generated in such systems. We conclude our review in section 8, pointing out some of the open problems.

Let us also mention some topics that *will not* be discussed in this review, primarily to keep it within reasonable bounds. We

consider extended optical lattices and do not discuss double-well or triple-well systems where interaction-induced effects are also important (for a recent example, see Xiong and Fischer 2013). We also do not go into the rapidly developing subject of modifications to Hubbard models by externally induced couplings. These may lead to the creation of artificial gauge fields or spin–orbit interactions via e.g. additional laser (for recent reviews, see Dalibard *et al* 2011, Goldman *et al* 2013) or microwave (Struck *et al* 2014) couplings. Fast periodic modulations of different Hamiltonian parameters (lattice positions or depth, or interactions) may lead to effective, time-averaged Hamiltonians with additional terms altering Hubbard models (see e.g. Eckardt *et al* 2010, 2005, Hauke *et al* 2012b, Liberto *et al* 2014, Lignier *et al* 2007, Rapp *et al* 2012, Struck *et al* 2011). Still faster modulations may be used to resonantly couple the lowest Bloch band with the excited ones, opening up additional experimental possibilities (Sowiński 2012, Łącki and Zakrzewski 2013, Dutta *et al* 2014, Straeter and Eckardt 2014, Goldman *et al* 2014, Przysiezna *et al* 2015).

## 2. Standard Hubbard models based on optical lattices

Before we turn to the discussion of non-standard Hubbard models, let us first establish clearly what we mean by standard ones. We start this section by discussing a weakly interacting Bose gas in an optical lattice, and derive the discrete Gross–Pitaevskii, i.e. discrete nonlinear Schrödinger, equation describing such a situation. Subsequently, we give a short description of Bose–Hubbard and Fermi–Hubbard models and their basic properties. These models allow the treatment of particles in the strongly correlated regime. Finally, we discuss the *extended* Hubbard models with nearest-neighbor, next-nearest-neighbor interactions, etc, which provide a standard basis for the treatment of dipolar gases in optical lattices.

### 2.1. Weakly interacting particles: the nonlinear Schrödinger equation

We start by providing a description of a weakly interacting Bose–Einstein condensate placed in an optical lattice. The many-body Hamiltonian in the second-quantization formalism describing a gas of  $N$  interacting bosons in an external potential,  $V_{\text{ext}}$ , reads

$$\hat{H}(t) = \int d\mathbf{r} \hat{\Psi}^\dagger(\mathbf{r}, t) \left[ -\frac{\hbar^2}{2m} \nabla^2 + V_{\text{ext}} \right] \hat{\Psi}(\mathbf{r}, t) + \frac{1}{2} \int d\mathbf{r} d\mathbf{r}' \hat{\Psi}^\dagger(\mathbf{r}, t) \hat{\Psi}^\dagger(\mathbf{r}', t) V(\mathbf{r} - \mathbf{r}') \hat{\Psi}(\mathbf{r}, t) \hat{\Psi}(\mathbf{r}', t), \quad (1)$$

where  $\hat{\Psi}$  and  $\hat{\Psi}^\dagger$  are the bosonic annihilation and creation field operators, respectively. Interactions between atoms are given by an isotropic short-range pseudopotential modeling s wave interactions (Bloch *et al* 2008):

$$V(\mathbf{r} - \mathbf{r}') = \frac{4\pi\hbar^2 a_s}{m} \delta(\mathbf{r} - \mathbf{r}') \frac{\partial}{\partial |\mathbf{r} - \mathbf{r}'|} |\mathbf{r} - \mathbf{r}'| \quad (2)$$

Here,  $m$  is the atomic mass and  $a_s$  the s wave scattering length that characterizes the interactions—attractive (repulsive) for negative (positive)  $a_s$ —through elastic binary collisions at low energies between neutral atoms, independently of the actual interparticle two-body potential. This is due to the fact that for ultracold atoms the de Broglie wavelength is much larger than the effective extension of the interaction potential, implying that the interatomic potential can be replaced by a pseudopotential. For non-singular  $\hat{\Psi}(\mathbf{r}, t)$ , the pseudopotential is equivalent to a contact potential of the form

$$V(\mathbf{r} - \mathbf{r}') = (4\pi\hbar^2 a_s / m) \delta(\mathbf{r} - \mathbf{r}') = g\delta(\mathbf{r} - \mathbf{r}'). \quad (3)$$

Note that this approximation is valid provided that no long-range contributions exist (later we shall consider modifications due to long-range dipolar interactions)—for more details about scattering theory see for instance (Landau and Lifshitz 1987, Gribakin and Flambaum 1993).

If the bosonic gas is dilute,  $na_s^3 \ll 1$ , where  $n$  is the density, the mean-field description applies, the basic idea of which was formulated by Bogoliubov (1947). It consists in writing the field operator in the Heisenberg representation as a sum of its expectation value (the condensate wavefunction) plus a fluctuating field operator:

$$\hat{\Psi}(\mathbf{r}, t) = \Psi(\mathbf{r}, t) + \delta\hat{\Psi}(\mathbf{r}, t). \quad (4)$$

When classical and quantum fluctuations are neglected, the time evolution of the condensate wavefunction at temperature  $T = 0$  is governed by the Gross–Pitaevskii equation (GPE) (Gross 1961, Pitaevskii 1961, Pitaevskii and Stringari 2003), obtained by using the Heisenberg equations and equation (4):

$$i\hbar \frac{d}{dt} \Psi(\mathbf{r}, t) = -\frac{\hbar^2}{2m} \nabla^2 \Psi(\mathbf{r}, t) + [V_{\text{ext}} + g|\Psi(\mathbf{r}, t)|^2] \Psi(\mathbf{r}, t). \quad (5)$$

The wavefunction of the condensate is normalized to the total number of particles  $N$ . Here we will consider the situation in which the external potential corresponds to an optical lattice, combined with a weak harmonic trapping potential.

A BEC placed in an optical lattice can be described in the so-called tight-binding approximation if the lattice depth is sufficiently large, such that the barrier between the neighboring sites is much higher than the chemical potential and the energy of the system is confined within the lowest band. This approximation corresponds to decomposing the condensate order parameter  $\Psi(\mathbf{r}, t)$  as a sum of wavefunctions  $\Theta(\mathbf{r} - \mathbf{R}_i)$  localized at each site of the periodic potential:

$$\Psi(\mathbf{r}, t) = \sqrt{N} \sum_i \varphi_i \Theta(\mathbf{r} - \mathbf{R}_i), \quad (6)$$

where  $\varphi_i = \sqrt{n_i(t)} e^{i\phi_i(t)}$  is the amplitude of the  $i$ th lattice site with  $n_i = N_i/N$  and  $N_i$  is the number of particles at the  $i$ th site. Introducing the ansatz given by equation (6) into equation (5) (Trombettoni and Smerzi 2001), one obtains the discrete nonlinear Schrödinger (DNLS) equation, which in its standard form reads

$$i\hbar \frac{\partial \varphi_i}{\partial t} = -K(\varphi_{i-1} - \varphi_{i+1}) + (\epsilon_i + U|\varphi_i|^2)\varphi_i, \quad (7)$$

where  $K$  denotes the next-neighbor tunneling rate:

$$K = - \int d\mathbf{r} \left[ \frac{\hbar^2}{2m} \nabla \Theta_i \cdot \nabla \Theta_{i+1} + \Theta_i V_{\text{ext}} \Theta_{i+1} \right]. \quad (8)$$

The on-site energies are given by

$$\epsilon_i = \int d\mathbf{r} \left[ \frac{\hbar^2}{2m} (\nabla \Theta_i)^2 + V_{\text{ext}} \Theta_i^2 \right], \quad (9)$$

and the nonlinear coefficient by

$$U = gN \int d\mathbf{r} \Theta_i^4. \quad (10)$$

Here we have only reviewed the lowest order DNLS equation. Nevertheless, it has been shown (Trombettoni and Smerzi 2003) that the effective dimensionality of the BECs trapped at each site can modify the degree of nonlinearity and the tunneling rate in the DNLS equation. We will come back to the DNLS equation and its non-standard forms in section 7.

## 2.2. The Bose–Hubbard model

In the strongly interacting regime, bosonic atoms in a periodic lattice potential are well described by a Bose–Hubbard Hamiltonian (Fisher *et al* 1989, for a recent review see Krutitsky 2015). In this section, we explain how the Bose–Hubbard Hamiltonian can be derived from the many-body Hamiltonian in second quantization (1) by expressing the fields through the single-particle Wannier modes. To be specific, we shall assume from now on a separable 3D lattice potential of the form

$$V_{\text{ext}} = \sum_{l=x,y,z} V_{0l} \sin^2(\pi l/a), \quad (11)$$

for which the Wannier functions are the products of one-dimensional standard Wannier functions (Kohn 1959). In equation (11),  $a$  plays the role of the lattice constant (and is equal to half the wavelength of the lasers forming the standing wave pattern). By appropriately arranging the directions and relative phases of the laser beams, much richer lattice structures may be achieved (Windpassinger and Sengstock 2013), such as the celebrated triangular or kagome lattices. The corresponding Wannier functions may then be found following the approach developed by Marzari *et al* (2012) and Marzari and Vanderbilt (1997). We shall, however, not consider here different geometrical aspects of possible optical lattices, but rather concentrate on the interaction-induced phenomena. Similarly, we do not discuss phenomena that are induced by next-nearest-neighbor tunnelings.

Let us start by reminding the reader of the handbook approach (Ashcroft and Mermin 1976). The field operators can always be expanded in the basis of Bloch functions, which are the eigenfunctions of the single-particle Hamiltonian consisting of the kinetic term and the periodic lattice potential:

$$\hat{\Psi}(\mathbf{r}) = \sum_{n,k} \hat{b}_{n,k} \phi_{n,k}(\mathbf{r}). \quad (12)$$

The Bloch functions have indices denoting the band number  $n$  and the quasi-momentum  $k$ . For sufficiently deep optical

potentials, and at low temperatures, the band gap between the lowest and the first excited band may be large enough that the second and higher bands will be practically unpopulated and can be disregarded. Within the lowest Bloch band of the periodic potential (11) the field operators may be expanded into an orthonormal Wannier basis, consisting of functions localized around the lattice sites. More precisely, the Wannier functions have the form  $w_i(\mathbf{r}) = w(\mathbf{r} - \mathbf{R}_i)$ , with  $\mathbf{R}_i$  corresponding to the minima of the lattice potential (Jaksch *et al* 1998):

$$\hat{\Psi}(\mathbf{r}) = \sum_i \hat{b}_i w_i(\mathbf{r}). \quad (13)$$

This expansion (known as the tight-binding approximation) makes sense because the temperature is sufficiently low, and because the typical interaction energies are not strong enough to excite higher vibrational states. Here,  $\hat{b}_i$  ( $\hat{b}_i^\dagger$ ) denote the annihilation (creation) operators of a particle localized at the  $i$ th lattice site, which obey canonical commutation relations  $[\hat{b}_i, \hat{b}_j^\dagger] = \delta_{ij}$ . The impact of higher bands in multi-orbital Hubbard models is discussed in section 4, whereas the situation where particles are confined in a single higher band of the lattice is addressed in section 5. Introducing the above expansion into the Hamiltonian given in equation (1), one obtains

$$\hat{H} = - \sum_{\langle i,j \rangle} t_{ij} \hat{b}_i^\dagger \hat{b}_j + \frac{U}{2} \sum_i \hat{n}_i (\hat{n}_i - 1) - \mu \sum_i \hat{n}_i, \quad (14)$$

where  $\langle , \rangle$  indicates the sum over nearest neighbors (note that each  $i, j$  pair appears twice in the summation, ensuring Hermiticity of the first term). Further,  $\hat{n}_i = \hat{b}_i^\dagger \hat{b}_i$  is the boson number operator at site  $i$ . In the above expression,  $\mu$  denotes the chemical potential, which is introduced to control the total number of atoms. In the standard approach, among all terms arriving from the expansion in the Wannier basis, only tunneling between nearest neighbors is considered and only interactions between particles on the same lattice site are retained. Note that this may not be a good approximation for shallow lattices (Trotzky *et al* 2012). Another way of looking at this problem is to realize that for sufficiently shallow lattice potentials, the lowest band will not have a cosine-like dispersion, and hence the single-band tight-binding approximation (as introduced above) will not be valid. The matrix element for tunneling between adjacent sites is given by

$$t_{ij} = - \int d\mathbf{r} w_i^*(\mathbf{r}) \left[ \frac{-\hbar^2 \nabla^2}{2m} + V_{\text{ext}} \right] w_j(\mathbf{r}). \quad (15)$$

The subscript  $(ij)$  can be omitted in the homogeneous case, when the external optical potential is isotropic and tunneling is the same along any direction. For a contact potential, the strength of the two-body on-site interactions  $U$  reduces to

$$U = g \int d\mathbf{r} |w_i(\mathbf{r})|^4. \quad (16)$$

If an external potential  $V_{\text{ext}}$  accounts also for a trapping potential  $V_T$ , an additional term in the Bose–Hubbard Hamiltonian appears, accounting for the potential energy:

$$\hat{H}_{\text{ext}} = \sum_i \epsilon_i n_i, \quad (17)$$

with  $\epsilon_i$  given by

$$\epsilon_i = \int d\mathbf{r} V_T |w_i(\mathbf{r})|^2 \approx V_T(\mathbf{R}_i). \quad (18)$$

This term describes an energy offset for each lattice site; typically it is absorbed into a site-dependent chemical potential:  $\mu_i = \mu + \epsilon_i$ .

Within the harmonic approximation (i.e. the approximation in which the on-site potential is harmonic and the Wannier functions are Gaussian), it is possible to obtain analytical expressions for the integrals above. While this approximation may provide qualitative information, often, even for deep lattices, an exact expansion in Wannier functions provides much better quantitative results, in the sense that the tight-binding model represents more closely the real physics in continuous space. The harmonic approximation underestimates tunneling amplitudes due to assuming Gaussian tails of the wavefunctions, as compared with the real exponential tails of Wannier functions. As we shall see later in sections 5 and 6, the two approaches may lead to qualitatively different physics for excited bands also. For the same reason, even in the mean-field DNLS approach, discussed in section 2.1, it is desirable to use Wannier functions in place of the localized  $\Theta$  functions introduced there.

The Bose–Hubbard Hamiltonian, equation (14), exhibits two different quantum phases depending on the ratio between the tunneling energy and the on-site repulsion energy: (i) a superfluid, compressible, gapless phase, when tunneling dominates, and (ii) an incompressible, Mott insulator ground state, when the on-site interaction dominates. Detailed discussions of methods of analysis (based on various kinds of mean-field approaches, quantum Monte Carlo methods, strong coupling expansions, DMRG, exact diagonalizations, etc) as well as the properties of this standard model have been often reviewed (Zwerger 2003, Lewenstein *et al* 2007, Lewenstein *et al* 2012, Bloch *et al* 2008, Cazalilla *et al* 2011). In particular, for high order expansions see Elstner and Monien (1999) and Damski and Zakrzewski (2006), while for the most recent works on this model see e.g. Carrasquilla *et al* (2013) and Łącki *et al* (2014).

Lastly, another generalization of the Bose–Hubbard model was recently elaborated by Barbiero *et al* (2014): the one with the strength of the on-site repulsion,  $U$ , growing faster than  $|i|$  from the center to periphery. Similar to the result previously reported in the mean-field counterpart of the so modified system (the discrete nonlinear Schrödinger equation) by Gligorić *et al* (2013), which, in turn, followed a similar concept elaborated in continuous mean-field models in Borovkova *et al* (2011), the spatially growing *self-repulsion* strength leads to self-trapping of *bright* quantum solitons in the Bose–Hubbard lattice.

### 2.3. The Fermi–Hubbard model

This section, describing the Hubbard model for a trapped gas of interacting spin 1/2 fermions, follows to a great extent the recent reviews of Bloch *et al* (2008), Giorgini *et al* (2008), Lee

(2008) and Radzhivsky and Sheehy (2010). The starting point is again a quantum field theory model similar to (1), reading

$$\hat{H}_F = \int d\mathbf{r} \left[ \sum_{\sigma} \hat{\psi}_{\sigma}^{\dagger} \left( -\frac{\hbar^2}{2m} \nabla^2 + V_{\text{ext}} \right) \hat{\psi}_{\sigma} + g(\hat{\psi}_{\downarrow}^{\dagger} \hat{\psi}_{\uparrow}^{\dagger} \hat{\psi}_{\uparrow} \hat{\psi}_{\downarrow}) \right], \quad (19)$$

where  $\sigma = \{\uparrow, \downarrow\}$  denotes the spin, and the field operators obey fermionic anticommutation relations:  $\{\hat{\psi}(\mathbf{r})_{\sigma}, \hat{\psi}^{\dagger}(\mathbf{r}')_{\sigma'}\} = \delta_{\sigma\sigma'} \delta(\mathbf{r} - \mathbf{r}')$ . As previously done for bosons, applying a standard tight-binding approximation, the electronic (or for us atomic spin 1/2) Fermi–Hubbard model is obtained with the Hamiltonian

$$\hat{H} = - \sum_{\langle i,j \rangle, \sigma} t_{ij} \hat{f}_{i\sigma}^{\dagger} \hat{f}_{j\sigma} + \frac{U}{2} \sum_i \hat{f}_{i\uparrow}^{\dagger} \hat{f}_{i\downarrow}^{\dagger} \hat{f}_{i\downarrow} \hat{f}_{i\uparrow} - \mu \sum_{i, \sigma} \hat{f}_{i\sigma}^{\dagger} \hat{f}_{i\sigma}, \quad (20)$$

where  $\hat{f}_{i\sigma}^{\dagger}$  ( $\hat{f}_{i\sigma}$ ) is the creation (annihilation) operator for  $\sigma$  fermions at site  $i$  and  $\mu$  is the chemical potential. This model has fundamental importance for the theory of conducting electrons (or fermions in general).

The BCS theory of superconductivity is essentially a theory of pairing, or a theory of Gaussian fermionic states. For weak interactions, when  $U \ll t$  (assuming that  $t_{ij} = t$  for simplicity), one can replace the quartic interaction term in the Hamiltonian by a ‘Wick-averaged’ bilinear term:

$$U \sum_i \hat{f}_{i\uparrow}^{\dagger} \hat{f}_{i\downarrow}^{\dagger} \hat{f}_{i\downarrow} \hat{f}_{i\uparrow} \simeq (\Delta_i \hat{f}_{i\uparrow}^{\dagger} \hat{f}_{i\downarrow}^{\dagger} + \Delta_i^* \hat{f}_{i\downarrow} \hat{f}_{i\uparrow} + W_{i\downarrow} \hat{f}_{i\uparrow}^{\dagger} \hat{f}_{i\uparrow} \\ + W_{i\uparrow} \hat{f}_{i\downarrow}^{\dagger} \hat{f}_{i\downarrow} - V_{i\uparrow} \hat{f}_{i\uparrow}^{\dagger} \hat{f}_{i\downarrow} - V_{i\downarrow}^* \hat{f}_{i\downarrow}^{\dagger} \hat{f}_{i\uparrow}), \quad (21)$$

where  $\Delta_i = U \langle \hat{f}_{i\downarrow} \hat{f}_{i\uparrow} \rangle$ ,  $W_{i\sigma} = U \langle \hat{f}_{i\sigma}^{\dagger} \hat{f}_{i\sigma} \rangle$ , and  $V_i^* = U \langle \hat{f}_{i\downarrow}^{\dagger} \hat{f}_{i\uparrow} \rangle$  and  $\langle \dots \rangle$  denotes a quantum average. The further steps are straightforward. For  $T = 0$  the ground state of the bilinear Hamiltonian (20) is easily obtained by diagonalization. Next, we calculate the ground state averages of  $\Delta_i$ ,  $W_{i\sigma}$ , and  $V_i$ , and obtain in this way self-consistent, highly nonlinear equations for these quantities. Typically, they have to be then treated numerically. Similarly, for  $T > 0$  the averages have to be performed with respect to the quantum Boltzmann–Gibbs state, i.e. the thermal canonical state, or, even better, the grand canonical state.

Cuprates were the first high temperature superconductors discovered, and all of them have a layered structure, consisting typically of several oxygen–copper planes (see figure 1). So far, there has been no consensus reached concerning mechanisms and the nature of high  $T_c$  superconductivity. Nevertheless, many researchers believe that the Hubbard model can provide important insights which can help with understanding the high  $T_c$  superconductivity of cuprates.

Consider again the Hubbard Hamiltonian (20). The matrix element  $t_{ij}$  for hopping between sites  $i$  and  $j$  is in principle not restricted to the nearest neighbors. We denote nearest-neighbor hopping by  $t$  and further-neighbor hoppings by  $t'$ ,  $t''$ , and so on. At half-filling (one electron per site) the system undergoes a metal-insulator transition as the ratio  $U/t$  is increased. The insulator is the Mott insulator (Mott 1949) that we met already for bosons. There is exactly one particle per site, and

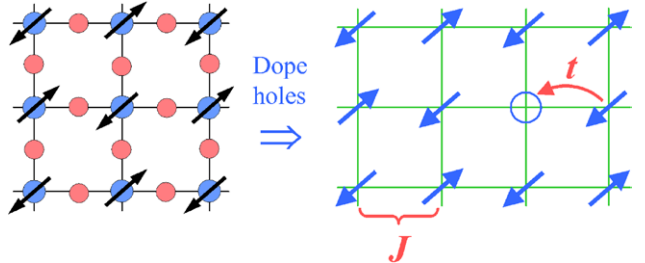


**Figure 1.** Schematics of a Cu–O layer (on the left) forming a typical cuprate. Copper atoms sit on a square lattice with oxygen atoms in between. One-band model with electron hopping rate  $t$  (on the right) corresponding to the simplified electronic structure.  $J$  denotes the antiferromagnetic super-exchange between spins on neighboring sites. Reprinted figure, with permission, from Lee *et al* (2006). Copyright (2006) by the American Physical Society.

this effect is caused solely by strong repulsion. This is in contrast to the case for a band insulator, which has two electrons of opposite spin per site, and cannot have more in the lowest band due to the Pauli exclusion principle. For large enough  $U/t$ , fermions remain localized at the lattice sites, because any hopping leads to a double occupation of some site, with a large energy cost  $U$ . The fermionic Mott insulator is additionally predicted to be antiferromagnetic (AF), because the AF alignment permits virtual hopping to gain a super-exchange energy  $J = 4t^2/U$ , whereas for parallel spins, hopping is strictly forbidden by Pauli exclusion. The fermionic MI was realized in beautiful experiments (Jördens *et al* 2008, Schneider *et al* 2008), while the forming of an AF state seems to be very close to an experimental realization—see the experiments in the R Hulet (Mathy *et al* 2012) and T Esslinger (Greif *et al* 2013, Imrisha *et al* 2014) groups. Importantly, the first fermionic MI in 2D was also realized recently (Uehlinger *et al* 2013).

Electron vacancies (holes) can be introduced into the copper–oxygen layers in a process called hole doping—leading to even more complex and interesting physics. In condensed matter, doping is typically realized by introducing a charge reservoir away from the copper–oxygen planes, such that it removes electrons from the plane. For ultracold atoms the number of ‘spin-up’ and ‘spin-down’ atoms can be controlled independently. Thus, in principle one can easily mimic the effect of doping, although in the presence of the confining harmonic potential it is difficult to achieve homogeneous doping in a well controlled way. One can circumvent this problem for repulsive Fermi–Bose mixtures. In such mixtures, composite fermions consisting of a fermion (of spin up or down) and a bosonic hole may form, and their number can be controlled by adding bare bosons to the system (Eckardt and Lewenstein 2010).

Figure 2 presents the schematic phase diagram that results from hole doping in the plane spanned by temperature  $T$  and hole concentration  $x$ . At low  $x$  and low  $T$ , the AF order is stable. With increasing  $x$ , the AF order is rapidly destroyed by a few per cent of holes. For even larger  $x$ , a superconducting phase appears, which is believed to be of d wave type. The transition temperature reaches a maximum at the optimal doping of about 15%. The high  $T_c$  SF region has a characteristic bell shape for all hole-doped cuprates, even though the maximum  $T_c$  varies from about 40–93 K and higher. The region

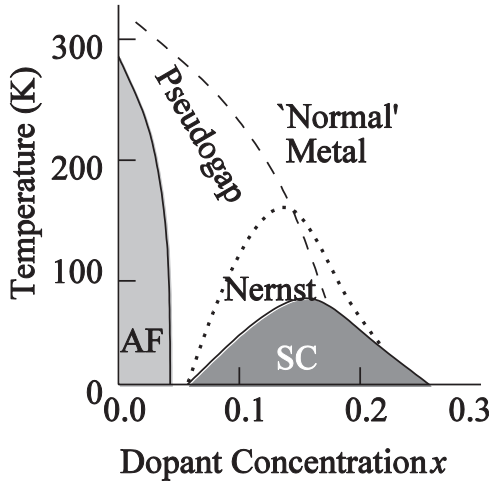


**Figure 2.** Schematic phase diagram of high  $T_c$  materials in the temperature versus dopant concentration,  $x$ , plane. AF and SC stand for antiferromagnet and d wave superconductor, respectively. Fluctuations of the SC appear below the dotted line corresponding to the Nernst effect. The pseudogap region extends below the dashed line. Reprinted figure, with permission, from Lee *et al* (2006). Copyright (2006) by the American Physical Society.

below the dashed line in figure 2, above  $T_c$  in the underdoped region (where  $x$  is smaller than optimal), is an exotic metallic state, called the pseudogap phase. Below the dotted line, there is a region of strong fluctuations of the superconducting phase characterized by the so-called Nernst effect (Lee 2008).

#### 2.4. Extended (dipolar) Hubbard models

Let us now go beyond contact interactions and consider the tight-binding description for systems with longer than contact, or simply with long-range, interactions. Instead of Coulomb interactions that appear between electrons in solids, in the physics of cold atoms a paradigmatic model can be realized with dipole–dipole interactions. This may have a magnetic origin, but strong interactions can also occur for electric dipole interactions as, e.g. between polar molecules. Recent reviews of ultracold dipolar gases in optical lattices provide a detailed introduction to and description of this subject for Fermi (Baranov 2008) and Bose (Lahaye *et al* 2009, Trefzger *et al* 2011) systems (see also Lewenstein *et al* 2012); here we present only the essentials.

Assuming a polarized sample where all dipoles point in the same direction, the total interaction potential consists of a contact term and a dipole–dipole part:

$$V(\mathbf{r} - \mathbf{r}') = g\delta(\mathbf{r} - \mathbf{r}') + \frac{d^2}{4\pi\epsilon_0} \frac{1 - 3\cos^2\theta}{|\mathbf{r} - \mathbf{r}'|^3}, \quad (22)$$

where  $\theta$  is the angle between the polarization direction of the dipoles and their relative position vector  $\mathbf{r} - \mathbf{r}'$ ,  $d$  is the electric dipole moment, and  $g$  is the amplitude of the contact interaction. Note that the classical interaction between two point dipoles contains also another  $\delta$ -type contribution, which is absent for effective atom–atom (molecule–molecule) interactions (or may be thought of as being incorporated into the contact term). For convenience, we denote the two parts of  $V(\mathbf{r} - \mathbf{r}')$  as  $U_c$  and  $U_{dd}$ , respectively.

The interaction between the dipoles is highly anisotropic. We consider a stable 2D geometry with a tight confinement in the direction of polarization of the dipoles. Applying an optical lattice in the perpendicular plane, the potential reads

$$V_{\text{ext}}(\mathbf{r}) = V_0 [\cos^2(\pi x/a) + \cos^2(\pi y/a)] + \frac{1}{2} m \Omega_z^2 z^2. \quad (23)$$

As previously, we use the expansion of the field operators in the basis of Wannier functions (strictly speaking a product of one-dimensional Wannier functions in the  $x$  and  $y$  directions with the ground state of the harmonic trap in the  $z$  direction with frequency  $\Omega_z$ ), and restrict our consideration to the lowest Bloch band.

**2.4.1. Dipolar Bose–Hubbard models.** Within the above described approximations, and for a one-component Bose system, the Hamiltonian becomes the standard Bose–Hubbard Hamiltonian (14) with the addition of a dipolar contribution, which reads in the basis of Wannier functions

$$\hat{H}_{dd} = \sum_{ijkl} \frac{U_{ijkl}}{2} \hat{b}_i^\dagger \hat{b}_j^\dagger \hat{b}_k \hat{b}_l, \quad (24)$$

where the matrix elements  $U_{ijkl}$  are given by the integral

$$U_{ijkl} = \int d^3r_1 d^3r_2 w_i^*(\mathbf{r}_1) w_j^*(\mathbf{r}_2) \times U_{dd}(\mathbf{r}_1 - \mathbf{r}_2) w_k(\mathbf{r}_1) w_l(\mathbf{r}_2). \quad (25)$$

The Wannier functions are localized at the minima of the optical lattice with a spatial localization  $\sigma$ . For a deep enough lattice,  $\sigma \ll a$ , the Wannier functions  $w_i(\mathbf{r})$  are significantly non-vanishing for  $\mathbf{r}$  close to the lattice centers  $\mathbf{R}_i$ , and thus the integral (25) may be significantly non-zero for the indices  $i = k$  and  $j = l$ . Thus, there are two main contributions to  $U_{ijkl}$ : the *off-site* term  $U_{ijij}$ , corresponding to  $k = i \neq j = l$ , and the *on-site* term  $U_{iiii}$ , where all the indices are equal.

**The off-site contribution.** The dipolar potential  $U_{dd}(\mathbf{r}_1 - \mathbf{r}_2)$  changes slowly on scales larger than  $\sigma$ . Therefore, one may approximate it with the constant  $U_{dd}(\mathbf{R}_i - \mathbf{R}_j)$  and take it out of the integration. Then the integral reduces to

$$U_{ijij} \simeq U_{dd}(\mathbf{R}_i - \mathbf{R}_j) \int d^3r_1 |w_i(\mathbf{r}_1)|^2 \int d^3r_2 |w_j(\mathbf{r}_2)|^2, \quad (26)$$

which leads to the off-site Hamiltonian

$$\hat{H}_{dd}^{\text{off-site}} = \frac{1}{2} \sum_{i \neq j} \frac{V}{|i - j|^3} \hat{n}_i \hat{n}_j, \quad (27)$$

with  $V = U_{ijij}$  and the sum running over all sites of the lattice.

**2.4.1.2. The on-site contribution.** At the same lattice site  $i$ , where  $|\mathbf{r}_1 - \mathbf{r}_2| \sim \sigma$ , the dipolar potential changes very rapidly and diverges for  $|\mathbf{r}_1 - \mathbf{r}_2| \rightarrow 0$ . Therefore, the integral

$$U_{iiii} = \int d^3r_1 d^3r_2 n(\mathbf{r}_1) U_{dd}(\mathbf{r}_1 - \mathbf{r}_2) n(\mathbf{r}_2), \quad (28)$$

with  $n(\mathbf{r}) = |w(\mathbf{r})|^2$  being the single-particle density, has to be calculated taking into account the atomic spatial distribution at the lattice site. The solution can be found by Fourier transformation, i.e.

$$U_d = U_{iiii} = \frac{1}{(2\pi)^3} \int d^3k \tilde{U}_{dd}(\mathbf{k}) \tilde{n}^2(\mathbf{k}), \quad (29)$$

which leads to an on-site dipolar contribution to the Hamiltonian of the type

$$\hat{H}_{dd}^{\text{on-site}} = \frac{U_d}{2} \sum_i \hat{n}_i(\hat{n}_i - 1). \quad (30)$$

Thus, for dipolar gases the effective on-site interaction  $U$  is given by

$$U = g \int d^3r |w(\mathbf{r})|^4 + \frac{1}{(2\pi)^3} \int d^3k \tilde{U}_{dd}(\mathbf{k}) \tilde{n}^2(\mathbf{k}), \quad (31)$$

which contains the contribution of the contact potential and the dipolar contribution (22).

Let us note that the dipolar part of the on-site interaction  $U_{iiii} = U_d$  (28) is directly dependent on the atomic density at a lattice site, and thus can be increased or decreased by changing the anisotropy and strength of the lattice confinement (see Lahaye *et al* 2009 for details).

We may now write the simplest tight-binding Hamiltonian of the system. Often one limits the off-site interaction term to nearest neighbors, thus only obtaining the Hamiltonian

$$\begin{aligned} \hat{H}_{\text{eBH}} = & -t \sum_{\langle i,j \rangle} \hat{b}_i^\dagger \hat{b}_j + \frac{U}{2} \sum_i \hat{n}_i(\hat{n}_i - 1) \\ & + \frac{V}{2} \sum_{\langle i,j \rangle} \hat{n}_i \hat{n}_j - \sum_i \mu_i \hat{n}_i, \end{aligned} \quad (32)$$

which is commonly referred to as the *extended* Bose–Hubbard model. Note that the sum over nearest neighbors  $\langle i,j \rangle$  leads to two identical terms in the off-site interaction  $V$  for pairs  $i,j$  and  $j,i$ . This is accounted for by the factor 1/2 in the Hamiltonian. The dipolar Bose–Hubbard model with interactions not truncated to nearest neighbors is discussed at the end of this section. The particle number is fixed by the chemical potential  $\mu_i$ , which can be site dependent, for instance due the presence of a trapping potential. For homogeneous systems, as discussed here, the chemical potential is constant, i.e.  $\mu_i = \mu$ . Slowly varying trapping potentials can be treated in the same framework by using the local density approximation.

For bosons, the phase diagram in one dimension has been intensively investigated, where the transition from superfluid to Mott insulator is of Berezinskii–Kosterlitz–Thouless (BKT) type (Kühner and Monien 1998, Kühner *et al* 2000). The inclusion of nearest-neighbor interaction leads to a density-modulated insulating phase with crystalline, staggered diagonal order. Depending on the context, the phase is referred to as a density wave or charge density wave (borrowed from electronic systems, where it is also used for metals with density fluctuations), Mott crystal or Mott solid. The phase in one dimension is referred to also as an alternating or staggered Mott insulator, whereas that in two dimensions is often referred to as a checkerboard phase. It was shown that there is a direct transition between the superfluid and the charge density wave without an intermediate supersolid phase, showing superfluid *and* crystalline order. Later it was realized that a bosonic Haldane insulator phase exists with non-local string

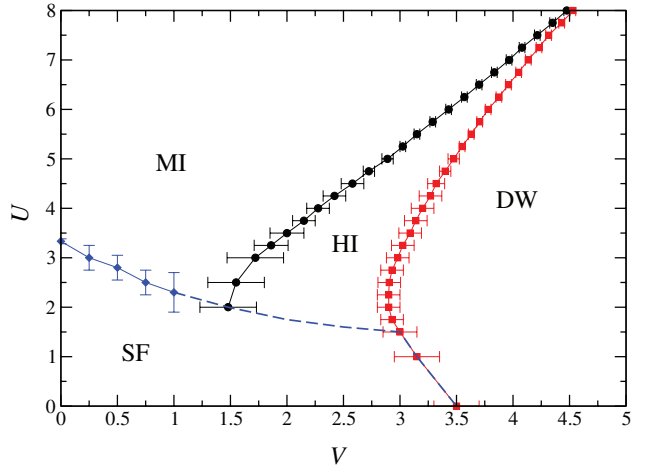


**Figure 3.** Phase diagram of the extended 1D Bose–Hubbard model (32) as a function of the on-site interaction  $U$  and the nearest-neighbor interaction  $V$  with  $t = 1$ . It shows the superfluid phase (SF), the Mott insulator (MI), the density wave (DW) and the Haldane insulator (HI) for the filling per site  $\rho = 1$ . This figure is from Rossini and Fazio (2012).

correlations (Dalla Torre *et al* 2006, Dalmonte *et al* 2011, Deng and Santos 2011, Rossini and Fazio 2012). While this gapped phase does not break the translational symmetry, particle–hole fluctuations appear in an alternating order. These fluctuations are separated by strings of equally populated sites. The corresponding phase diagram in one dimension and at filling (the density per site)  $\rho = 1$  is plotted in figure 3.

For non-commensurate fillings the model is also quite rich. It has been studied using a quantum Monte Carlo approach in two dimensions (Sengupta *et al* 2005) for fillings below unity. The phase diagram of the system for strong interactions  $U$  is reproduced in figure 4. Two interesting novel phases appear. The elusive supersolid (SS) phase shows a diagonal long-range order as revealed by a non-zero structure factor and simultaneously a non-zero superfluid density. As shown in figure 4, additionally regions of phase separation (PS) appear, which are revealed as discontinuities (jumps) of the filling  $\rho$  as a function of the chemical potential  $\mu$  (Sengupta *et al* 2005). When the on-site interaction becomes weaker, the SS phase becomes larger and PS regions disappear at filling larger than 1/2 (Maik *et al* 2013). For half-integer and integer fillings an insulating charge density wave (CDW) appears, which is also often referred to as a checkerboard phase (Sengupta *et al* 2005, Batrouni *et al* 2006, Sowiński *et al* 2012). These findings were confirmed and further studied in one-dimensional Monte Carlo (Batrouni *et al* 2006) and DMRG analyses (Mishra *et al* 2009).

The phase diagram becomes even richer when the true long-range interactions for dipoles, equation (27), are taken into account beyond nearest-neighbor interactions. The Hamiltonian reads then

$$\begin{aligned} \hat{H}_{\text{eBH}} = & -t \sum_{\langle i,j \rangle} \hat{b}_i^\dagger \hat{b}_j + \frac{U}{2} \sum_i \hat{n}_i(\hat{n}_i - 1) \\ & + \frac{1}{2} \sum_{i \neq j} \frac{V}{|i-j|^3} \hat{n}_i \hat{n}_j - \sum_i \mu_i \hat{n}_i. \end{aligned} \quad (33)$$

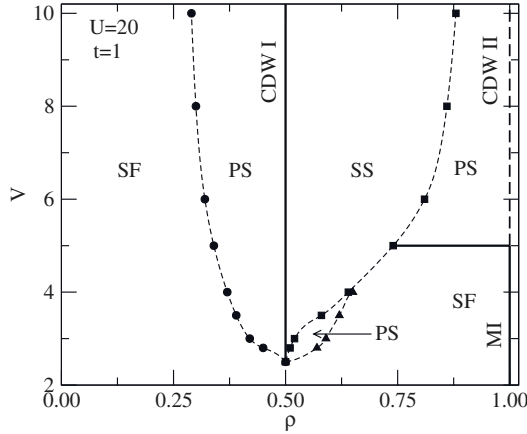


**Figure 4.** The phase diagram in the filling  $\rho - V$  parameter space of the extended two-dimensional Bose–Hubbard model  $U = 20$ . The energy unit is  $t = 1$ . The thick solid vertical line indicates the charge density wave (CDW I) at half-filling; other phases present are the superfluid (SF) and supersolid (SS), and at unit filling either the Mott insulator (MI) or another charge density wave (CDW II); PS denotes phase-separated regions. Reprinted figure, with permission, from Sengupta *et al* (2005). Copyright (2005) by the American Physical Society.

Consider the case of low filling in the hard core limit (with large on-site interaction  $U$ , excluding double occupancy). Such a case was discussed in Capogrosso-Sansone *et al* (2010) using large-scale quantum Monte Carlo (QMC) simulations. The Hamiltonian considered included the effects of a trap of frequency  $\omega$ , and was given by

$$\hat{H}_{\text{eBH}} = -t \sum_{\langle i,j \rangle} \hat{b}_i^\dagger \hat{b}_j + \frac{1}{2} \sum_{i \neq j} \frac{V}{|i-j|^3} \hat{n}_i \hat{n}_j - \sum_i (\mu - \Omega i^2) \hat{n}_i, \quad (34)$$

with the requirement that the initial system has no doubly occupied sites. The results are summarized in figure 5. For small enough hopping  $t/V \ll 0.1$ , it is found that the low energy phase is incompressible ( $\partial\rho/\partial\mu = 0$  with the filling factor  $\rho$ ) for most values of  $\mu$ . This parameter region is denoted as DS in figure 5 and corresponds to the classical *devil's staircase*. This is a succession of incompressible ground states, dense in the interval  $0 < \rho < 1$ , with a spatial structure commensurate with the lattice for all rational fillings (Hubbard 1978, Fisher and Selke 1980) and no analogue for shorter-range interactions. For finite  $t$ , three main Mott lobes emerge with  $\rho = 1/2$ ,  $1/3$ , and  $1/4$ , named checkerboard, stripe, and star solids, respectively. Their ground state configurations are visualized in figures 5(b)–(d). Interestingly, as found in Capogrosso-Sansone *et al* (2010) these phases survive in the presence of a confining potential and at finite temperature. Note that the shape of the Mott solids with  $\rho = 1/2$  and  $1/4$  away from the tip of the lobe can be shown to be qualitatively captured by mean-field calculations, while this is not the case for the stripe solid at filling  $1/3$  which has a sharp, point-like structure characteristic of fluctuation-dominated 1D configurations. Mott lobes at other rational filling factors, e.g.  $\rho = 1$  and  $7/24$ , have also been observed (Capogrosso-Sansone *et al* 2010), but are not shown in the figure. It is worth mentioning that in the strongly correlated regime (at low  $t/V$ ) the physics of the system is dominated by the presence of numerous metastable states resembling glassy systems, and QMC calculations

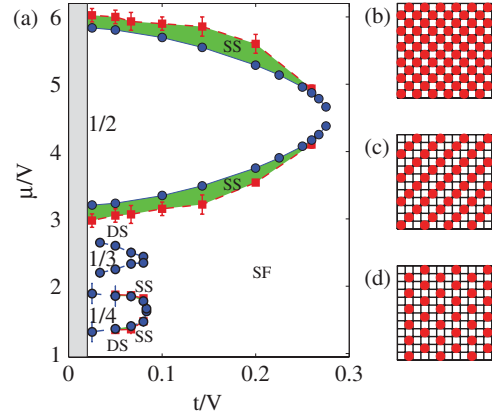


**Figure 5.** The phase diagram of the dipolar 2D Bose–Hubbard model in the hard core limit. The lobes represent insulating density waves (also denoted as Mott solids) with the densities indicated; SS denotes the supersolid phase, SF the superfluid phase and DS the devil's staircase. The panels (b)–(d) are sketches of the ground state configurations for the Mott solids with density (b)  $\rho = 1/2$  (checkerboard), (c)  $\rho = 1/3$  (stripe solid) and (d)  $\rho = 1/4$  (star solid). This figure is from Capogrosso-Sansone *et al* (2010).

in this case become practically impossible. These metastable states were in fact correctly predicted by the generalized mean-field theory (Menotti *et al* 2007).

For large enough  $t/V$ , the low energy phase is superfluid for all values of the chemical potential  $\mu$ . At intermediate values of  $t/V$ , however, doping the Mott solids (either removing particles creating vacancies or adding extra particles) stabilizes a supersolid phase, with coexisting superfluid and crystalline orders (no evidence of this phase has been found in the absence of doping). The solid/superfluid transition consists of two steps, with both transitions of second-order type and a supersolid as an intermediate phase. Remarkably, the long-range interactions stabilize the supersolid over a wide range of parameters. For example, a vacancy supersolid is present for fillings  $0.5 > \rho \gtrsim 0.43$ , roughly independently of the interaction strength. This is in contrast with typical extended Bose–Hubbard model results (compare figure 4) where the supersolid phase appears only for  $\rho > 0.5$ , i.e. no vacancy supersolid is observed. Similarly, the phase separation is not found when long-range interactions are taken into account (Capogrosso-Sansone *et al* 2010). Note, however, that in the former case soft bosons were considered, while hard core bosons are studied in Capogrosso-Sansone *et al* (2010).

Let us note that this is still not a full story. As discussed above, the Hamiltonian (27) is obtained assuming that the dipolar potential changes slowly on scales of the width of the Wannier functions,  $\sigma$ . Corrections due to finite  $\sigma$  have been discussed recently by Wall and Carr (2013). These corrections lead to deviations from the inverse-cube power law at short and medium distances on the lattice scale—the dependence here is instead exponential, with the power law recovered only for large distances. The resulting correction may be significant at moderate lattice depths and leads to quantitative differences in the phase diagram, as discussed for the one-dimensional case at unit filling (Wall and Carr 2013). The extent to which the full diagram is modified in 2D by these corrections is not yet known and is the subject of ongoing studies.

**2.4.2. Dipolar Fermi–Hubbard models** The fermionic version of the extended Hubbard model (32) with nearest-neighbor interactions is also widely discussed in solid state physics for both polarized (spinless) and spin 1/2 fermions (see Georges *et al* 2013, Gu *et al* 2004, Hirsch 1984, Kivelson 1987, Nasu 1983, Raghu *et al* 2008, Robaszkiewicz *et al* 1981, Si *et al* 2001). There are far fewer papers on the model including the true long-range interactions for dipoles, described for spinless fermions by the Hamiltonian

$$\hat{H}_{\text{eFH}} = -t \sum_{\langle i,j \rangle} \hat{f}_i^\dagger \hat{f}_j + \frac{1}{2} \sum_{i \neq j} \frac{V}{|i-j|^3} \hat{n}_i \hat{n}_j - \sum_i \mu_i \hat{n}_i. \quad (35)$$

This model has been studied by Mikelsons and Freericks using a mean-field ansatz (Mikelsons and Freericks 2011); in this way, a fermionic version of the phase diagram of figures 4(b)–(d) was derived for the homogenous case  $\mu_i = \mu$ .

Mikelsons and Freericks solve the model using mean-field theory (MFT). As they stress: ‘this can be justified, since the interaction is long range and consequently each site is effectively coupled to any other site. In fact, due to the absence of a local interaction, the MFT is equivalent to the dynamical mean-field theory (DMFT) approach, which becomes exact in the infinite-dimensional limit. The absence of a spin degree of freedom also implies that the model is in the Ising universality class, with a finite transition temperature in 2D’. Within MFT one approximates the interaction part of the Hamiltonian by writing

$$\hat{n}_i \hat{n}_j \approx \hat{n}_i \langle n_j \rangle + \langle n_i \rangle \hat{n}_j - \langle n_i \rangle \langle n_j \rangle, \quad (36)$$

i.e. one neglects the density fluctuations, as is done in the first-order (Hartree–Fock) self-consistent perturbation theory—this should be very accurate for small  $U/t$ . In the MFT approximation, the mean density  $\langle n_i \rangle$  is a fixed parameter in the Hamiltonian and acts as a site-dependent potential. The resulting MFT Hamiltonian is quadratic in the  $(\hat{f}, \hat{f}^\dagger)$  operators and can be easily diagonalized for large, but finite lattices, especially assuming translational invariance at some level. MFT can be regarded as a variational method and its results can be compared with another variational ansatz corresponding to phase separation. The results are presented in figures 6 and 7, where we present schematically unit cells, corresponding to different ‘charge density wave’ orderings, and the phase diagram at zero temperature  $T = 0$ .

### 3. Non-standard lowest band Hubbard models

The original article on the Hubbard model was published by J Hubbard in 1963 as a description of electrons in narrow bands (Hubbard 1963). As discussed in section 2.3, in this framework the many-particle Hamiltonian is restricted to a tunneling matrix element  $t$  and the on-site interaction  $U$ . Other two-particle interaction processes are considerably smaller than the on-site term and are therefore neglected. Hubbard’s article also gives an estimation on the validity of the approximation (for common d wave electron systems), where the (density–density) nearest-neighbor interaction  $V$  is identified as the first-order correction (see section 2.4). However, it was

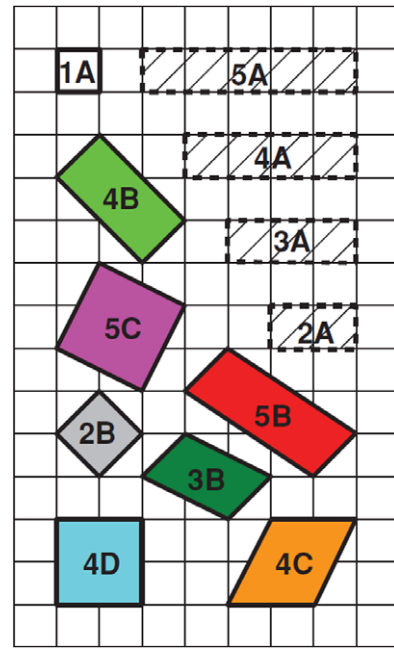


**Figure 6.** Unit cells corresponding to different density wave phases. Vertices indicate sites with higher density. Only density wave orders corresponding to unit cells with the solid outline were found to be stabilized. Reprinted figure, with permission, from Mikelsons and Freericks (2011). Copyright (2011) by the American Physical Society.

pointed out by Guinea, Hirsch, and others (Guinea 1988a, 1988b, Guinea and Schön 1988, Hirsch 1989, 1994, Strack and Vollhardt 1993, Amadon and Hirsch 1996) that one of the neglected terms in the two-body nearest-neighbor interaction describes the density-mediated tunneling of an electron along a bond to a neighboring site. It therefore contributes to the tunneling and was referred to as *bond-charge interaction* or *density-induced tunneling*. The main difference from the single-particle tunneling case stems from the fact that the operator depends on the density on the two neighboring sites. Strictly speaking, the simple Hubbard model is justified only if the bond-charge interaction is small compared with the tunneling matrix element. It is worth noticing that bond-charge terms were already considered, although they were then neglected, in the original paper of Hubbard of 1963, where he presented a non-perturbative approach based on the decoupling of the Green’s functions of the strongly interacting electron problem. Recently Grzybowski and Chhajlany (2012) applied the Hubbard method to a model with a strong bond-charge interaction term: these authors divided the tunneling terms into double-occupancy-preserving and double-occupancy-non-preserving ones, and treated the latter as a perturbation.

For optical lattices, this density-induced tunneling (Mazzarella *et al* 2006, Mering and Fleischhauer 2011, Jürgensen *et al* 2012, Lühmann *et al* 2012, Łęcki *et al* 2013) is of particular interest due to two points. First, unlike in solids, its amplitude can be rather large in optical lattices due to the characteristic shape of the Wannier functions for sinusoidal potentials. Second, the density-induced tunneling scales directly with the filling factor, which enhances its impact for bosonic or multi-component systems. In addition, ultracold atoms offer tunable interactions and differently ranged

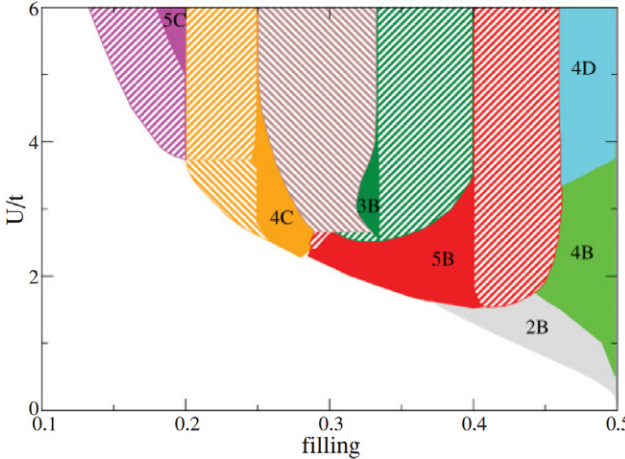


**Figure 7.** Phase diagram for  $T = 0$  including the phase separation (those regions are dashed). Decreasing the interaction contracts the range of filling of the ordered phases and progressively eliminates phases commensurate with low values of filling. The only phase surviving down to  $U/t = 0$  is the checkerboard phase (2B). Phase separation replaces the 4D phase near the fillings  $\rho = 0.28$  and  $\rho = 0.36$  for larger  $U/t$ . In parts of the phase diagram, 4C and 5C phases show phase separation with the homogeneous state. Reprinted figure, with permission, from Mikelsons and Freericks (2011). Copyright (2011) by the American Physical Society.

interactions such as contact (section 2.1) and dipolar interaction potentials (section 2.4).

Before focusing on bosons, we start the discussion by recalling one of the classic papers on non-standard Fermi–Hubbard models. In the following, different off-site interaction processes are discussed for bosons in optical lattices. We derive a generalized Hubbard model within the lowest band. Subsequently, the amplitudes of these off-site processes are calculated for both contact ( $\delta$ -function-shaped) interaction potentials and dipolar interactions. In the following sections, we focus on fermionic atoms and mixtures of different atomic species.

### 3.1. Non-standard Fermi–Hubbard models

In order to give the reader an idea of what has been studied in the past in condensed-matter physics, we follow the 1996 paper by Amadon and Hirsch on metallic ferromagnetism in a single-band model and the effects of band filling and Coulomb interactions (Amadon and Hirsch 1996). In this paper, the authors derive a single-band tight-binding model with on-site repulsion and nearest-neighbor exchange interactions as a simple model for describing metallic ferromagnetism. The main point is the inclusion of the effect of various other Coulomb matrix elements in the Hamiltonian that are expected to be of appreciable magnitude in real materials. They compare results from exact diagonalization and mean-field theory in 1D. Quoting the authors: ‘As the band filling decreases from 1/2, the tendency to ferromagnetism is found to decrease in exact diagonalization, while mean-field theory predicts the opposite behavior. A nearest-neighbor Coulomb repulsion is found to suppress the tendency to ferromagnetism; however, the effect becomes small for large on-site repulsion. A pair hopping interaction enhances the tendency to ferromagnetism. A nearest-neighbor hybrid Coulomb matrix element breaks

electron–hole symmetry and causes metallic ferromagnetism to occur preferentially for more-than-half-filled rather than less-than-half-filled bands in this model. Mean-field theory is found to yield qualitatively incorrect results for the effect of these interactions on the tendency to ferromagnetism’.

The starting point for the theory is the single-band tight-binding Fermi Hamiltonian with all Coulomb matrix elements included:

$$\hat{H} = - \sum_{\langle i,j \rangle, \sigma} t_{ij} (\hat{f}_{i\sigma}^\dagger \hat{f}_{j\sigma} + \text{h.c.}) + \sum_{i,j,k,l,\sigma,\sigma'} \langle ij|1/r|kl \rangle \hat{f}_{i\sigma}^\dagger \hat{f}_{j\sigma}^\dagger \hat{f}_{l\sigma'} \hat{f}_{k\sigma'}, \quad (37)$$

where  $\hat{f}_{i\sigma}^\dagger$  creates an electron of spin  $\sigma$  in a Wannier orbital at site  $i$ , which we denote as  $w_i(\mathbf{r})$ . The Coulomb matrix elements are given by the integrals

$$\langle ij|1/r|kl \rangle = \int d\mathbf{r} d\mathbf{r}' w_i^*(\mathbf{r}) w_j^*(\mathbf{r}') \frac{e^2}{|r - r'|} w_k(\mathbf{r}) w_l(\mathbf{r}'). \quad (38)$$

Restricting our consideration to just one-site and two-site integrals between nearest neighbors, the following matrix elements result:

$$U = \langle ii|1/r|ii \rangle, \quad (39)$$

$$V = \langle ij|1/r|ij \rangle, \quad (40)$$

$$J = \langle ij|1/r|ji \rangle, \quad (41)$$

$$J' = \langle ii|1/r|jj \rangle, \quad (42)$$

$$\Delta t = \langle ii|1/r|ij \rangle. \quad (43)$$

As argued by the authors: ‘matrix elements involving three and four centers are likely to be substantially smaller than these, as they involve additional overlap factors. Even though the repulsion term  $V$  could be of appreciable magnitude for sites further than nearest neighbors, we assume that such terms will not change the physics qualitatively’.

The resulting non-standard Fermi Hamiltonian reads

$$\hat{H} = - \sum_{\langle i,j \rangle, \sigma} t_{ij}^\sigma (\hat{f}_{i\sigma}^\dagger \hat{f}_{j\sigma} + \text{h.c.}) + U \sum_i \hat{n}_{i\uparrow} \hat{n}_{i\downarrow} + V \sum_{\langle i,j \rangle} \hat{n}_i \hat{n}_j + J \sum_{\langle i,j \rangle, \sigma, \sigma'} \hat{f}_{i\sigma}^\dagger \hat{f}_{j\sigma}^\dagger \hat{f}_{i\sigma'} \hat{f}_{j\sigma'} + J' \hat{f}_{i\sigma}^\dagger \hat{f}_{i\sigma'} \hat{f}_{j\sigma} \hat{f}_{j\sigma'}, \quad (44)$$

with  $\hat{n}_i = \hat{n}_{i\uparrow} + \hat{n}_{i\downarrow}$  and density-dependent tunneling

$$t_{ij}^\sigma = t_{ij} - \Delta t (\hat{n}_{i,-\sigma} + \hat{n}_{j,-\sigma}). \quad (45)$$

In the situation considered in Amadon and Hirsch (1996), ‘all matrix elements in the above expressions are expected to be always positive, except possibly for the hybrid matrix element  $\Delta t$ ’. However, with the convention that the single-particle hopping matrix element  $t$  is positive and that the operators describe electrons rather than holes, the sign of  $\Delta t$  is also expected to be positive. This should be contrasted with the situations that we can approach with bosons; discussed below.

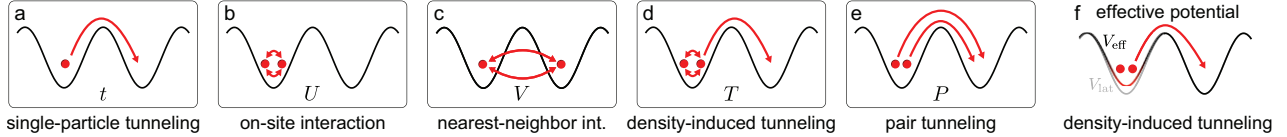


**Figure 8.** On-site and nearest-neighbor off-site processes. In the Hubbard model, only (a) the tunneling  $t$  and (b) the on-site interaction  $U$  are accounted for. Generalized Hubbard models can include (c) the nearest-neighbor interaction  $V$ , (d) the density-induced tunneling  $T$ , and (e) the pair tunneling  $P$ . The relative amplitudes of these processes depend on the interaction potential. They are plotted for contact interaction in figure 9 and for dipolar interaction in figure 12. (f) In optical lattices, the density-induced tunneling  $T$  has a relatively large amplitude and can therefore affect the tunneling in the system. Effectively, it gives rise to a modified tunneling potential, which is shallower (shown here) for repulsive and deeper for attractive interactions. This figure is adapted from Jürgensen *et al* (2012).

### 3.2. Non-standard Bose–Hubbard models with density-induced tunneling

We consider the same bosonic system as before with Hamiltonian (1) and optical lattice potential (11), and restrict the Wannier function expansion to the lowest Bloch band (13) using the same procedure as in section 2.2. While previously we provided some heuristic arguments for dropping various contributions of the interaction potential, we shall currently keep all the terms (restricting our consideration, however, to nearest neighbors only). For a general potential  $V(\mathbf{r} - \mathbf{r}')$ , define

$$V_{ijkl} = \int d\mathbf{r} d\mathbf{r}' w_i^*(\mathbf{r}) w_j^*(\mathbf{r}') V(\mathbf{r} - \mathbf{r}') w_k(\mathbf{r}) w_l(\mathbf{r}'). \quad (46)$$

The generalized lowest band Hubbard Hamiltonian reads then

$$\begin{aligned} \hat{H}_{\text{GBH}} = & -t \sum_{\langle i,j \rangle} \hat{b}_i^\dagger \hat{b}_j + \frac{U}{2} \sum_i \hat{n}_i (\hat{n}_i - 1) + \frac{V}{2} \sum_{\langle i,j \rangle} \hat{n}_i \hat{n}_j, \\ & -T \sum_{\langle i,j \rangle} \hat{b}_i^\dagger (\hat{n}_i + \hat{n}_j) \hat{b}_j + \frac{P}{2} \sum_{\langle i,j \rangle} \hat{b}_i^{\dagger 2} \hat{b}_j^2. \end{aligned} \quad (47)$$

All contributing processes in this model are sketched in figure 8. The third term represents the nearest-neighbor interaction  $V = V_{ijij} + V_{iji}$ , which was already introduced in section 2.4. Recall that the sum over nearest neighbors  $\langle i, j \rangle$  leads to two identical terms  $\hat{n}_i \hat{n}_j$  and  $\hat{n}_j \hat{n}_i$ . The fourth term  $T = -(V_{ijij} + V_{iji})/2$  also originates from the interaction. As illustrated in figure 8, it constitutes a process of hopping between neighboring sites and therefore directly affects the tunneling  $t$  in the lattice system. This process is known as density-induced or interaction-induced tunneling, density-dependent tunneling, and correlated tunneling, depending on the context. In the condensed-matter literature, this tunneling is also known as bond-charge interaction. The last term  $P = V_{ijij}$  denotes the pair tunneling amplitude of the process, when a pair of bosons hops from one site to the neighboring site. To get a general idea about the relative importance of these terms we look into systems with (i) contact interactions and (ii) contact and dipolar interactions.

**3.2.1. Bosons with contact interaction.** Let us start with correlated processes for ultracold bosonic atoms interacting via a contact interaction  $V(\mathbf{r} - \mathbf{r}') = g\delta(\mathbf{r} - \mathbf{r}')$ . Here, we assume an isotropic three-dimensional optical lattice with lattice depths  $V_x = V_y = V_z = V_0$ . In units of the recoil energy  $E_R = \hbar^2/(8ma^2)$ , where  $a$  is the lattice constant, and for Wannier functions  $w_i(\mathbf{r})$

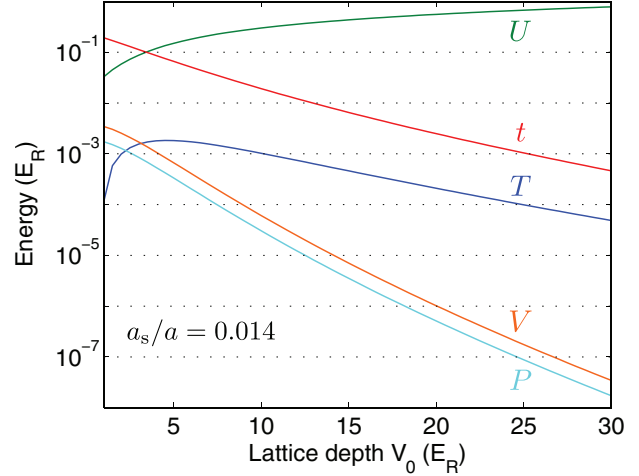


**Figure 9.** Lowest band parameters, from contact interactions, for the on-site interaction  $U$ , the tunneling  $t$ , the interaction-induced tunneling  $T$ , the nearest-neighbor interaction  $V$ , and the pair tunneling  $P$ . All interaction processes scale linearly with the scattering length  $a_s/a$ , whereas the tunneling  $t$  is unaffected. The amplitudes are plotted for an isotropic 3D optical lattice with lattice depth  $V_0$  and scattering length  $a_s/a = 0.014$ . This figure is adapted from Lühmann *et al* (2012).

in lattice coordinates  $\mathbf{r} \rightarrow \mathbf{r}/a$ , the interaction integral can be expressed as

$$V_{ijkl} = \frac{8}{\pi} \frac{a_s}{a} \int w_i^*(\mathbf{r}) w_j^*(\mathbf{r}) w_k(\mathbf{r}) w_l(\mathbf{r}) d\mathbf{r}. \quad (48)$$

This integral gives rise to various contributions: the on-site interaction  $U_c$ , next-neighbor interaction  $V_c$ , density-induced tunneling  $T_c$ , and pair tunneling  $P_c$  given by (with the subscript c denoting contact interactions)

$$\begin{aligned} U_c/E_R &= U_{iiii}, \\ V_c/E_R &= U_{ijij} + U_{iji} = 2U_{ijij}, \\ T_c/E_R &= -(U_{ijij} + U_{iji})/2 = -U_{ijij}, \\ P_c/E_R &= U_{ijij}. \end{aligned} \quad (49)$$

Since in this part we shall consider contact interactions only, we drop the subscript c in the following for convenience. We shall reintroduce it later, when also dipolar interactions will be discussed. From the integral expression (48), we see that the amplitudes are proportional to the effective scattering length  $a_s/a$  and otherwise depend solely on properties of the Wannier functions. All amplitudes are plotted in figure 9, where one sees that the on-site interaction  $U$  is the dominating energy. For neutral atoms, the nearest-neighbor interaction  $V$  and the

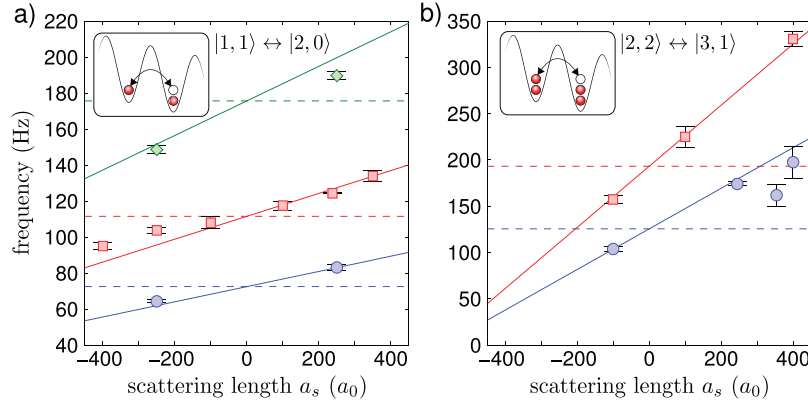


**Figure 10.** The oscillation frequency of the doublon number in a tilted optical lattice, depending on the scattering length  $a_s$  for a filling of (a)  $n = 1$  and (b)  $n = 2$ . The data sets are obtained for optical lattices with  $V_x = V_y = 20 E_R$  and  $V_z = 8 E_R$  (green),  $10 E_R$  (red), and  $12 E_R$  (blue). The scattering length is tuned via a Feshbach resonance, where  $a_0$  is the Bohr radius. The solid lines represent the theoretical prediction  $\nu_n(t + (2n - 1)T)/\hbar$ , where  $T$  is proportional to the scattering length  $a_s$  and  $\nu_n$  is a prefactor for the resonant oscillation. The constant dashed line corresponds to the single-particle tunneling, i.e.  $\nu_n t/\hbar$ . Figure from Jürgensen *et al* (2014).

pair tunneling amplitude  $P$  are much smaller than both  $U$  and the (single-particle) tunneling amplitude  $t$  (for  $V_0 \gtrsim 10 E_R$ ). However, the amplitude of the density-induced tunneling

$$\hat{T} = -T \hat{b}_i^\dagger (\hat{n}_i + \hat{n}_j) \hat{b}_j \quad (50)$$

is considerably larger than  $V$  and  $P$ . Due to the structure of this operator, we can combine it with the conventional single-particle tunneling  $t$  to give an effective hopping

$$\hat{t}_{\text{eff}} = -[t + T(\hat{n}_i + \hat{n}_j - 1)] \hat{b}_i^\dagger \hat{b}_j. \quad (51)$$

Although this density-dependent hopping is small in comparison with the on-site interaction  $U$ , it can constitute a substantial contribution to the tunneling process. For repulsive interactions, as depicted in figure 9, the value of  $T$  is positive and thus increases the magnitude of the overall tunneling, whereas attractive interactions decrease the overall magnitude.

The process of the density-induced tunneling (51) can also be illustrated within an effective potential picture (Lühmann *et al* 2012), by inserting the explicit expressions for the integral  $T_c$  (48) and the tunneling amplitude  $t$  (15). The term  $\hat{n}_i + \hat{n}_j - 1$  corresponds to the density  $n_{\text{DI}}(\mathbf{r}) = n_i|w_i(\mathbf{r})|^2 + (n_j - 1)|w_j(\mathbf{r})|^2$  on sites  $i$  and  $j$  excluding the hopping particle. The effective hopping operator (51) can then be written as

$$\hat{t}_{\text{eff}} = \int d^3r w_i^* \left( \frac{\mathbf{p}^2}{2m} + V(\mathbf{r}) + gn_{\text{DI}}(\mathbf{r}) \right) w_j \hat{b}_i^\dagger \hat{b}_j. \quad (52)$$

Here,  $V(\mathbf{r}) + g n_{\text{DI}}(\mathbf{r})$  can be identified as an effective tunneling potential, which is illustrated in figure 8(f). Since the density  $n_{\text{DI}}(\mathbf{r})$  is maximal at the lattice site centers, the effective tunneling potential corresponds to a shallower lattice for repulsive interactions and therefore causes an increased tunneling. In this effective potential, the band structure and the Wannier functions are altered. Such a modified band structure was experimentally observed in optical lattices for an atomic Bose–Fermi mixture (Heinze *et al* 2011) (see section 3.4).

<sup>12</sup> A scattering length of  $a_s = 100 a_0$  at a lattice spacing of  $a = 377$  nm corresponds to  $a_s/a = 0.014$ .

For standard  $^{87}\text{Rb}$  parameters<sup>12</sup>, the bare amplitude  $T$  reaches roughly 10% of the tunneling amplitude  $t$  for deep lattices (see figure 9). In addition, the density-induced tunneling scales with the particle number on neighboring sites as  $n_i + n_j - 1$ . At a filling factor of  $n = 3$ , the correction is about 30% at the superfluid–Mott insulator transition point. Note that all amplitudes except the tunneling  $t$  scale linearly with the interaction strength. By using Feshbach resonances to change the interaction strength, the amplitudes of  $T$  and  $U$  can be tuned independently from the lattice depth and thus the tunneling  $t$ . In contrast, for contact interactions the ratio  $T/U$  is only a function of the lattice depth.

The direct detection of density-induced tunneling was performed in an optical lattice experiment with Cs atoms and tunable interactions (Meinert *et al* 2013, Jürgensen *et al* 2014). Here, a Mott insulator, prepared in a quasi-one-dimensional lattice, is tilted by an offset energy  $\epsilon$  per lattice site. By quenching the lattice into tunneling resonance, where the additional on-site energy  $U$  of a hopping particle equals the tilt  $\epsilon$ , resonant oscillation can be observed (see the insets of figure 10). Due to the compensation of the dominating on-site interaction, the oscillation frequency is a direct measure for the (total) tunneling  $\hat{t}_{\text{eff}}$  (51), thereby revealing interaction effects on its amplitude. Figure 10 shows the observed oscillation frequency as a function of the interaction strength for filling factors  $n = 1$  and  $n = 2$ . It shows the linear dependence of the density-dependent tunneling on both the scattering length  $T \propto a_s/a$  and the density  $T \propto 2n - 1$ . The solid lines depict the theoretical prediction for  $\hat{t}_{\text{eff}}$ , whereas the constant dashed line corresponds to single-particle tunneling in the standard Hubbard model.

As a direct consequence of the density-induced tunneling, the critical point of the superfluid–Mott insulator transition is affected, depending on both the scattering length and the filling factor, and the transition is shifted towards deeper lattices for repulsive interactions. Since the nearest-neighbor interaction  $V$  and the pair tunneling  $P$  have very small amplitudes (figure 9), for neutral atoms we can neglect their contributions in the following. Mean-field theory allows us to demonstrate

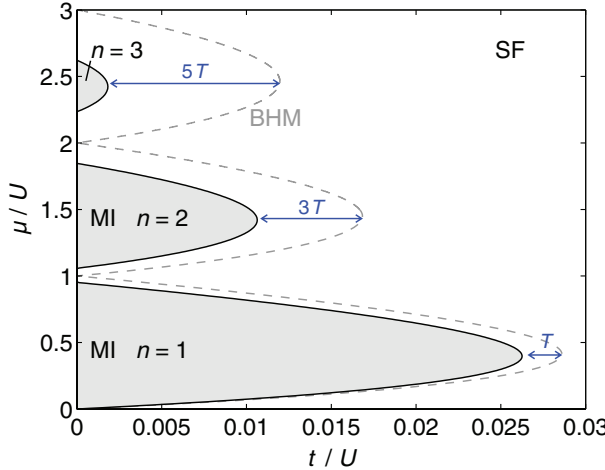


**Figure 11.** Phase diagram of the generalized Bose–Hubbard model with density-induced tunneling  $T = 0.002 U$  in an isotropic three-dimensional lattice with  $z = 6$  nearest neighbors. It shows the transition from the superfluid phase (SF) to the Mott insulator phases (MI) with filling  $n$ . Between the Mott lobes at  $J/U \rightarrow 0$ , the density-induced tunneling prohibits the Mott insulating state. The dashed line depicts the results from the standard Bose–Hubbard model (BHM). The blue arrows indicate the occupation-dependent change of the overall tunneling by  $(2n - 1) T$  for filling  $n$  at the tips of the Mott lobes, which captures the main impact of the density-induced tunneling. The phase diagram is calculated by means of a Gutzwiller mean-field theory. Note that the second-order perturbation (54) with a single mean-field parameter fails at large values of  $T$ .

how the interaction-induced tunneling affects the ground state phase diagram of the generalized Bose–Hubbard Hamiltonian  $\hat{H}_{\text{GBH}} - \mu \sum_i \hat{n}_i$  (equation (47)) with  $V = P = 0$ , where  $\mu$  is the chemical potential. In mean-field theory, a superfluid order parameter  $\psi = \langle \hat{b}_i \rangle = \langle \hat{b}_i^\dagger \rangle$  is introduced, where  $\psi \neq 0$  corresponds to the superfluid phase (SF) and  $\psi = 0$  defines the Mott insulator (MI) with a fixed particle number per lattice site (Fisher *et al* 1989, van Oosten *et al* 2001). The decoupling of the lattice sites is achieved by neglecting the fluctuations between  $\hat{b}_i^\dagger$  and  $\hat{b}_j$  of quadratic order, i.e.

$$\hat{b}_i^\dagger \hat{b}_j \approx \hat{b}_i^\dagger \hat{b}_j - \left( \hat{b}_i^\dagger - \langle \hat{b}_i^\dagger \rangle \right) \left( \hat{b}_j - \langle \hat{b}_j \rangle \right) = \psi \left( \hat{b}_i^\dagger + \hat{b}_j \right) - \psi^2. \quad (53)$$

Analogously, the density-induced tunneling can be decoupled via

$$\hat{b}_i^\dagger \hat{n}_i \hat{b}_j + \hat{b}_i^\dagger \hat{n}_j \hat{b}_j \approx \psi \left( \hat{b}_i^\dagger \hat{n}_i + \hat{n}_j \hat{b}_j \right), \quad (54)$$

disregarding terms of order  $\psi^3$  (Lühmann *et al* 2012). With the decoupling above, one can perform second-order perturbation of  $\psi$  for a Mott lobe with  $n$  particles per site (see van Oosten *et al* 2001).

The results are plotted in figure 11 for the Bose–Hubbard model (dashed line) and the generalized Hubbard model with  $T/U = 0.002$  (solid line). Although  $T$  is much smaller than  $U$ , the transition from the superfluid to the Mott insulator phase is significantly shifted towards lower values of

$t/U$ . The occupation-dependent nature of  $\hat{T} = -T \hat{b}_i^\dagger (\hat{n}_i + \hat{n}_j) \hat{b}_j$  is reflected by the fact that the Mott lobes with higher filling factors  $n$  are more strongly affected. In fact, for the given example, lobes with  $n \geq 4$  do not exist. The effect of interaction-induced tunneling can be mainly captured by the change of the overall tunneling as indicated by equation (51). For a filling factor  $\hat{n}_i \rightarrow n$ , the generalized and standard Bose–Hubbard models differ by approximately  $(2n - 1) T$  at the tips of the Mott lobes. Below and above the tips, hole and particle excitations, respectively, become more probable at the phase boundary. Thus, the shift of the Bose–Hubbard Mott lobes by the density-induced tunneling interpolates between the tips and can be approximated well by  $2 T \mu/U$ . Note that this type of phase diagram can be achieved experimentally by keeping the lattice depth  $V_0$  (and therefore  $t$ ) fixed and tuning  $t/U$  by using a Feshbach resonance.

The modified phase diagram with a fixed interaction strength but variable lattice depth is shown in figure 15 for  $^{87}\text{Rb}$  parameters in a three-dimensional lattice. The curve for bosons only corresponds to vanishing Boson–Fermion scattering length,  $a_{\text{BF}} = 0 a_0$ . The density-induced tunneling in combination with multi-orbital processes is discussed in section 4. In addition to affecting the ground state properties, the density-induced tunneling also influences the dynamic behavior, which is discussed, e.g. in Łącki *et al* (2013) and Łącki and Zakrzewski (2013).

**3.2.2. Bosons with dipolar interaction.** For bosons with dipolar interaction, the situation can change drastically. For simplicity, we assume that the dipoles are polarized along the  $z$  direction. We will consider two-dimensional lattice geometries with the potential given by (23), where the Wannier function along the  $z$  direction is just a harmonic oscillator ground state eigenfunction, such that there is no aggregation of atoms or molecules along the  $z$  direction due to attracting interactions. As for contact interactions, we work in dimensionless units by scaling the distance with respect to the lattice constant  $a = \lambda/2$ , i.e.  $\pi x/a \rightarrow x$ , and assume the recoil energy as a natural energy unit. Then, the interaction potential reads

$$U_{\text{dd}}(\mathbf{r}) = \mathcal{D} \frac{1 - 3 \cos^2 \theta}{r^3} \quad (55)$$

(compare (22)), with the effective dipolar strength denoted by  $\mathcal{D} = d^2 m / 2\pi^3 \epsilon_0 \hbar^2 a$ , where  $d$  is the dipole moment of the polar molecules, and  $\epsilon_0$  the vacuum permittivity. For atoms, the dipolar (magnetic) strength  $\mathcal{D} = \mu_0 \mu^2 m / 2\pi^3 \hbar^2 a$ , where  $\mu$  is the magnetic dipole moment and  $\mu_0$  denotes the vacuum permeability.

Dipolar interactions act together with contact interactions, affecting, e.g. the nearest-neighbor interactions and correlated tunneling amplitudes. The Hamiltonian now takes the form (47) with the parameters  $U = U_c + U_{\text{dd}}$ ,  $V = V_c + V_{\text{dd}}$ ,  $P = P_c + P_{\text{dd}}$  and  $T = T_c - T_{\text{dd}}$  (we have reintroduced the subscript  $c$  for the contact interaction contribution). Note the minus sign between the density-induced tunneling contributions due to

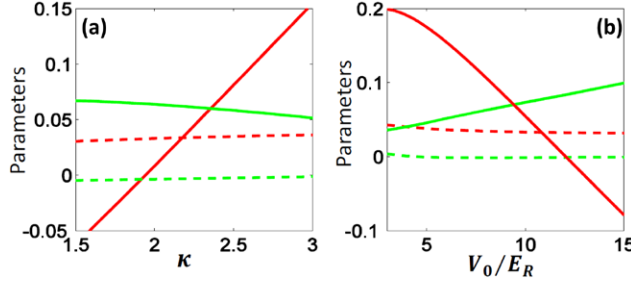


**Figure 12.** The change of the interaction parameters as (a) a function of the trap flattening  $\kappa$  for a lattice depth of  $V_0 = 6E_R$ , and (b) a function of the lattice depth  $V_0/E_R$  for a fixed trap flattening parameter  $\kappa = 3$ . The red solid line denotes the on-site interaction  $U_{dd}/E_R$ , the red dashed line denotes the nearest-neighbor interaction  $V_{dd}/E_R$ , the green solid line denotes the interaction-induced tunneling  $T_{dd}/J$ , and the green dashed line denotes the pair-tunneling amplitude  $P_{dd}/J$ . A sketch of the different processes can be found in figure 8.

the definitions in (49) and (57) below. Further on, we omit the terms in  $V_c$  and  $P_c$ , as they are very small (see the preceding section). By means of the dipolar interaction integral

$$D_{ijkl} = \mathcal{D} \int w_i^*(\mathbf{r}) w_j^*(\mathbf{r}') U_{dd}(\mathbf{r} - \mathbf{r}') w_k(\mathbf{r}') w_l(\mathbf{r}) d\mathbf{r} d\mathbf{r}', \quad (56)$$

we can express the dipolar on-site interaction ( $U_{dd}$ ), the nearest-neighbor interactions ( $V_{dd}$ ), the density-induced tunneling ( $T_{dd}$ ), and the pair tunneling amplitude ( $P_{dd}$ ) as follows:

$$\begin{aligned} U_{dd} / E_R &= D_{iiii}, \\ V_{dd} / E_R &= D_{ijij} + D_{iji}, \\ T_{dd} / E_R &= D_{iiji}, \\ P_{dd} / E_R &= D_{iiji}, \end{aligned} \quad (57)$$

where the amplitudes again vary linearly with the strength  $\mathcal{D}$ . But now the proportionality constant depends on the shape of the Wannier functions and the dipolar interaction. Thus, by tuning the lattice parameters and the trap frequency, one only changes the proportionality factors in equation (57). We illustrate this dependence in figure 10 for a dipolar strength  $\mathcal{D} = 1$ . To take into account the effect of the harmonic trap along the  $z$  direction, we introduce a trap flattening parameter  $\kappa = \hbar\Omega/2E_R$ . We see from figure 12(a) that for a fixed lattice depth, the on-site interaction  $U_{dd}$  decreases with decreasing  $\kappa$ , and when  $\kappa$  becomes lower than a critical value, the interaction strength  $U_{dd}$  becomes negative. This point corresponds to the situation where the width of the Wannier function is roughly equal to the trap length along the  $z$  direction. This shows that the on-site interaction strength can be tuned by changing the trap flattening ratio  $\kappa$ . On the other hand, the nearest-neighbor interaction  $V_{dd}$  does not show a strong dependence on the trap flattening  $\kappa$ , since it is mainly controlled by the distance between the lattice sites. The single-particle correlated tunneling amplitude  $T_{dd}$ , however, varies strongly with the lattice flattening, and it is positive even if the interactions are effectively repulsive. The parameter plotted in figure 12 for  $\mathcal{D} = 1$  corresponds to weak polar molecules, whereas for a dipole strength  $\mathcal{D} \sim 10$  one can reach the limit where the correlated tunneling is of the same

order as the single-particle tunneling:  $T_{dd} \sim t$ . The total density-induced tunneling amplitude (defined above as  $T = T_c - T_{dd}$ ) may thus change sign depending on  $V_0$  or  $\kappa$ . Notice also that the pair tunneling amplitude is much smaller than other parameters present in the Hamiltonian. We plot in figure 12(b) the parameters as a function of the lattice depth  $V_0/E_R$  for a fixed trap flattening ratio  $\kappa = 3$ . Here also the parameters follow the same trend, as  $T_{dd}$  is positive and the on-site interaction decreases as the lattice depth gets stronger. As soon as the width of the Wannier functions along the  $x$ - $y$  plane becomes similar to the oscillator width along the  $z$  direction, the on-site strength vanishes as before and an increase in the lattice depth leads to an attractive on-site interaction. The sensitivity of the interaction parameters to the geometry of the lattice sites described above was originally discussed in Sowiński *et al* (2012). It was also noticed and discussed in detail in Wall and Carr (2013), where it is shown that the effects become even more dramatic in a reduced quasi-1D geometry.

To appreciate the effect of the density-induced tunneling  $T$  for the physics of the extended model, we first consider the non-commensurate case for a two-dimensional system, with example results presented in figure 13. The complete analysis obtained using quantum Monte Carlo simulations can be found in Maik *et al* (2013). Following the discussion comparing the orders of magnitude of different terms above, it is assumed that  $|T| \approx V/10$  (with either positive or negative sign). Since the pair hopping  $P$  is usually much smaller, it is omitted ( $P = 0$ ). Thus, figure 14 presents the effects due to density-dependent tunneling, as compared with figure 5. Observe that, while for the contact interactions the density-induced tunneling shifts the borders between different phases, for dipolar interactions these additional contributions may lead to a disappearance of the phase separation (PS). A similar behavior appears for  $T = 0$  for smaller values of  $U$  (compare Maik *et al* 2013).

While the above analysis was carried out for rather arbitrarily chosen parameter values, one may also assume specific atomic parameters. Consider (Sowiński *et al* 2012) an ultracold gas of dipolar molecules confined in an optical lattice with lattice depth  $V_0 = 6 E_R$ , mass  $m = 127$  a.m.u and  $\lambda = 790$  nm. We assume the s wave scattering length of the molecules to be  $a_s \approx 100a_0$ . For these parameters,  $g \approx 1.06$  is approximately constant. We consider dipole moments  $d$  up to  $\sim 3D$  (Debye), which can be achievable for molecules like bosonic RbCs, KLi (Voigt *et al* 2009). We also choose the lattice parameter  $\kappa \approx 1.95$ , making (additionally to  $t$ ) the on-site interaction  $U$  almost independent of the dipole moment ( $U_{dd} \approx 0$ ). In this case, for a large enough dipolar strength  $\mathcal{D}$ , one expects with increasing  $d$  the parameters  $V$ ,  $T$ , and  $P$  to determine the system properties. For clarity, we restrict our consideration to a 1D chain of  $N$  lattice sites with periodic boundary conditions. We analyze the influence of the additional terms  $T$  and  $P$  on the grand canonical phase diagram, where the particle number is not conserved. For this, we add a chemical potential term  $-\mu \sum_i \hat{n}_i$  to the Hamiltonian (47). Figure 15 shows the phase diagram as well as the average number of particles per site for exact diagonalization

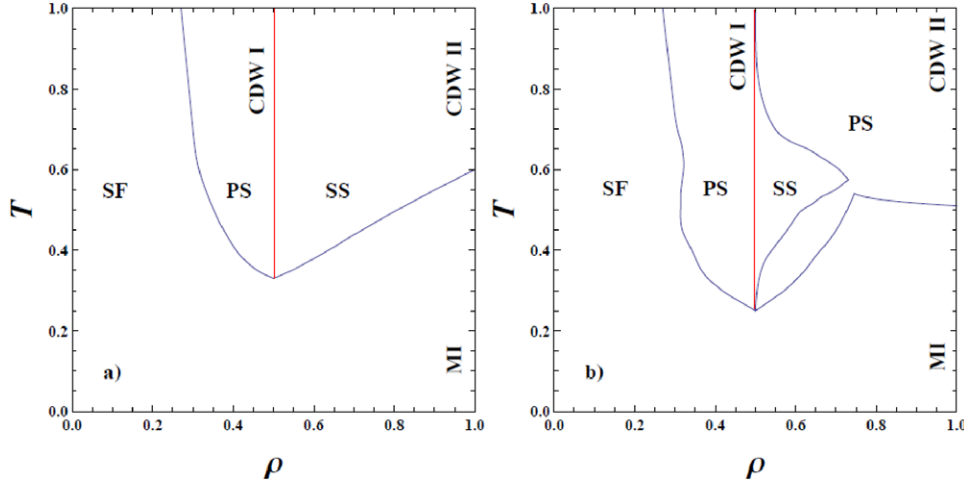


**Figure 13.** The phase diagrams for  $U = 20$  at finite  $T$  (with  $V = 10|T|$  and  $t = 1$  the unit of energy). (a) If  $t$  and  $T$  are of the same sign, the relative importance of the interactions decreases, leading to the disappearance of PS regions at filling greater than a half. Compared to the  $T = 0$  cases (figure 5), this phase diagram resembles more the case for low  $U = 5$ . (b) If  $T$  and  $t$  compete due to having opposite signs, the relative importance of the interactions is enhanced, increasing the PS regions while the supersolid phase region shrinks. This figure is from Maik *et al* (2013).

calculations for four sites with occupation truncated at four particles per site. Without the modified terms, with increasing dipolar strength the system becomes insulating with checkerboard order (above also referred to as the charge density wave) due to the increased nearest-neighbor repulsion. The right-hand plot reveals that the inclusion of the density-induced tunneling changes the phase diagram. A novel pair superfluid phase arises (characterized by a non-zero pair superfluid order parameter  $\sum \langle \hat{b}_i^2 \rangle$ ) as one increases the dipolar strength. Since in the exact diagonalization the particle number is conserved, superfluid and pair superfluid phases are not identified with the typical order parameters but rather with large first,  $\phi_i = \sum_j \langle \hat{b}_j^\dagger \hat{b}_i \rangle$ , and second,  $\Phi_i = \sum_j \langle \hat{b}_j^\dagger \hat{b}_j^\dagger \hat{b}_i \rangle \hat{b}_i \rangle$ , correlation functions, respectively. Apparently, a sufficiently

large tunneling  $T$  destroys the insulating checkerboard phase, making way for a pair superfluid.

### 3.3. Non-standard Bose–Fermi–Hubbard models

The density-induced tunneling discussed above also plays an important role in multi-component systems, where the atoms either have a spin degree of freedom or represent different atomic species. In particular, the interspecies interaction directly induces tunneling within both components. Here, the most interesting case of a mixture of bosonic and fermionic species is discussed. However, several aspects can be transferred to other multi-component systems. The Bose–Fermi–Hubbard model presented in the following describes the case where bosonic and fermionic species are spin polarized and interact via contact interaction. The experimental realizations of atomic mixtures of bosonic and fermionic particles in optical lattices (Günter *et al* 2006, Ospelkaus *et al* 2006b, Best *et al* 2009, Heinze *et al* 2011) have triggered a lively discussion about the

role of interspecies and intraspecies interactions (Cramer *et al* 2008, Lühmann *et al* 2008, Lutchyn *et al* 2009, Cramer 2011, Mering and Fleischhauer 2011, Jürgensen *et al* 2012).

The standard Bose–Fermi–Hubbard Hamiltonian (Albus *et al* 2003) is given by

$$\hat{H}_{\text{BFH}} = - \sum_{\langle i,j \rangle} (t_B \hat{b}_i^\dagger \hat{b}_j + t_F \hat{c}_i^\dagger \hat{c}_j) + \frac{U_{\text{BB}}}{2} \sum_i \hat{n}_i (\hat{n}_i - 1) + \sum_i U_{\text{BF}} \hat{n}_i \hat{m}_i - \sum_i (\mu_B \hat{n}_i + \mu_F \hat{m}_i), \quad (58)$$

where  $t_B$  is the tunneling matrix element for bosons and  $t_F$  is that for fermions. The intraspecies and interspecies interactions are restricted to the on-site interactions  $U_{\text{BB}}$  and  $U_{\text{BF}}$ , respectively. Here,  $\hat{b}_i$  ( $\hat{c}_i$ ) is the bosonic (fermionic) annihilation operator and  $\hat{n}_i$  ( $\hat{m}_i$ ) the respective particle number operator, where the total numbers of bosonic and fermionic atoms are fixed by the chemical potentials  $\mu_B$  and  $\mu_F$ . Let us assume for simplicity that the fermions are in a perfect band insulator phase where Pauli blocking prohibits the fermionic tunneling. This freezes out the fermionic degrees of freedom and the resulting Hamiltonian captures the behavior of the bosonic component under the influence of exactly one fermion per lattice site ( $\langle \hat{m}_i \rangle = 1$ ). Consequently, the Bose–Fermi–Hubbard Hamiltonian simplifies to an effective bosonic Hamiltonian:

$$\hat{H}_{\text{FBH}} = - \sum_{\langle i,j \rangle} t_B \hat{b}_i^\dagger \hat{b}_j + \frac{U_{\text{BB}}}{2} \sum_i \hat{n}_i (\hat{n}_i - 1) + \sum_i (U_{\text{BF}} - \mu_B) \hat{n}_i. \quad (59)$$

In this case, the energy of interaction,  $U_{\text{BF}}$ , between bosons and fermions can be fully absorbed into an effective chemical potential  $\mu_{\text{eff}} = \mu_B - U_{\text{BF}}$ . Hence, the resulting effective Hamiltonian does not differ from the standard Bose–Hubbard model, except for there being a modification of the chemical potential. As a consequence, the behavior of the bosons

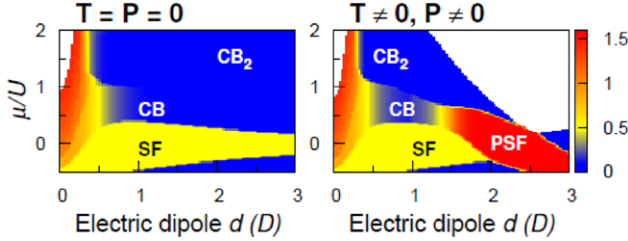


**Figure 14.** Phase diagram without (left) and with (right)  $T$  and  $P$  taken into account for a model of polar molecules with parameters defined in the text. The color quantifies the superfluidity indicators  $\phi_i$  and  $\Phi_i$  (see the text). Neglecting  $T$  and  $P$ , for large enough  $d$  and  $\mu$  the system is always in an insulating phase and the average number of particles is a multiple of 1/2. CB ( $CB_2$ ) denotes a checkerboard phase where sites with zero and one (two) particles alternate. Including the new terms, the insulating phases vanish for large enough  $d$ , and pair superfluidity (PSF) appears. This figure is from Sowiński *et al* (2012).

is not influenced by the homogeneously distributed fermions, which is in contradiction to the experimental observations (Günter *et al* 2006, Ospelkaus *et al* 2006b, Best *et al* 2009). Omitting the band insulator assumption above and taking into account the experimental confinement has also only little influence (Pollet *et al* 2008). Therefore, extended interspecies processes must play roles that are not covered in the Bose–Fermi–Hubbard model (Mering and Fleischhauer 2011, Jürgensen *et al* 2012).

The off-site processes arising from the boson–boson interaction (see figure 8) are elaborated on in section 3.2. The Bose–Fermi interaction leads to additional distinct processes, since the interacting particles are distinguishable—such as the cross-tunneling, where bosonic and fermionic particles interchange sites. For the density-induced tunneling, either a boson or a fermion can tunnel.

However, for a fermionic band insulator all processes that involve the hopping of a fermion are forbidden. In this case, only on-site interactions and the density-induced tunneling of bosons have to be taken into account, since other processes are prohibited or contribute only with small amplitudes (compare figure 9). The generalized, effective Hubbard model of the lowest band including these processes reads (Jürgensen *et al* 2012)

$$\hat{H} = - \sum_{\langle i,j \rangle} [t_B + T(\hat{n}_i + \hat{n}_j - 1) + 2T_{BF}] \hat{b}_i^\dagger \hat{b}_j + \frac{U_{BB}}{2} \sum_i \hat{n}_i (\hat{n}_i - 1) - \mu_{\text{eff}} \sum_i \hat{n}_i, \quad (60)$$

with the density-induced tunneling  $T$  mediated by boson–boson interaction (defined in equation (49)) and  $T_{BF} = g_{BF} \int d^3r w_i^{B*}(\mathbf{r}) w_i^F(\mathbf{r}) w_i^F(\mathbf{r}) w_j^B(\mathbf{r})$  mediated by the interspecies interaction. The interaction parameter is  $g_{BF} = \frac{2\pi\hbar^2}{m_r} a_{BF}$ , where  $m_r$  is the reduced mass and  $a_{BF}$  the interspecies scattering length. While the repulsive interaction between the bosons increases the total tunneling, the fermions reduce or enhance the bosonic mobility, depending on the

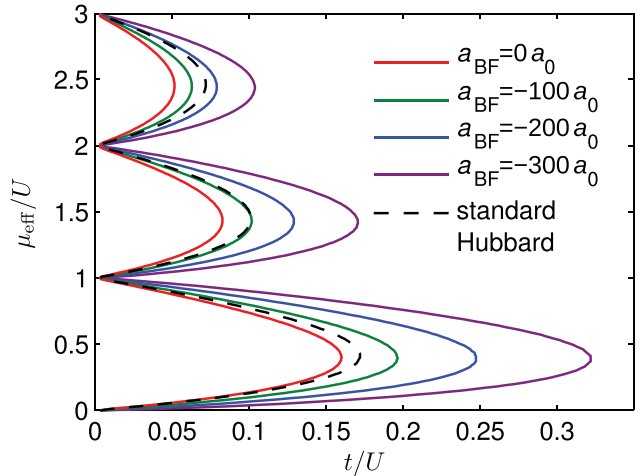


**Figure 15.** Phase diagram of the effective bosonic Hamiltonian (61) with density-induced tunneling for different Bose–Fermi scattering lengths,  $a_{BF}$ , within Gutzwiller mean-field theory. For comparison, the results from the standard Hubbard model are shown as a dashed black line. The calculation is performed for bosonic  $^{87}\text{Rb}$  and fermionic  $^{40}\text{K}$  in an optical lattice with a spacing of  $a = 377$  nm (experimental parameters of Best *et al* (2009)). For the wavelength considered, the Wannier functions of the two species are almost identical. The interaction between the bosonic atoms is fixed to a repulsive scattering length of  $a_{BB} = 102 a_0$  (Will *et al* 2010), while the attractive interaction between the two species is tunable over a wide range using a Feshbach resonance (Best *et al* 2009, Ferlaino *et al* 2006). This figure is from Jürgensen *et al* (2012).

sign of the boson–fermion interaction. As a consequence, and in strong contrast to the predictions of the standard Hubbard model, the superfluid–Mott insulator transition is affected and the phase boundaries are shifted depending on the interspecies interaction strength. The phase diagram is shown in figure 15 for different attractive Bose–Fermi interaction strengths. For strong Bose–Fermi attraction and low bosonic filling, the transition occurs at much shallower lattices, since the total tunneling is reduced. In the picture of an effective potential (see section 2.4.1), this corresponds to a deeper tunneling potential. The effect is reversed when the repulsion between the bosons becomes stronger than the attraction to the fermions, which is the case for weaker Bose–Fermi interaction and higher bosonic filling. In this case, the effective tunneling potential is shallower and tunneling is enhanced. The Mott insulator transition in Bose–Fermi systems is discussed further in section 4.6.

#### 4. Multi-orbital Hubbard models

Along with including the off-site interactions discussed in the last section, taking into account higher bands is an important extension of standard Bose–Hubbard models. In the Hubbard model, only the lowest single-particle band is assumed to be occupied, since higher bands are energetically separated. In strongly correlated systems, the interaction-induced coupling between the orbital bands is, however, strong enough that higher bands are mixed with the lowest band. Due to their dominating contribution to the total energy, the orbital occupation is determined by on-site interaction processes. Within

a mean-field treatment (section 4.2), the occupation of higher orbitals corresponds to a modified on-site wavefunction of the particles—in order to minimize the on-site interaction energy. Due to the population of higher orbitals, the effective wavefunction overlap on neighboring lattice sites also changes. As a consequence, the tunneling amplitude is modified and becomes occupation dependent.

First, we formulate a multi-orbital Hubbard model in order to define appropriate notation in section 4.1. After giving a mean-field description for the orbital degrees of freedom (section 4.2), the correlated many-particle on-site problem is discussed (section 4.3). The results can be used directly to compute the orbital dressing of off-site processes (section 4.5). This leads intrinsically to occupation-dependent Hamiltonians (section 4.6). Hubbard models in which particles are confined just to higher bands of the lattice are discussed in section 5. The analysis presented below is restricted to interacting bosons only, which have been studied in detail. Effects of higher bands for impurities embedded in a one-dimensional sea of fermions in a periodic potential were considered in Doggen *et al* (2014).

#### 4.1. Multi-orbital Hubbard models

Again the basic Hamiltonian in second quantization is given by equation (1). Now, however, we expand the atom field, taking excited bands explicitly into account:

$$\hat{\Psi}(\mathbf{r}) = \sum_{i,\alpha} \hat{b}_i^\alpha w_i^\alpha(\mathbf{r}), \quad (61)$$

where  $w_i^\alpha(\mathbf{r})$  is a Wannier function of the band  $\alpha$  localized at site  $i$  while  $\hat{b}_i^{\alpha\dagger}, \hat{b}_i^\alpha$  are the creation and annihilation operators for a boson at site  $i$  and energy band  $\alpha$ . The single-particle part of the Hamiltonian (1) yields tunnelings and energies in different orbitals:

$$t_{ij}^\alpha = - \int w_i^{\alpha*}(\mathbf{r}) \left[ -\frac{\hbar^2}{2m} \nabla^2 + V_{\text{ext}}(\mathbf{r}) \right] w_j^\alpha(\mathbf{r}) d\mathbf{r}, \quad (62)$$

$$\epsilon_i^\alpha = \int w_i^{\alpha*}(\mathbf{r}) \left[ -\frac{\hbar^2}{2m} \nabla^2 + V_{\text{ext}}(\mathbf{r}) \right] w_i^\alpha(\mathbf{r}) d\mathbf{r}. \quad (63)$$

Similarly, the interaction part of the Hamiltonian may be expressed as

$$H_{\text{int}} = \frac{1}{2} \sum_{\alpha\beta\gamma\delta} \sum_{ijkl} U_{ijkl}^{\alpha\beta\gamma\delta} \hat{b}_i^{\alpha\dagger} \hat{b}_j^{\beta\dagger} \hat{b}_k^\gamma \hat{b}_l^\delta, \quad (64)$$

with the interaction integrals

$$U_{ijkl}^{\alpha\beta\gamma\delta} = \int w_i^{\alpha*}(\mathbf{r}) w_j^{\beta*}(\mathbf{r}') V(\mathbf{r} - \mathbf{r}') w_k^\gamma(\mathbf{r}') w_l^\delta(\mathbf{r}) d\mathbf{r} d\mathbf{r}'. \quad (65)$$

Combining different terms, we obtain the multi-orbital Hubbard model in its full glory. The summations over site indices may be, as before, limited to nearest neighbors, but e.g. the tunneling between next-nearest-neighbor sites can also be included in the model, depending on the specific problem or lattice geometry.

The full description of lattice and orbital degrees of freedom captured in a multi-orbital Hubbard model leads to an extremely complex many-particle problem. Also, for very strong interactions it may lead to convergence problems (see discussions in e.g. Łącki *et al* (2013) and references therein). The goal of this section is therefore rather to define effective Hubbard models within a single band. This *interaction-dressed* band includes the orbital degrees of freedom and can be treated by common single-band methods for lattice models. The individual processes, such as on-site interaction, tunneling, and density-induced tunneling, are affected and renormalized by this treatment.

#### 4.2. Mean-field description of higher orbitals

As described in section 3, we find that different kinds of extensions of the Hubbard model become relevant when the interaction between the particles is enhanced, e.g. by means of a Feshbach resonance or by reducing the lattice constant. When the interaction is sufficiently weak compared to the lattice potential, the bosonic system can be approximately modeled using the lowest band single-particle Wannier states, which are localized at the minima of the lattice. Under these conditions, the Hubbard interaction  $U$  and tunneling parameter  $J$  are given by respective matrix elements with respect to the single-particle Wannier states. This approximation breaks down for stronger interaction as the interaction-induced coupling to higher energy Wannier states starts playing a role.

To describe such a system, one can introduce modified Wannier-like orbitals with a dependence on the lattice site occupation numbers  $n_j$ . Such Wannier-like orbitals will have admixtures from higher bands, depending on the occupation. The most significant effect of the repulsive interaction will be a broadening of the Wannier-like orbitals with increasing occupation, effectively enhancing  $J$  and decreasing  $U$ . One can take this into account, in terms of the Hubbard description, by replacing  $J$  and  $U$  by functions  $J_{\hat{n}_i, \hat{n}_j}$  and  $U_{\hat{n}_i}$  of the number operators  $\hat{n}_i$ . Quantitative consequences of this kind of modification of the plain bosonic Hubbard model have been studied by several authors at a theoretical level (Li *et al* 2006, Johnson *et al* 2009, Hazzard and Mueller 2010, Dutta *et al* 2011). Considering an interaction-induced modification of the Wannier functions, additional Mott insulator phases have also been predicted (Alon *et al* 2005b). A variational time-dependent approach in which Wannier functions adapt dynamically to lattice dynamics and interactions has been proposed (Sakmann *et al* 2011). Unfortunately this original approach does not take the interaction-induced multi-particle entanglement efficiently into account, being, at the present stage, inferior to the multi-orbital expansion (Major *et al* 2014). In (Larson *et al* 2009), the effect of the interaction-induced coupling to the first excited band on the Mott transition was considered. Re-entrant behavior in the superfluid-Mott transition has also been predicted, due to the interaction-induced modification of Hubbard parameters (Larson *et al* 2009, Cetoli and Lundh 2010). The effects of

interaction on the tunneling dynamics in one-dimensional double-well and triple-well potentials have been studied, e.g. in Cao *et al* (2011) and Zöllner *et al* (2008) where the authors found enhanced correlated pair tunneling near the fermionization limit.

For bosons with contact interaction, we rewrite the total Hamiltonian in terms of the field operators as

$$\hat{H} = \int \hat{\Psi}^\dagger(\mathbf{r}) \left[ -\frac{\hbar^2}{2m} \nabla^2 + V_{\text{ext}} \right] \hat{\Psi}(\mathbf{r}) + \frac{g}{2} \int \hat{\Psi}^\dagger(\mathbf{r}) \hat{\Psi}^\dagger(\mathbf{r}) \hat{\Psi}(\mathbf{r}) \hat{\Psi}(\mathbf{r}) d\mathbf{r}. \quad (66)$$

To derive a Hubbard-type description, the field operators  $\hat{\Psi}(\mathbf{r})$  are expanded in terms of Wannier-like orbitals  $\omega_i(\mathbf{r}, \hat{n}_i) = \omega(\mathbf{r} - \mathbf{R}_i, \hat{n}_i)$  localized at the lattice minima  $\mathbf{R}_i$ , namely  $\hat{\Psi}(\mathbf{r}) = \sum_i \hat{b}_i \omega_i(\mathbf{r}, \hat{n}_i)$  with bosonic annihilation and number operators  $\hat{b}_i$  and  $\hat{n}_i = \hat{b}_i^\dagger \hat{b}_i$ . Note that the ‘wavefunction’  $\omega_i$  depends on the number operator  $\hat{n}_i$ —in order to take into account interaction-induced occupation-dependent broadening. Keeping only the on-site interaction, as well as the density-induced tunneling, we arrive at the effective single-band Hamiltonian

$$\hat{H} = - \sum_{\langle i,j \rangle} t_{\hat{n}_i, \hat{n}_j} \hat{b}_i^\dagger b_j - \sum_{\langle i,j \rangle} [T_{\hat{n}_i, \hat{n}_j}^1 \hat{b}_i^\dagger \hat{n}_i \hat{b}_j + T_{\hat{n}_i, \hat{n}_j}^2 \hat{b}_i^\dagger \hat{n}_j \hat{b}_j] + \frac{1}{2} \sum_i U_{\hat{n}_i} \hat{n}_i (\hat{n}_i - 1), \quad (67)$$

where

$$\begin{aligned} t_{\hat{n}_i, \hat{n}_j} &= - \int d\mathbf{r} \omega_i(\mathbf{r}, \hat{n}_i) \left[ -\frac{\hbar^2}{2m} \nabla^2 + V_{\text{ext}}(\mathbf{r}) \right] \omega_j(\mathbf{r}, \hat{n}_j + 1), \\ U_{\hat{n}_i} &= g \int d\mathbf{r} \omega_i^2(\mathbf{r}, \hat{n}_i) \omega_i^2(\mathbf{r}, \hat{n}_i - 1), \\ T_{\hat{n}_i, \hat{n}_j}^1 &= -g \int d\mathbf{r} \omega_i(\mathbf{r}, \hat{n}_i + 1) \omega_i^2(\mathbf{r}, \hat{n}_i) \omega_j(\mathbf{r}, \hat{n}_j), \\ T_{\hat{n}_i, \hat{n}_j}^2 &= -g \int d\mathbf{r} \omega_i(\mathbf{r}, \hat{n}_i + 1) \omega_j^2(\mathbf{r}, \hat{n}_j - 1) \omega_j(\mathbf{r}, \hat{n}_j). \end{aligned} \quad (68)$$

In order to estimate the occupation number dependence of the effective Wannier functions, we express them as

$$\omega_i(\mathbf{r}, \hat{n}_i) = \frac{1}{\sqrt{\mathcal{N}_{\hat{n}_i, \hat{n}_j}}} \left[ \phi_i(\mathbf{r}, \hat{n}_i) - \sum_{\langle j \rangle} \mathcal{A}_{\hat{n}_i, \hat{n}_j} \phi_j(\mathbf{r}, \hat{n}_j) \right], \quad (69)$$

where in a mean-field treatment we make a Gaussian ansatz for the localized wavefunctions at site  $i$  with occupation number operator  $\hat{n}_i$ :  $\phi(\mathbf{r} - \mathbf{R}_i, \hat{n}_i) = \frac{1}{\pi^{3/4} d^{3/2}(\hat{n}_i)} \exp(-(\mathbf{r} - \mathbf{R}_i)^2/d^2(\hat{n}_i))$ , and the width  $d(\hat{n}_i)$  is a variational parameter depending on the particle number  $n_i$  (Chiofalo *et al* 2000, Vignolo *et al* 2003, Schaff *et al* 2010). We introduced  $\mathcal{A}_{\hat{n}_i, \hat{n}_j}$  to fulfill the requirement that the effective Wannier functions at neighboring sites are orthogonal, whereas  $\mathcal{N}_{\hat{n}_i, \hat{n}_j}$  takes care of the normalization of the Wannier functions. A more rigorous, fully correlated treatment can be found in section 4.5.

For deep enough lattice depths, we can assume that the width is much smaller than the lattice constant, i.e.  $a/d(n_i) \gg 1$ . Consequently, one can define the function for the overlap between Gaussians centered at neighboring sites as

$$\begin{aligned} \mathcal{S}_{\hat{n}_i, \hat{n}_j} &= \int d\mathbf{r} \phi_i(\mathbf{r}, \hat{n}_i) \phi_j(\mathbf{r}, \hat{n}_j) \\ &= \left[ \frac{2d(\hat{n}_i)d(\hat{n}_j)}{d^2(\hat{n}_i) + d^2(\hat{n}_j)} \right]^{3/2} \exp \left\{ -\frac{a^2}{2[d^2(\hat{n}_i) + d^2(\hat{n}_j)]} \right\}. \end{aligned} \quad (70)$$

In the limit of  $\mathcal{S}_{\hat{n}_i, \hat{n}_j} \ll 1$ , from the orthonormalization constraints, one gets

$$\mathcal{A}_{\hat{n}_i, \hat{n}_j} = 1 - \sqrt{1 - \mathcal{S}_{\hat{n}_i, \hat{n}_j}}, \quad (71)$$

$$\mathcal{N}_{\hat{n}_i, \hat{n}_j}^{-2} = 1 - 2 \sum_{\langle j \rangle} \mathcal{A}_{\hat{n}_i, \hat{n}_j} \mathcal{S}_{\hat{n}_i, \hat{n}_j} + \sum_{\langle j \rangle} \mathcal{A}_{\hat{n}_i, \hat{n}_j}^2. \quad (72)$$

To find the occupation-dependent width of the site-centered Gaussian  $\phi(\mathbf{r} - \mathbf{R}_i, n_i)$ , we minimize the Gross–Pitaevskii energy functional. Taking into account the full lattice potential (i.e. not employing a quadratic approximation for the lattice minima), for a given  $n_i$  this leads to

$$\begin{aligned} &\left[ \frac{d(n_i)}{d_0} \right]^5 \exp \left[ -\pi^2 \frac{d^2(n_i)}{a^2} \right] \\ &= \frac{d(n_i)}{d_0} + \sqrt{2\pi} \left[ \frac{V_0}{E_R} \right]^{1/4} \frac{a_s}{a} (n_i - 1). \end{aligned} \quad (73)$$

We have introduced  $d_0/a = [V_0/E_R]^{-1/4}/\pi$  for the width of  $\phi$  in the limit  $V_0 \gg E_R$ . Note that equation (73) has a solution only as long as  $\sqrt{V_0/E_R} \gg d^2(n_i)/d_0^2$ .

#### 4.3. Multi-orbital on-site interaction

The on-site energy  $U$  in the Hubbard model represents the interaction energy of particles on the same lattice site, calculated using the Wannier function of the lowest band. It is clear, however, that the respective wavefunction is not an eigenfunction of the single-site problem with interactions, since repulsive interaction broadens and attractive interaction narrows the on-site density. In the language of orbitals, this corresponds to the admixture of higher orbitals with the lowest orbital. The occupation of higher orbitals is dependent on the particle number and is a function of the interaction strength and lattice depth. For bosonic atoms in optical lattices, the occupation-dependent population of higher orbitals can be observed experimentally via spectroscopy measurements (Campbell *et al* 2006, Bakr *et al* 2011, Mark *et al* 2011, Mark *et al* 2012) and via a quantum phase evolution measurement (figure 16) after a sudden quench of the lattice depth (Will *et al* 2010). For two-component fermionic atoms, modulation spectroscopy has been used to measure the on-site interaction in a

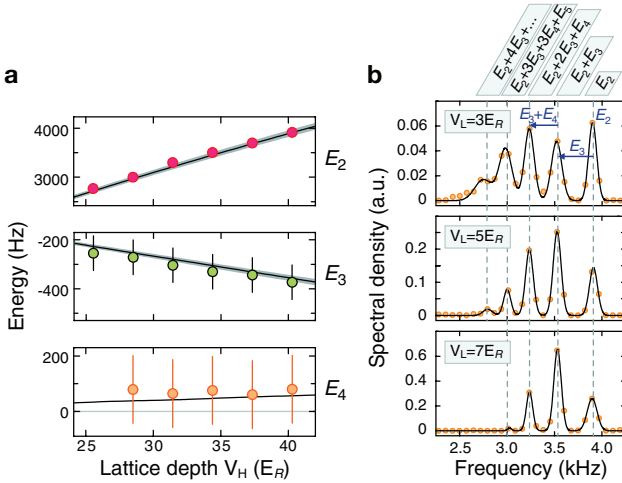


**Figure 16.** The occupation dependence of the on-site energy  $U_n$  due to the population of higher orbitals was observed in a collapse and revival experiment (Will *et al* 2010). (a) Effective multi-body interaction energies  $E_n$  obtained using the expansion (77) as a function of the final lattice depth  $V_H$  after the quench, where the circles correspond to the measured values ( $V_L = 8 E_R$ ). The lines are theoretical predictions obtained using exact diagonalization in a many-particle basis (equation (75)). (b) The experimental energies are determined by Fourier transformation of time-resolved traces ( $V_H = 40 E_R$ ), where the relative peak height depends on the number distribution of the superfluid state in the shallow lattice  $V_L$ . The dashed gray lines show the theoretical values. This figure is from Will *et al* (2010).

honeycomb lattice. For large interactions, the on-site interaction deviates from the theoretical single-particle on-site interaction computed from the honeycomb Wannier functions indicating the influence of higher bands (Uehlinger *et al* 2013). Theoretically, the occupation dependence has been studied using mean-field approaches (Li *et al* 2006, Hazzard and Mueller 2010, Dutta *et al* 2011), field theoretical methods (Johnson *et al* 2009), variational approaches (Sakmann *et al* 2011, Major *et al* 2014), direct-space quantum Monte Carlo methods (Pilati and Troyer 2012), and different kinds of diagonalization approaches (Busch *et al* 1998, Büchler 2010, Bissbort *et al* 2012, Lühmann *et al* 2012, Łacki *et al* 2013).

In the simplified case of two atoms with contact interaction in the harmonic confinement, the Schrödinger equation can be solved exactly (Busch *et al* 1998). While the  $\delta$  interaction potential for neutral atoms is easily applied to the single-band problem, it must be treated with care when dealing with an (infinite) orbital degree of freedom, since the corresponding Hamiltonian is not self-adjoint for dimensions higher than 1. For two or three dimensions, a regularized  $\delta$  potential can be used to circumvent this problem. In Busch *et al* (1998), analytical expressions for the energy and the wavefunctions are derived. The great advantage of the harmonic oscillator potential is the separability in relative and center-of-mass coordinates. Transferring these results directly to optical lattices is problematic: while the Gaussian is a reasonable approximation for the lowest band

Wannier function of a lattice site when dealing with on-site properties, higher band Wannier functions differ strongly from their harmonic counterpart. As the regularization in Busch *et al* (1998) explicitly accounts for the infinite series of higher orbital wavefunctions, the results cannot be transferred quantitatively.

To circumvent the subtleties of the  $\delta$  potential, different kinds of interaction potentials can be applied. In Büchler (2010), the two channels of the Feshbach resonance are modeled in order to solve the problem using the Bloch functions of the optical lattice. By comparison with the standard Bose–Hubbard model, this allows one to obtain the multi-orbital on-site energy. The great advantage of this treatment is that it directly models the experimental technique for tuning the interaction strength. A simpler approach is to use a model interaction potential of finite range, where one has to ensure that the results depend only weakly on the specific shape of the potential (Lühmann *et al* 2012, Pilati and Troyer 2012). Note that the finite range of the potentials leads to a high energy cutoff, since fast oscillating wavefunctions of very high orbitals are averaged out within the interaction integrals. Note that for scattering resonances the assumption of an interaction potential of finite range may break down. Numerically, a scaling with respect to the number of orbitals can be applied to predict the actual value of the problem with an infinite number of orbitals (Büchler 2010, Jürgensen *et al* 2012, Łacki *et al* 2013).

For short-ranged interaction potentials  $V(\mathbf{r} - \mathbf{r}')$ , we can write the on-site problem for  $n$  particles in a local many-particle Fock basis with states  $|N\rangle = |n_0, n_1, \dots\rangle$ , where  $n_\alpha$  is the number of particles in orbital  $\alpha$ . Dropping the site index, the orbitals are the Wannier functions and the Hamiltonian for a single lattice site reads (compare (64))

$$\hat{H}_{\text{site}} = \sum_{\alpha} e^{\alpha} \hat{n}^{\alpha} + \frac{1}{2} \sum_{\alpha\beta\gamma\delta} U^{\alpha\beta\gamma\delta} \hat{b}^{\dagger\alpha} \hat{b}^{\dagger\beta} \hat{b}^{\gamma} \hat{b}^{\delta}, \quad (74)$$

where  $\hat{n}^{\alpha} = \hat{b}^{\alpha\dagger} \hat{b}^{\alpha}$ ,  $\hat{b}^{\alpha\dagger}$  creates and  $\hat{b}^{\alpha}$  annihilates a particle in the Wannier orbital  $\alpha$  with single-particle energies  $e^{\alpha}$ . The interaction integrals are given in equation (65). The many-particle ground state for  $n$  particles

$$|\Psi(n)\rangle = \sum_N c_N(n) |N(n)\rangle \quad (75)$$

is a superposition of local Fock states with  $n$  particles and real coefficients  $c_N(n)$ . While for the non-interacting ground state  $|\Psi_0(n)\rangle = |n, 0, 0, \dots\rangle$ , all atoms occupy the single-particle ground state, the interaction promotes particles also to higher orbitals. On the mean-field level, the change of the single-site wavefunction is attributed to an interaction broadening of the density.

However, the significant change of the many-particle state lies also within modified higher order correlations, allowing the particles to mutually reduce their spatial overlap (Bissbort *et al* 2012). Therefore, this effect cannot be captured on an effective single-particle level. The eigenvalues  $e_n$  of the

Hamiltonian equation (74) for  $n$  particles directly relate to the multi-orbital on-site energy  $U_n$  per particle pair via

$$U_n = \frac{2}{n(n-1)} e_n. \quad (76)$$

This is the occupation-dependent on-site energy for an effective Hubbard model. Note that the on-site energy decreases with the number of particles, i.e.  $U_{n+1} < U_n$ . From a different point of view, the occupation-dependent on-site energy can be understood as effective  $n$ -body collisions with energies  $E_n$  (Johnson *et al* 2009, Will *et al* 2010, Bissbort *et al* 2012). Expanded in terms of  $n$ -body collisions, the on-site energy for  $n$  particles can be written as

$$\begin{aligned} U_n = & \frac{E_2}{2} n(n-1) + \frac{E_3}{6} n(n-1)(n-2) \\ & + \frac{E_4}{24} n(n-1)(n-2)(n-3) + \dots \end{aligned} \quad (77)$$

Using the occupation-dependent energies  $U_n$ , we can set  $E_2 = U_2$ ,  $E_3 = 3U_3 - 3E_2$ ,  $E_4 = 6U_4 - 6E_2 - 4E_3$ , ... . The differences between the occupation-dependent energies  $U_n$  have been observed in a collapse and revival experiment with bosonic atoms after a quench from a shallow lattice ( $V_L$ ) to a deep lattice ( $V_H$ ) (Will *et al* 2010). The local particle number distribution in the superfluid regime, which is Poissonian or number squeezed depending on the lattice depth  $V_L$ , is preserved during the quench. The time evolution of the matter wave field  $\psi = \langle \phi(t) | \hat{b} | \phi(t) \rangle$  in the deep lattice reflects the occupation dependence of the on-site energy (76) via

$$|\psi|^2 = \sum_{n,m=0}^{\infty} C_{n,m} e^{-i(e_{n+1}-e_n-e_{m+1}+e_m)t/\hbar}, \quad (78)$$

where the relative contribution  $C_{n,m}$  depends on the particle number distribution in the superfluid state. In figure 16, the results are shown as effective  $n$ -body collision energies  $E_n$ .

#### 4.4. Bose–Hubbard models with local three-body interaction

Truncating the effective description of (77) to the first two terms, one may build a particular Bose–Hubbard model with local three-body interactions, with the Hamiltonian

$$\begin{aligned} \hat{H} = & -t \sum_{\langle i,j \rangle} \hat{b}_i^\dagger \hat{b}_j + \frac{U}{2} \sum_i \hat{n}_i (\hat{n}_i - 1) \\ & + \frac{W}{6} \sum_i \hat{n}_i (\hat{n}_i - 1)(\hat{n}_i - 2) - \mu \sum_i \hat{n}_i, \end{aligned} \quad (79)$$

where  $\mu$  is the chemical potential fixing the particle number. While for contact interaction (compare figure 16(a)) the strengths of the two-body and three-body terms may be modified in a limited range by changing the lattice depth and geometry, one may assume that the three-body term controlled by  $W$  can be experimentally tuned independently of the two-body term  $U$  (e.g. for dipolar or other kinds of interactions). It is in

fact for polar molecules in optical lattices that such a three-body potential term was introduced (Büchler *et al* 2007). The following quantum Monte Carlo study (Schmidt *et al* 2008) revealed the existence of both solid and supersolid phases in the system. Another early discussion of the model (79) was done at the mean-field level in Chen *et al* (2008). It was shown that, depending on the three-body term, the second insulating lobe ( $\rho = 2$ ) changes its area. In contrast, the first insulating lobe ( $\rho = 1$ ) is insensitive to the three-body interactions. These results are intuitively straightforward. It is clear that for  $\rho = 2$ , in contrast to the  $\rho = 1$  case, tunneling has to compete not only with two-body interactions but also with three-body interactions to destroy the insulating phase. A pedagogical explanation of these facts and a comparison with the Gutzwiller mean-field approach was presented recently in Sowiński and Chhajlany (2014).

A more precise discussion of the model was given for the one-dimensional case. First, using the DMRG approach (Silva-Valencia and Souza 2011), it was shown that for a strong enough three-body term the first insulating lobe, in contrast to what is predicted by mean-field results, changes its shape and the tip of the lobe is shifted. However, the transition from the MI to the SF phase remains in the Berezinskii–Kosterlitz–Thouless (BKT) universality class. In Sowiński (2012b), these results were supported with exact diagonalization calculations, and the extension to an attractive three-body term was proposed (see figure 17). Independently, a two-dimensional system with strong three-body attraction was studied using a quantum Monte Carlo approach in Safavi-Naini *et al* (2012). In addition, some effects of finite temperatures were discussed in that article. Recently, a summary of properties of the one-dimensional model (79), on the basis of the dynamical DMRG method, was also presented in Ejima *et al* (2013).

Further extensions of the model (79) have also been studied. In particular, (i) an extension adopting long-range dipole–dipole interactions was proposed and discussed in Zhou *et al* (2010); (ii) a discussion of the influence of a magnetic field on the properties of the model was provided in Huang and Wan (2010); (iii) additional effects arising in a superlattice potential were studied using mean-field and DMRG approaches in Singh *et al* (2012).

Finally, it is worth noting that the seemingly exotic version of the model (79) with a vanishing two-body term  $U = 0$  has also been discussed in detail in Silva-Valencia and Souza (2012), Sowiński (2014), where the one-dimensional case has been addressed using DMRG calculations. For that model, the first insulating lobe for  $\rho = 1$  vanishes and the stability of higher Mott lobes increases with increasing filling  $\rho$ . As previously, in the vicinity of the phase transition the system remains in the BKT universality class.

Another proposition (Daley *et al* 2009) considers an attractive two-body term  $U < 0$  and strong three-body repulsion, a model which may mimic strong three-body losses. In Lee and Yang (2010), it was shown that for vanishing tunnelings and filling  $0 < \rho < 2$ , an additional pair superfluid phase is present in the system. With increasing tunneling, the system

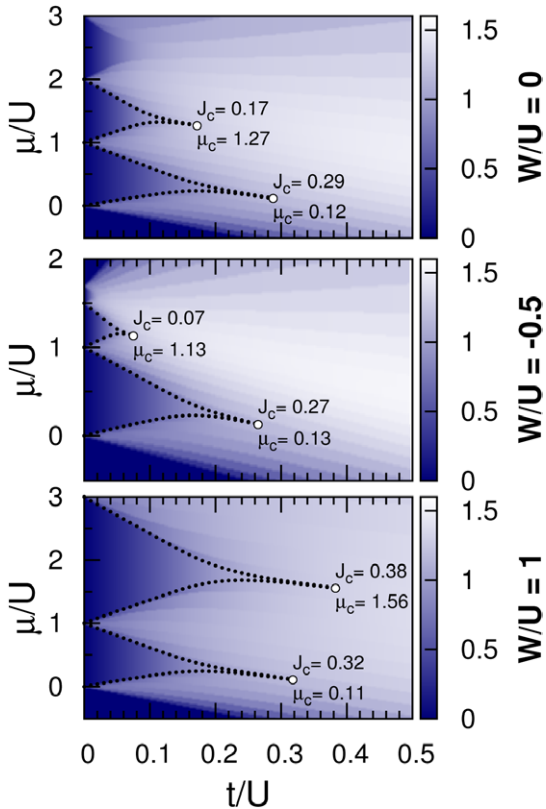


**Figure 17.** The phase diagrams of the one-dimensional system described by the Hamiltonian (79) for different values of the three-body interactions  $W$ . Open circles mark the transition from the MI to the SF phase, as estimated from the exact diagonalization of small systems and extrapolated to the thermodynamic limit. In the background of each phase diagram, the density plots of the correlation function  $\langle \hat{a}_i^\dagger \hat{a}_j \rangle$  are visualized. For  $\rho = 1$ , the insulating phase does not change significantly, but for  $\rho = 2$  the size of the MI phase crucially depends on the three-body interaction parameter. This figure was adapted from Sowiński (2012b).

undergoes a second-order phase transition to a normal SF phase. On this basis, in Sowiński *et al* (2013b) the model with large but finite repulsive  $W$  was discussed, where it was shown that the critical exponents and the central charge governing the quantum phase transition have repulsion-dependent features. In consequence, the model (79) with attractive two-body and repulsive three-body interactions extends the list of known systems violating the universality hypothesis. While some of these models seem unrealistic at first, it is also known how to control the relative strength of three-body interactions, as exemplified in Mazza *et al* (2010) for Raman-induced couplings. A more recent work (Daley and Simon 2013) has shown how to engineer practically at will three-body interactions via photon-assisted tunneling.

#### *4.5. Multi-orbital dressing of off-site processes*

While the last section shows how on-site properties, i.e. the on-site wavefunction and the energy  $U$ , are influenced by orbital degrees of freedom, in the following their impact on off-site properties is discussed. As a result of the population

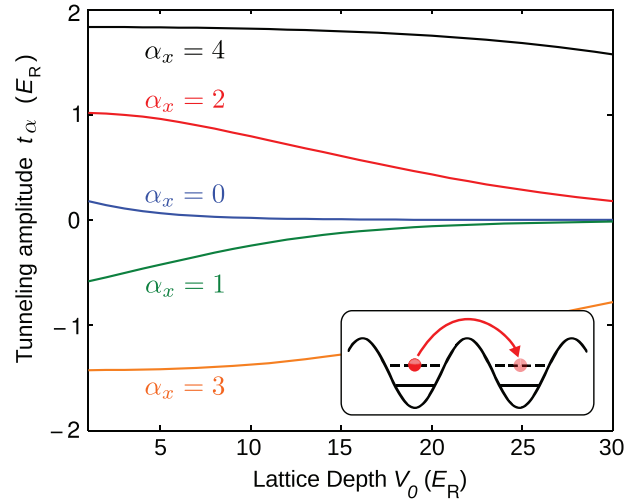


**Figure 18.** Single-particle tunneling matrix elements  $t^\alpha$  for the lowest five bands (denoted by  $\alpha_i$ ) as a function of the lattice depth  $V_0$ . This figure is from Lühmann *et al* (2012).

of higher orbitals, the effective wavefunction overlap of particles on neighboring lattice sites changes. This leads to modified amplitudes of the tunneling and the off-site interactions (section 3.2). Since the occupation of higher orbitals is typically a few per cent or lower, one would expect the effect on the hopping to be only marginal. However, as shown in figure 18 the tunneling matrix elements  $t^\alpha$  in higher bands can be exponentially large compared with the lowest band ones. Therefore, the tunneling in higher orbitals can have a large net effect on the total tunneling amplitude. In optical lattices, the effects of bosonic tunneling in higher bands were discussed by using variational mean-field methods (Li *et al* 2006, Larson *et al* 2009, Hazzard and Mueller 2010, Dutta *et al* 2011) (see section 4.2) and by using numerical exact methods mainly restricted either to double-well or to triple-well systems; see e.g. Cao *et al* (2011), Sakmann *et al* (2009) and (2010). The effect was also discussed for experiments with Bose–Fermi mixtures (Lühmann *et al* 2008, Lutchyn *et al* 2009, Mering and Fleischhauer 2011, Jürgensen *et al* 2012).

When dealing with both lattice and orbital degrees of freedom, one could be tempted to formulate the multi-orbital Hubbard model, i.e.

$$\hat{H} = - \sum_{\langle i,j \rangle, \alpha} t^{\alpha} \hat{b}_i^{\alpha\dagger} \hat{b}_j^{\alpha} + \sum_{i,\alpha} e^{\alpha} \hat{n}_i^{\alpha} + \frac{1}{2} \sum_{i,\alpha\beta\gamma\delta} U^{\alpha\beta\gamma\delta} \hat{b}_i^{\alpha\dagger} \hat{b}_i^{\beta\dagger} \hat{b}_i^{\gamma} \hat{b}_i^{\delta} \quad (80)$$

(compare with equation (74)). Here,  $t^{\alpha}$  is the amplitude for tunneling between neighboring sites  $i$  and  $j$  in band  $\alpha$ , (62). Although this model is already a strong simplification of the full two-body Hamiltonian (64), as it disregards any off-site interactions, the complexity of this problem is enormous. The idea is therefore to switch from the non-interacting basis to a basis that is more adapted as regards the interactions. This basis is constructed from the solution of the multi-orbital

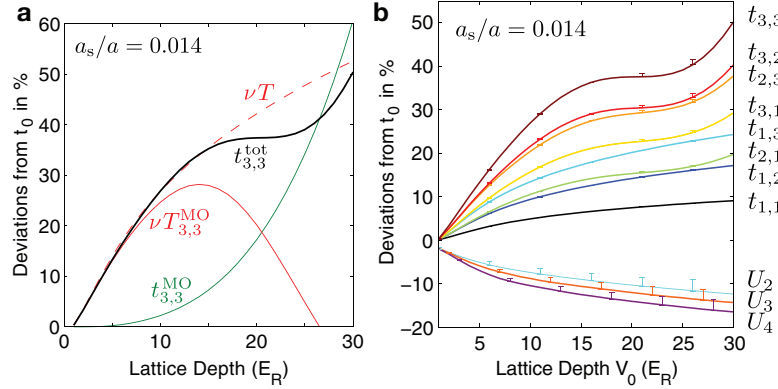


**Figure 19.** (a) Contributions to the effective tunneling  $t_{n_i,n_i}^{\text{tot}}$  with  $n_i = n_j = 3$  from the multi-orbital tunneling  $t_{n_i,n_i}$ , density-induced tunneling  $T$ , and multi-orbital density-induced tunneling  $T_{n_i,n_i}$ , where the latter two scale with the prefactor  $\nu = n_i + n_j - 1$ . The total tunneling is the sum of the two multi-orbital-dressed processes. The plot shows the deviations from the single-particle tunneling  $t_0$  as a function of the lattice depth  $V_0$ . (b) Occupation-dependent total tunneling  $t_{n_i,n_i}^{\text{tot}}$  and on-site interactions  $U_n$  for a box-shaped interaction potential (with a width  $W = 5$  nm and a lattice constant  $a = 377$  nm). The results are only weakly affected by changes in the scattering potential (error bars correspond to  $W = 25$  nm). This figure is from Lühmann *et al* (2012).

on-site problem (74) as described in Bissbort *et al* (2012), Jürgensen *et al* (2012) and Lühmann *et al* (2012). Since we restrict the single-site solutions to just the lowest energy state, we truncate the basis thereby to a single band, which is constructed from correlated single-site states (75). By construction, the second term and the third term of equation (80) are diagonal in this basis. In particular, the on-site interaction in the *dressed band* is given by (the operators within the dressed band are denoted with a tilde)

$$\sum_i U_{\tilde{n}_i} \tilde{n}_i (\tilde{n}_i - 1). \quad (81)$$

The on-site interaction parameter, which is occupation dependent, can be expressed formally as a projection  $U_{\tilde{n}_i} = \mathcal{P}_i^\dagger \sum_n U_n |\tilde{n}\rangle_i \langle \tilde{n}|_i \mathcal{P}_i$ . Here, the  $U_n$  are the eigenenergies normalized per particle pair (76), and  $\mathcal{P}_i$  projects the many-site state to site  $i$ .

It is important to note that other processes such as the multi-orbital tunneling matrix element are also transformed in the dressed basis. Since the orbital dressing is a basis transformation that is block diagonal with respect to the particle subspaces, the usual commutation relations  $[\tilde{b}_i, \tilde{b}_j^\dagger] = \delta_{ij}$  are fulfilled. The appropriate procedure of the transformation to the interaction-dressed basis is described in appendix A. From a practical point of view, it is important that once the Hamiltonian is expressed in the dressed basis it remains a single-band lattice problem (compare equation (82)). It is inherently occupation dependent, but has otherwise the same complexity as the single-band Hubbard Hamiltonian. The dressed band model allows one to apply standard single-band methods to calculate the phase diagram, e.g. the mean-field and quantum Monte Carlo approaches.

#### 4.6. Multi-orbital occupation-dependent Hamiltonians

The multi-orbital dressing of both interactions and the tunneling leads to intrinsically occupation-dependent Hubbard models. As discussed in sections 4.3 and 4.5, the multi-orbital

renormalization of the on-site interaction, tunneling and other off-site processes causes the amplitudes to depend on the particle numbers at the participating sites. In optical lattices, the multi-orbital corrections can be of the same order of magnitude as the density-induced tunneling, as discussed in section 3.2. Therefore, the combination of the two effects is essential for a correct description.

In the multi-orbital dressed band (section 4.5), the occupation-dependent Hamiltonian for bosons in an optical lattice is given by Lühmann *et al* (2012)

$$\hat{H} = - \sum_{\langle i,j \rangle} \tilde{b}_i^\dagger \tilde{b}_j t_{\tilde{n}_i, \tilde{n}_j} - \sum_{\langle i,j \rangle} \tilde{b}_i^\dagger (\tilde{n}_i + \tilde{n}_j) \tilde{b}_j T_{\tilde{n}_i, \tilde{n}_j} + \frac{1}{2} \sum_i U_{\tilde{n}_i} \tilde{n}_i (\tilde{n}_i - 1), \quad (82)$$

where the second term represents the density-induced tunneling (see equation (47) with  $V, P = 0$ ). The total tunneling consists of normal and density-induced tunnelings. Both processes effectively include higher orbital processes. For a given occupation of lattice sites  $i$  and  $j$ , the total tunneling can be evaluated as

$$t_{n_i, n_j}^{\text{tot}} = t_{n_i, n_i} + (n_i + n_j - 1) T_{n_i, n_i}, \quad (83)$$

where its individual contributions are shown in figure 19(a) as a function of the lattice depth. Note that both the density-induced tunneling and the amount of multi-orbital corrections scale with the interaction strength. In shallow lattices, the multi-orbital renormalization of the tunneling and bond-charge tunneling is in general weak and becomes substantial only at intermediate lattice depths ( $V_0 \gtrsim 15 E_R$ ). Interestingly, the higher orbital contributions of the tunneling and bond-charge interaction partly compensate each other at intermediate lattice depths. Figure 19(b) demonstrates the occupation dependence of the total tunneling amplitude  $J_{n_i, n_i}^{\text{tot}}$  for different occupations  $n_i$  and  $n_j$ .

Using perturbative mean-field theory (van Oosten *et al* 2001), occupation-dependent amplitudes such as  $t_{n_i \pm 1, n_i}^{\text{tot}}$  must

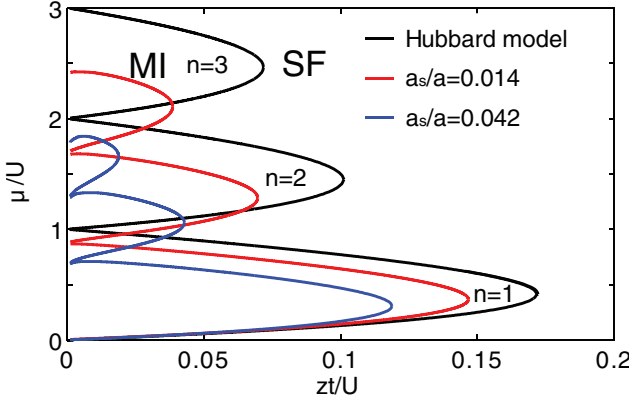


**Figure 20.** Phase diagrams showing the transition from the superfluid (SF) to the Mott insulator (MI) for the generalized multi-orbital-dressed Hubbard Hamiltonian (82) in the Gutzwiller approximation. The phase boundaries are plotted for the interaction strengths  $a_s/a = 0.014$  (red,  $^{87}\text{Rb}$  parameters) and  $a_s/a = 0.042$  (blue) as well as for the Bose–Hubbard model (black). This figure is from Lühmann *et al* (2012).

be approximated by  $t_{n_i,n_i}^{\text{tot}}$ . However, Gutzwiller calculations for the ground state without this restriction give very similar results. The phase diagram is shown in figure 20 for two different interaction strengths  $a_s$  as a function of  $zt/U$ , where  $z = 6$  is the number of nearest neighbors for three-dimensional cubic lattices. The superfluid phase is enlarged for repulsive interactions and the tips of the Mott lobes are shifted towards smaller values of  $zt/U$ . This corresponds to a significant shift of the critical lattice depth of the superfluid–Mott insulator transition due to an effectively increased tunneling and reduced on-site interaction. The deformation along the  $\mu/U$  axis is due to the occupation-dependent on-site interaction  $U_n$ . Phase diagrams for 1D and 2D lattices are computed in Łęcki *et al* (2013) using mean-field methods and the time-evolving block decimation algorithm (TEBD) in 1D. The corresponding phase diagram is shown in figure 21, where the Mott lobes are affected in the same way as in the mean-field treatment. In addition to the band-dressing technique discussed here, direct-space quantum Monte Carlo methods have also been applied using different interaction potentials (Pilati and Troyer 2012). Experimentally, the shift of this transition has been studied for a filling  $n = 1$  and tunable interactions (Mark *et al* 2011). In general, however, the shift is considerably more pronounced for higher fillings since the density-induced tunneling and the multi-orbital renormalization scale with the particle number.

Bose–Fermi mixtures also allow for occupation-dependent models, for which the effects of higher bands were discussed in Jürgensen *et al* (2012), Lühmann *et al* (2008), Lutchyn *et al* (2009) and Mering and Fleischhauer (2011). Here, the on-site energy (section 4.3) and multi-orbital dressing of the tunneling (section 4.5) must be treated in a many-particle product basis of  $n$  bosons and  $n_F$  fermions. In addition, density-induced tunneling  $T$  (boson assisted) and  $T_{\text{BF}}$  (fermion assisted) also crucially affect the phase diagram, as discussed in section 3.4. Therefore, it is important to treat the two effects at the same time (Mering and Fleischhauer 2011, Jürgensen *et al* 2012). Using the simplification of a fermionic band insulator ( $n_F = 1$ ), where all fermionic degrees of freedom are frozen

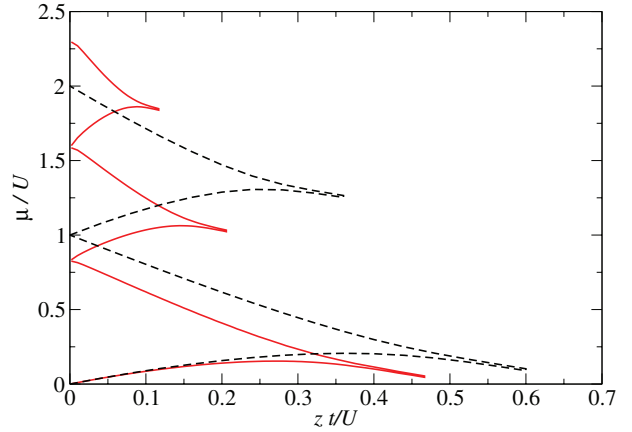


**Figure 21.** Superfluid–Mott insulator transition in one dimension for the generalized Hubbard Hamiltonian (82) including density-induced tunneling and multi-orbital effects (solid red line). The phase diagram is obtained by means of a TEBD algorithm with 100 lattice sites for an interaction strength  $a_s/a = 0.014$  and a vertical confinement of  $34.8 E_R$ . The dashed black line corresponds to the Bose–Hubbard model. This figure is from Łęcki *et al* (2013).

out, the system can be described using an effectively bosonic Hamiltonian (see equation (60)):

$$\begin{aligned} \widetilde{H} = & - \sum_{\langle i,j \rangle} \tilde{b}_i^\dagger \tilde{b}_j (t_{\tilde{n}_j, \tilde{n}_i} + 2T_{\text{BF}, \tilde{n}_j, \tilde{n}_i}) - \sum_{\langle i,j \rangle} \tilde{b}_i^\dagger (\tilde{n}_i + \tilde{n}_j) \tilde{b}_j T_{\tilde{n}_j, \tilde{n}_i} \\ & + \sum_i E_{\tilde{n}_i} - \mu \sum_i \tilde{n}_i. \end{aligned} \quad (84)$$

In this case, the on-site energy for  $n$  bosons is given by

$$E_n = n\epsilon_{B,n} + \epsilon_{F,n} + \frac{1}{2}n(n-1)U_n + nU_{\text{BF},n}, \quad (85)$$

containing the occupation-dependent (repulsive) energies of interaction between the bosons  $U_n$  and (attractive) energies of interaction between bosons and fermions  $U_{\text{BF},n}$  as well as the single-particle energies  $\epsilon_{B,n}$  and  $\epsilon_{F,n}$  of the higher orbitals. In analogy with the purely bosonic system case, the critical point of the superfluid–Mott insulator transition is affected. The phase diagram and the critical lattice depth are shown for an  $^{87}\text{Rb}$ – $^{40}\text{K}$  mixture in figure 22. In the standard Bose–Fermi–Hubbard model the transition does not depend on the boson–fermion interaction (dashed lines in figure 22(b)), whereas the generalized occupation-dependent Hamiltonian predicts a strong dependence on the interspecies scattering length. This strong shift of the superfluid–Mott insulator transition was also observed experimentally (Günter *et al* 2006, Ospelkaus *et al* 2006b, Best *et al* 2009). In Best *et al* (2009), the interspecies interaction  $a_{\text{BF}}$  was tuned via a Feshbach resonance, which allows observing the shift of the Mott transition point as a function of the interspecies interaction. The transition point shown in figure 23 was obtained by measuring the condensate fraction of  $^{87}\text{Rb}$ . For  $a_{\text{BF}} < 200a_0$  the experiment finds a shift of the transition which is even stronger than theoretically expected (figure 22(b)). However, for  $a_{\text{BF}} < 200a_0$  the experiment observes also a strong increase in the particle loss, indicating additional processes such as a redistribution of the bosonic atoms. Note that the experimental lattice ramping

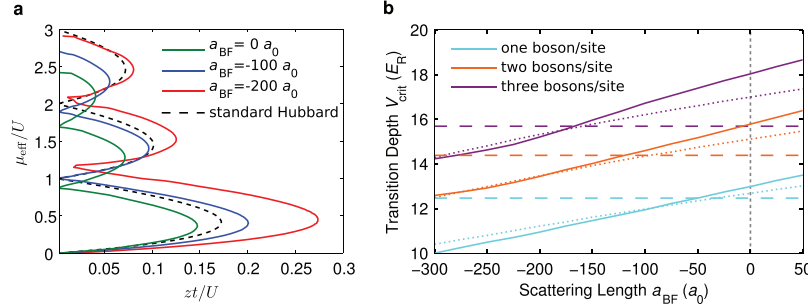


**Figure 22.** (a) Phase diagram for the superfluid-Mott insulator transition of bosons interacting attractively with a fermionic band insulator. The predictions of the standard Hubbard models are shown as a dashed black line. The attractive interaction effectively reduces the total tunneling and extends Mott insulating phases, depending on the interspecies scattering length  $a_{BF}$ . (b) The critical lattice depth of the superfluid-Mott insulator transition as a function of the interspecies scattering length  $a_{BF}$ . The transition occurs for significantly shallower lattices than in the purely bosonic system ( $a_{BF} = 0$ ). The dashed lines correspond to the standard Bose–Fermi–Hubbard model (59) and the dotted lines to the generalized lowest band model (60) with density-induced tunneling given in section 3.4. This figure is from Jürgensen *et al* (2012).

procedure can also cause a drop of the bosonic coherence due to an adiabatic heating. The latter is caused by different contributions of the atomic species to the total entropy (Cramer *et al* 2008, Cramer 2011). For repulsive interaction, one would expect a phase separation of bosonic and fermionic atoms when the interspecies interaction exceeds the intraspecies interaction of the bosons. Hence, if the interspecies interaction is large enough, the bosonic Mott transition is no longer influenced directly by the presence of the fermions. However, the redistribution of bosonic atoms possibly causes higher bosonic filling factors and thereby affects the transition point.

## 5. Hubbard models based on excited bands

Up to now, we have restricted our considerations to a single band, and took effects of higher bands into account only in an effective theory. However, by actively exploiting these higher bands, one may open access to studying orbital physics in optical lattices, with exciting prospects, as reviewed in Wu (2009) and Lewenstein and Liu (2011): multi-orbital physics can lead to unconventional superfluid states (Stojanovic *et al* 2008, Cai and Wu 2011, Wirth *et al* 2010, Ölschläger *et al* 2011, Ölschläger *et al* 2013, Soltan-Panahi *et al* 2012), or additional Mott insulator phases where atoms localize after undergoing a Tonks–Girardeau-like transition (Alon *et al* 2005). Manipulating atoms in higher bands, one may also induce various topological phenomena (Wu 2008b, Sun *et al* 2012, Li *et al* 2013), and one can go beyond the integer quantum Hall effect that may be obtained in the s orbitals of an optical honeycomb lattice subject to a synthetic gauge field (Goldman *et al* 2010, Kitagawa 2010, Alba *et al* 2011, Hauke *et al* 2012b)—in the flat p bands of such a lattice, exotic incompressible states analogous to the Laughlin fractional quantum Hall liquid can be created (Wu *et al* 2007, Chern and Wu 2011, Li *et al* 2014). Several groups have now achieved loading and manipulating ultracold atoms in higher (such as p) bands (Browaeys *et al* 2005, Köhl 2005, Anderlini *et al* 2007, Müller *et al* 2007, Ölschläger *et al* 2011, Ölschläger *et al* 2012, Ölschläger *et al* 2013, Wirth *et al* 2010). Techniques such as lattice ramping and using radio frequency pulses have

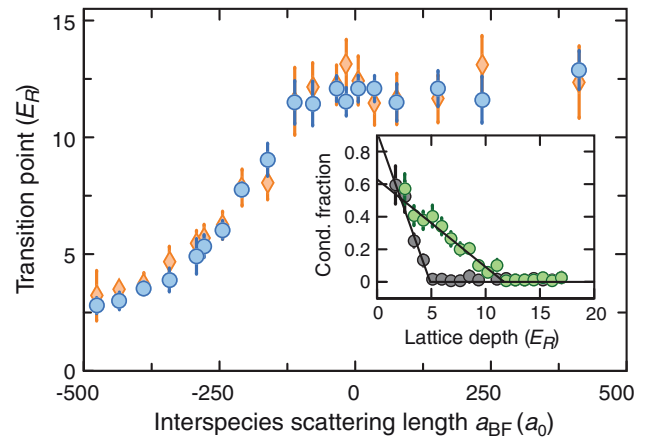


**Figure 23.** Superfluid-Mott insulator transition in a mixture of bosonic  $^{87}\text{Rb}$  and fermionic  $^{40}\text{K}$  atoms, where the interspecies interaction  $a_{BF}$  was tuned by using a Feshbach resonance. The diamonds and circles represent experimental results for the ratios 0.5 and 0.75 of  $^{40}\text{K}$  to  $^{87}\text{Rb}$  atoms, respectively. The transition point has been determined as the point of vanishing condensate fraction of  $^{87}\text{Rb}$  (inset). This figure is from Best *et al* (2009).

been used to transfer atoms from the s band to higher bands. There, they can stay in a metastable state for a long time, allowing a detailed study of the effects of orbital degeneracy.

In a broader context, such studies may give important insight into the behavior of strongly correlated electrons in solid-state samples. In many materials, such as transition metal oxides (Tokura and Nagaosa 2000), orbital effects play a fundamental role, being responsible for several important material properties such as colossal magnetoresistance, ferroelectricity, unconventional superconductivity, and charge ordering. In many instances, novel quantum phases emerge due to the coupling of the orbital degree of freedom to the charge, spin, or lattice degrees of freedom (Kugel and Khomskii 1982, Khaliullin 2005). However, such coupling not only generates interesting effects, but also complicates the theoretical treatment. It is, therefore, desirable to study simpler systems in which the orbital degree of freedom is decoupled from all others. Here, ultracold atoms provide an ideal tool; loaded into higher bands of optical lattices, they allow one to analyze

orbital dynamics in a well controlled environment, including orbital-only models of single-species (spinless) fermions.

### 5.1. A three-color p band Hubbard model for optical lattices

As a first illustrative example of a non-standard Hubbard model for higher bands, we review in this section a three-color model describing spinless fermions in the p band orbitals of an optical lattice close to an optical Feshbach resonance. The model considered already hosts unconventional phases in the simple cubic lattice—such as a phase with ‘axial orbital order’ in which  $p_z$  and  $p_x + i p_y$  (or  $p_x - i p_y$ ) orbitals alternate, thus breaking spatial symmetry and time-reversal symmetry (Hauke *et al* 2011).

To derive the Hubbard model for ultracold atoms in higher optical lattice bands, one can proceed like in the derivation of the standard Hubbard model of spinless particles, equation (14), explained in section 2.2. Generalizing equation (13), we expand the field operators in the Wannier basis of the higher band:

$$\hat{\Psi}(\mathbf{r}) = \sum_{i=1}^N \sum_{\mu=x,y,z} w_i^\mu(\mathbf{r}) \hat{f}_i^\mu. \quad (86)$$

Here, the operator  $\hat{f}_i^\mu$  destroys a fermion in the orbital  $p_\mu$  at site  $i$ . The corresponding Wannier function  $w_i^\mu(\mathbf{r})$  is a product of the  $p_\mu$  function for  $\mu$  and the lowest s functions for remaining directions. Using this expansion, the dynamics of ultracold atoms in higher optical lattice bands can be described using the non-standard Hubbard model:

$$\begin{aligned} \hat{H} = & - \sum_{i=1}^N \sum_{\mu,\nu=x,y,z} t_{\mu,\nu} (\hat{f}_i^{\mu\dagger} \hat{f}_{i+\mathbf{e}_\nu}^\mu + \text{h.c.}) \\ & + \sum_{i=1}^N \sum_{\mu,\nu,\mu',\nu'=x,y,z} V_{\mu,\nu,\mu',\nu'} \hat{f}_i^{\mu\dagger} \hat{f}_i^{\nu\dagger} \hat{f}_{i+\mathbf{e}_\nu}^{\mu'} \hat{f}_{i+\mathbf{e}_\nu}^{\nu'}. \end{aligned} \quad (87)$$

The geometry that we consider here is a simple cubic lattice with spacing set to 1, and with unit vector  $\mathbf{e}_\nu$  in direction  $\nu = x, y, z$ . The nearest-neighbor tunneling matrix element  $t_{\mu,\nu}$  describes the hopping of fermions in orbital  $p_\mu$  along the direction  $\mathbf{e}_\nu$ . As illustrated in figure 24, due to the odd parity of p orbital Wannier wavefunctions, this tunneling does not couple orbitals with different principal axes. In conjunction with the anisotropy of the p orbital, the tunneling becomes direction and orbital dependent (Isacsson and Girvin 2005, Kuklov 2006, Liu and Wu 2006):  $t_{\mu,\nu} = t_{\parallel} \delta_{\mu,\nu} + t_{\perp} (1 - \delta_{\mu,\nu})$ . This spatial dependence is responsible for a good part of the rich physics of ultracold atoms in higher bands.

Additionally, Hamiltonian (87) contains an on-site inter-orbital interaction term  $V_{\mu,\nu,\mu',\nu'}$ . Typically, the interaction between fermionic atoms at low temperatures is weak. The reason is that the Pauli exclusion principle only allows scattering in high partial wave channels (p, f, etc), which are suppressed at low temperatures due to the angular momentum barrier. To realize strongly correlated phases, however, strong fermion–fermion interactions are desirable. One way to increase the elastic scattering cross-section is to employ

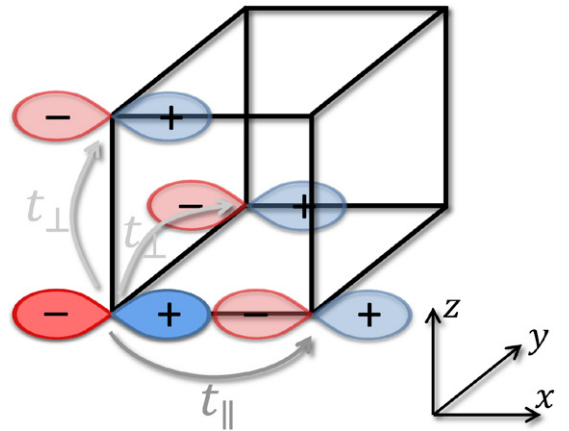


**Figure 24.** Orbital tunneling, exemplified for the  $p_x$  orbital. Due to the odd parity of p orbitals (indicated by ‘−’ (red) and ‘+’ (blue)), a fermion in a given  $p_x$  orbital (solid dumbbell) can tunnel only into neighboring  $p_x$  orbitals (semi-transparent dumbbells). Since the hopping amplitude is given by the overlap of the anisotropic p Wannier functions, one has typically  $|t_{\parallel}| \gg |t_{\perp}|$ , with  $t_{\parallel} = t_{x,x}$  and  $t_{\perp} = t_{x,y} = t_{x,z}$ . Moreover, the odd parity results in different signs:  $\text{sgn}(t_{\perp}) = -\text{sgn}(t_{\parallel})$ .

a Feshbach resonance (FR) (Chin *et al* 2010). Typically, the FRs are generated by coupling channels in the electronic ground state through magnetic fields. For the case of p waves, however, this method usually leads to significant atom losses through three-body inelastic collisions (Regal *et al* 2003, Zhang *et al* 2004, Günter *et al* 2005, Schunck *et al* 2005).

As discussed in Goyal *et al* (2010) and Hauke *et al* (2011), optical Feshbach resonances (OFRs) (Theis *et al* 2004, Thalhammer *et al* 2005) should allow one to enhance the p wave scattering cross-section while avoiding strong losses due to three-body recombination. Additionally, the OFR provides for a high degree of control, since, e.g. one can adjust the ratio of interaction strengths among different p orbitals. In contrast to the approach of previous sections such as section 3.2, here a regime where the interactions remain sufficiently small to allow the neglect of off-site contributions is considered.

In Hauke *et al* (2011), it was shown that in this case Hamiltonian (87) takes the form

$$\begin{aligned} \hat{H} = & - \sum_{i=1}^N \sum_{\mu,\nu=x,y,z} t_{\mu,\nu} (\hat{f}_i^{\mu\dagger} \hat{f}_{i+\mathbf{e}_\nu}^\mu + \text{h.c.}) \\ & + \sum_{i=1}^N \left[ V_1 \hat{n}_i^x \hat{n}_i^y + V_2 (\hat{n}_i^x \hat{n}_i^z + \hat{n}_i^y \hat{n}_i^z) + (iV_3 \hat{f}_i^x \hat{f}_i^y \hat{n}_i^z + \text{h.c.}) \right]. \end{aligned} \quad (88)$$

Here,  $\hat{n}_i^\mu = \hat{f}_i^{\mu\dagger} \hat{f}_i^\mu$  is the number operator for fermions in orbital  $\mu$  at site  $i$ . Due to the OFR, the relative strengths and signs of  $V_{1,2,3}$  can be varied by changing the detuning of the OFR laser or the strength of a Zeeman splitting between internal atomic states. The terms  $V_1$  and  $V_2$  denote usual on-site density–density interactions. Additionally, the OFR leads to the orbital-changing term  $V_3$ . Physically, it transforms  $p_x$  into  $p_y$  particles (and vice versa). This allows them to explore the entire  $xy$  plane, instead of being confined to a one-dimensional line, as is usually the case as long as  $t_{\perp}$  can be neglected (Zhao and Liu 2008).

Hamiltonian (87) generalizes the Hubbard-like models of Miyatake *et al* (2009), Rapp *et al* (2008, 2007), Tóth *et al* (2010), Wu (2008) and Zhao and Liu (2008). For the special case of  $V_1 = V_2$  and  $V_3 = 0$ , Hamiltonian (87) reduces to the SU(3)-symmetric Hubbard model. One can visualize p band fermions as particles carrying a color index representing the  $p_x$ ,  $p_y$ , and  $p_z$  orbital states. Then, Hamiltonian (87) describes a three-color fermion model with color-dependent interaction  $V_{1,2}$ , a novel color-changing term  $V_3$ , and spatially anisotropic and color-dependent tunneling  $t_{\mu, \nu}$ . Since the  $V_3$  term explicitly breaks time-reversal symmetry (TRS), we can expect it to lead to novel phases reflecting that intriguing property that lies at the heart of the topological insulator states (Hasan and Kane 2010).

An important limiting case of Hamiltonian (87) is the one where interactions dominate over tunneling terms: the so-called strong coupling limit. In Hubbard models of spinful s band fermions, this limit leads to the emergence of Heisenberg and  $t - J$  models, which are relevant for high  $T_c$  superconductivity. Unlike for these situations, in the case of atoms in the p band of the optical lattice three orbital states instead of two spin states are involved.

In the strong coupling limit of Hamiltonian (87),

$$|t_{\parallel}| \ll V_1, \quad |t_{\parallel}| \ll V_2 - V_3, \quad \text{and} \quad |t_{\parallel}| \ll V_2 + V_3, \quad (89)$$

at the average p band filling of 1/3, the low energy manifold consists of states with one p band particle per site. Since  $|t_{\perp}| \ll |t_{\parallel}| \equiv t$ , one can safely neglect the perpendicular tunneling  $t_{\perp}$  in this limit (Zhao and Liu 2008).

The low energy states are coupled via virtual hopping that induces exchange interactions between nearest-neighbor orbitals (see figure 25). The resulting physics within the low energy manifold is captured in an effective Hamiltonian that can be derived from second-order perturbation theory. Following this approach and treating the tunneling  $t$  in (87) as a perturbation, one obtains the effective Hamiltonian for the low energy manifold at 1/3 filling:

$$\begin{aligned} \hat{H}_{\text{eff}} = & - \sum_i \left\{ \sum_{\mu=x,y,z} J_{\mu} \hat{n}_i^{\mu} (2 - \hat{n}_{i+\mu}^{\mu} - \hat{n}_{i-\mu}^{\mu}) \right. \\ & + \sum_{\mu=x,y} (J_2 - J_1) \hat{n}_i^{\mu} (\hat{n}_{i+\mu}^z + \hat{n}_{i-\mu}^z) \\ & \left. + J_3 [\hat{f}_i^{y\dagger} \hat{f}_i^x (\hat{n}_{i+z}^z + \hat{n}_{i-z}^z) + \text{h.c.}] \right\}. \end{aligned} \quad (90)$$

The resulting model is characterized by nearest-neighbor orbital interactions and the ‘correlated orbital-flipping’ term,  $\sim J_3$ . To write this model more compactly, we have used  $\hat{n}_i^x + \hat{n}_i^y + \hat{n}_i^z = 1$ , and defined

$$J_1 = t^2/V_1, \quad (91)$$

$$J_2 = t^2 V_2 / (V_2^2 - V_3^2), \quad (92)$$

$$J_3 = t^2 V_3 / (V_2^2 - V_3^2), \quad (93)$$

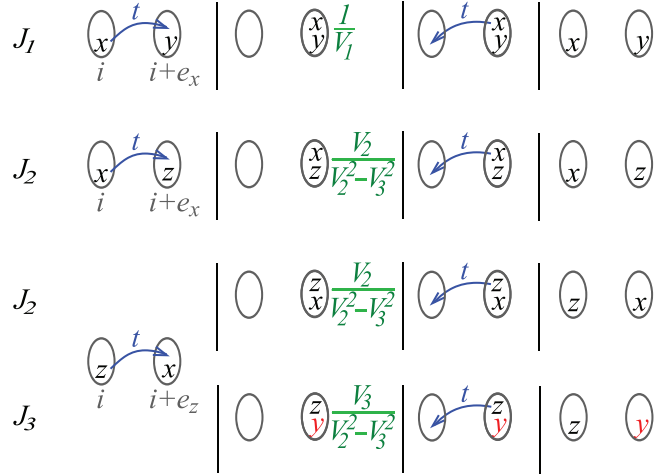


**Figure 25.** Sketch of the virtual hopping processes at p band filling 1/3 (one p band particle per site) leading to the effective Hamiltonian (90). If neighboring particles are in different orbitals  $p_{\mu}$  and  $p_{\nu}$  (abbreviated as  $\mu$  and  $\nu$ , respectively), and if they are connected by a bond in the  $\mu$  or  $\nu$  direction, a particle can tunnel with amplitude  $t$  (blue) to a neighboring site (leftmost column). There, it experiences on-site interaction (green processes, second column). Due to the anisotropic tunneling, only the same particle can tunnel back (third column). Rightmost column: for the processes  $J_1$  and  $J_2$ , the final configuration is the same as the initial one, but in the orbital-changing process  $J_3$  an  $x$  particle has changed into a  $y$  particle (bottom sketch). Neglecting  $t_{\perp}$ , the sketched processes—plus the ones obtained by interchanging  $x$  and  $y$ —are the only ones that can occur. This figure is from Hauke *et al* (2011).

as well as  $J_x = J_y = J_1, J_z = J_2$ . For  $V_3 = 0, V_1 = V_2$ , Hamiltonian (90) reduces to terms of the form  $J_{\mu} \hat{n}_i^{\mu} \hat{n}_{i+\mu}^{\mu}$ , a hallmark of the quantum three-state Potts model<sup>13</sup>.

For positive couplings  $J_{1,2}$ , the first term of Hamiltonian (90) favors any configuration where the orbitals at neighboring sites differ, while for negative  $J_{1,2}$  it favors configurations where the orbitals at neighboring sites are equal. The second term favors a pattern alternating between  $p_z$  particles and particles that are not  $p_z$  if  $J_2 > J_1$ , and a pattern alternating between  $p_x$  and  $p_y$  if  $J_2 < J_1$ . The competition between these terms leads to the appearance of three different phases; see the phase diagram in figure 26:

- (a) For  $J_1 > J_2 + |J_3|/2$  and  $J_1 > 0$ , the system is in an *antiferro-orbital* phase: in each  $xy$  plane, sites with  $p_x$  and  $p_y$  orbitals alternate; see figure 26, bottom right (this is similar to an antiferromagnetic Néel state in spin systems). Since  $p_x$  and  $p_y$  particles do not tunnel in the  $z$  direction, the  $x-y$  planes are decoupled. This phase has also been found in the two-dimensional model considered in Zhao and Liu (2008), where  $J_3 = 0$ .
- (b) For  $J_1 < J_2 + |J_3|/2$  and  $J_2 > -|J_3|/2$ , the ground state shows *axial orbital order*. The state is bipartite with  $|p_z\rangle$  on one sublattice and  $(|p_x\rangle \pm i|p_y\rangle)/\sqrt{2}$  (for  $J_3 \gtrless 0$ , respectively) on the other sublattice (see the right panel of figure 26). The state  $(|p_x\rangle \pm i|p_y\rangle)/\sqrt{2}$  has *finite angular momentum*, whence this novel phase breaks TRS. At  $J_3 = 0$ , any superposition between  $|p_x\rangle$  and  $|p_y\rangle$  is degenerate, and TRS is restored.

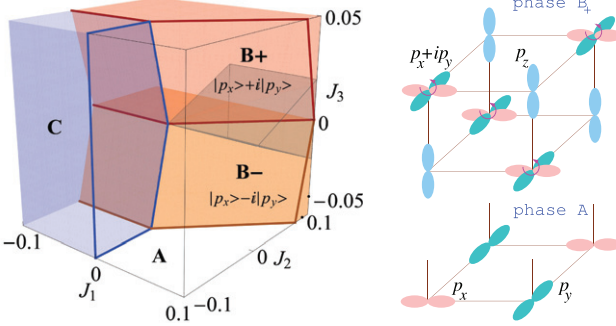


**Figure 26.** Left: phase diagram of the p band Hubbard model, equation (90), at filling 1/3. One finds four phases: phase A with antiferro-orbital order (empty region), phases B<sub>+</sub> and B<sub>-</sub> with axial orbital order (red/orange, for  $J_3 \gtrless 0$ ), and phase C (blue) with tunneling completely frozen. The gray wedge indicates the region satisfying the strong coupling conditions (89). Right: sketch of phases A and B<sub>+</sub>. In phase B<sub>+</sub>,  $|p_z\rangle$  and  $|p_x\rangle + i|p_y\rangle$  orbitals alternate. Phase B<sub>-</sub> can be visualized from this by replacing  $|p_x\rangle + i|p_y\rangle$  with  $|p_x\rangle - i|p_y\rangle$ . This figure is from Hauke *et al* (2011).

- (c) For the case  $J_1 < 0$  and  $J_2 < -|J_3|/2$ , the ground state is highly degenerate, consisting of any configuration where  $\alpha\beta$  planes are filled uniformly with  $p_\alpha$  or  $p_\beta$ , where  $\alpha\beta = xy, xz, yz$ , thus preventing any tunneling. This phase, however, is not physical, as it does not fulfill the strong coupling requirements (89).

As shown in Hauke *et al* (2011), the characteristic shape of the p band orbitals provides a direct possibility for distinguishing the different phases experimentally. Due to the non-trivial p orbital Wannier functions, signatures of the distinct phases appear in the momentum distribution that can be observed in standard time-of-flight images. Other complex orbital configurations can be obtained even for  $J_3 = 0$  by considering non-cubic lattices such as triangular or kagome lattices, where frustration effects decrease ordering tendencies (Zhao and Liu 2008). These can be detected in, for example, noise–noise correlation functions.

As demonstrated by the simple example of spinless fermions in a cubic lattice, non-standard orbital Hubbard models allow for the exploration of exotic phenomena, such as time-reversal symmetry breaking. At interfaces of two domains with opposite symmetry breaking, i.e.  $p_x + i p_y$  and  $p_x - i p_y$ , chiral zero-mode fermions may arise, similar to the edge states in spin Hall insulators (Hasan and Kane 2010). In the above example, the time-reversal symmetry was broken due to the  $J_3$  term that appeared as a consequence of using an optical Feshbach resonance to enhance interactions. However, as discussed in the next section, non-standard orbital Hubbard models offer also the possibility of observing the *spontaneous* formation of topological states (Li *et al* 2012, Sowiński *et al* 2013), adding an exciting new direction to the research on higher bands of optical lattices.

## 5.2. Time-reversal symmetry breaking of p orbital bosons

In a recent proposal, Li and co-workers addressed the possibility of achieving spontaneous breaking of time-reversal

symmetry using  $p_x$  and  $p_y$  orbitals in a one-dimensional lattice (Li *et al* 2012). This interesting construction may be realized assuming an optical lattice potential of the form

$$V_{\text{ext}}(\mathbf{r}) = V_x \sin^2(\pi x/a_x) + V_y \sin^2(\pi y/a_y) + \frac{m\Omega^2}{2}z^2, \quad (94)$$

for a highly non-symmetric lattice with  $V_y \gg V_x$ . Assuming that  $V_x/a_x^2 = V_y/a_y^2$ , within the harmonic approximation for the lattice sites the  $p_x$  and  $p_y$  orbitals are degenerate (Li *et al* 2012). The asymmetric lattice depths and different lattice constants ensure that the tunneling in the  $y$  direction is suppressed and that the system consists of a one-dimensional chain of quasi-isotropic sites. In this arrangement, the tunnelings for  $p_x$  and  $p_y$  orbitals in the  $x$  direction differ in sign and in magnitude. The p orbital bosons in such a lattice are argued to remain metastable (with a slow decay to s orbitals), like in double-well experiments (Wirth *et al* 2010).

The Hubbard-like Hamiltonian obtained using appropriate Wannier functions (the product of Wannier functions in the  $x$  and  $y$  directions as well as the ground state of the harmonic oscillator in the  $z$  direction) reads (Sowiński *et al* 2013a)

$$\hat{\mathcal{H}} = \sum_j \hat{H}(j) - \sum_{\langle ij \rangle} [t_x \hat{a}_x^\dagger(i) \hat{a}_x(j) + t_y \hat{a}_y^\dagger(i) \hat{a}_y(j)]. \quad (95)$$

Here, the local, on-site Hamiltonian  $\hat{H}(j)$  has the form

$$\begin{aligned} \hat{H}(j) = & \sum_{\alpha=x,y} \left[ E_\alpha \hat{n}_\alpha(j) + \frac{U_{\alpha\alpha}}{2} \hat{n}_\alpha(j)(\hat{n}_\alpha(j) - 1) \right] \\ & + \frac{U_{xy}}{2} [4\hat{n}_x(j)\hat{n}_y(j) + \hat{a}_x^\dagger(j)^2 \hat{a}_y(j)^2 + \hat{a}_y^\dagger(j)^2 \hat{a}_x(j)^2]. \end{aligned} \quad (96)$$

All cases of  $U$  represent contact interactions between different orbitals, and  $E_x$  and  $E_y$  are single-particle energies. The Hamiltonian commutes with the operator for the total number of particles,  $\hat{N} = \hat{N}_x + \hat{N}_y$ , where  $\hat{N}_\alpha = \sum_i \hat{n}_\alpha(i)$  (this is not valid for  $\hat{N}_x$  and  $\hat{N}_y$  separately, due to the last two terms in (96), which transfer pairs of bosons between different orbitals). Thus the Hamiltonian has a global  $Z_2$  symmetry related to the parity of the operator  $\hat{N}_y$  (choosing  $\hat{N}_x$  leads to the same conclusions), and it commutes with the symmetry operator  $S = \exp(i\pi \hat{N}_y)$ .

On introducing circular annihilation operators,  $\hat{a}_\pm(j) = [\hat{a}_x(j) \pm i\hat{a}_y(j)]/\sqrt{2}$ , the local part of the Hamiltonian (95) can be written in the form

$$\begin{aligned} \hat{H}(j) = & \frac{U}{2} \left[ \hat{n}(j) \left( \hat{n}(j) - \frac{2}{3} \right) - \frac{1}{3} \hat{L}_z^2(j) \right] \\ & + \delta[(\hat{n}(j) - 1)(\hat{L}_+(j) + \hat{L}_-(j))] \\ & + \lambda \left[ \frac{1}{4} \hat{L}_z^2(j) - 3(\hat{L}_+(j) - \hat{L}_-(j))^2 - \hat{n}(j) \right], \end{aligned} \quad (97)$$

where  $U = (U_{xx} + U_{yy})/2$ ,  $\delta = (U_{xx} - U_{yy})/2$ , and  $\lambda = U_{xy} - U/3$  with  $\hat{n}(j) = \hat{a}_+^\dagger(j)\hat{a}_+(j) + \hat{a}_-^\dagger(j)\hat{a}_-(j)$ , and angular momentum operators  $\hat{L}_z(j) = \hat{a}_+^\dagger(j)\hat{a}_+(j) - \hat{a}_-^\dagger(j)\hat{a}_-(j)$ ,  $\hat{L}_\pm(j) = \hat{a}_\pm^\dagger(j)\hat{a}_\mp(j)/2$ .

In the harmonic approximation, when the condition  $V_x/a_x^2 = V_y/a_y^2$  leading to orbital degeneracy is fulfilled, one

has  $E_x = E_y$ , and considerable simplifications occur. In particular,  $U_{xx} = U_{yy} = 3U_{xy} = U$ , independently of the lattice depth. Thus,  $\delta = \lambda = 0$  and  $[\hat{H}(j), \hat{L}_z(j)] = 0$  (i.e. eigenvalues of  $\hat{L}_z(j)$  become good quantum numbers). This is no longer true when proper Wannier functions are used. Even for deep optical lattices this leads to important differences between the two approaches. Let us concentrate on the case of the site filling of  $3/2$ , as discussed in Li *et al* (2012) and Sowiński *et al* (2013). Consider the staggered angular momentum  $\tilde{L}_z = \sum_j (-1)^j \langle \hat{L}_z(j) \rangle$ , the  $Z_2$  symmetry order parameter (Li *et al* 2012). In the harmonic approximation (Li *et al* 2012), two superfluid phases are observed (see figure 27). For low tunneling, the system shows antiferro-orbital (AFO) order with a staggered orbital current of  $p_x \pm ip_y$  type, which spontaneously breaks time-reversal symmetry. With increasing tunneling strength, a phase transition to a paraorbital (PO) superfluid is observed, where the staggered angular momentum  $\tilde{L}_z$  vanishes.

Interestingly, a quite different picture emerges when ‘proper’ Wannier functions are used. Both  $\delta$  and  $\lambda$  in (97) become different from zero, and, as a result, one has  $[\hat{H}(j), \hat{L}_z(j)] \neq 0$ , breaking the local axial symmetry. In Sowiński *et al* (2013), the system has been studied via exact diagonalization for small systems of length  $L = 4, 6$ , and  $8$  with periodic boundary conditions. The lowest energy states in two eigensubspaces of  $\mathcal{S}$  were found independently. Let us call these states  $|G_{\text{even}}\rangle$  and  $|G_{\text{odd}}\rangle$  with corresponding eigenenergies  $E_{\text{even}}$  and  $E_{\text{odd}}$  (subscripts even/odd correspond to even/odd numbers of bosons in orbital  $y$ ). The state with lower energy is the global ground state (GS) of the system. In principle, it may happen that both lowest states have the same energy. In such a case, any superposition  $\cos(\theta)|G_{\text{even}}\rangle + \sin(\theta)e^{i\varphi}|G_{\text{odd}}\rangle$  is a ground state of the system. In the thermodynamic limit, this  $U(1) \times U(1)$  symmetry is spontaneously broken to Ising-like  $Z_2$  symmetry and only one of the two macroscopic states can be realized (Sowiński *et al* 2013a).

Exact diagonalization in a harmonically approximated system gives for small tunnelings a degenerate GS, i.e.  $|G_{\text{even}}\rangle$  and  $|G_{\text{odd}}\rangle$  have the same energy, reproducing the results of Li *et al* (2012). When the anharmonicity of the lattice wells is included, the picture changes (figure 28(a)): for small tunnelings, the GS realizes an insulating state in the  $p_y$  orbital with one boson per site, and a fractional superfluid state in the  $p_x$  orbital. No significant correlation  $\langle \hat{a}_x^\dagger(j)\hat{a}_y(j) \rangle$  is found in this limit. In contrast, for large tunneling all particles occupy the  $p_x$  orbital in a superfluid phase, which is manifested by a large hopping correlation  $h_x$ , defined by

$$h_\alpha = \frac{1}{L} \sum_j \langle \hat{a}_\alpha^\dagger(j)\hat{a}_\alpha(j+1) \rangle, \quad (98)$$

where  $\alpha = x, y$ .

The most interesting physics arises for intermediate tunnelings. Figure 28(a) shows that there exists a particular tunneling value for which the two orbitals are equally populated. In the vicinity of this point, the GS is degenerate (figure 28(b)). More precisely, the degeneracy occurs exactly

<sup>13</sup> Orbital order in a simpler model without OFR, and its relation to the Potts model, were discussed by Wu in the unpublished version of Wu (2008b).

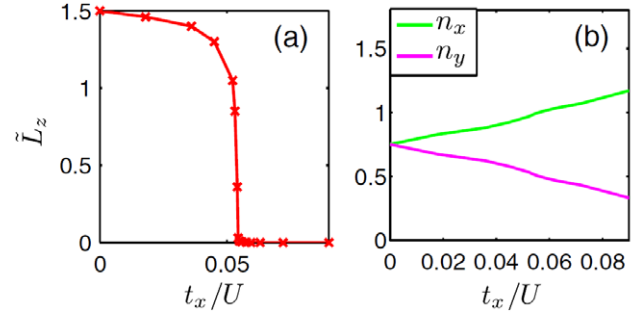


**Figure 27.** AFO–PO phase transition at filling  $3/2$  in the harmonic approximation. Panel (a) shows the staggered angular momentum ( $Z_2$  order parameter) as a function of the tunneling amplitude, for a fixed ratio  $|t_x/t_y| = 9$ . Panel (b) shows the filling of  $p_x$  and  $p_y$  orbitals. The numerical results were obtained using the DMRG. Reprinted figure, with permission, from Li *et al* 2012. Copyright (2012) by the American Physical Society.

for  $L$  different values of the tunneling within a certain finite range. The range of tunneling for which  $E_{\text{odd}} - E_{\text{even}} = 0$  does not grow with the lattice size, but saturates. This led the authors (Sowiński *et al* 2013a) to claim that in the thermodynamic limit the degeneracy of the ground state is dynamically recovered in a certain well defined range of tunnelings. In this region, whenever the tunneling is changed, one particle is transferred between orbitals to minimize the energy. Since there is no corresponding term in the Hamiltonian, this transfer is directly related to the flip from one eigensubspace of  $\mathcal{S}$  to the other.

In the region of recovered degeneracy, the two ground states  $|G_{\text{even}}\rangle$  and  $|G_{\text{odd}}\rangle$  have the same energy. However, in the thermodynamic limit, due to the einselection principle (Zurek 2003), the macroscopic state that is realized physically should exhibit as low an entanglement as possible. Minimizing the von Neumann entropy of the single-site density matrix, two orthogonal ground states  $|G_\pm\rangle = (|G_{\text{even}}\rangle \pm i|G_{\text{odd}}\rangle)/\sqrt{2}$  with the lowest entropy are found. Importantly, an independent DMRG calculation revealed that the staggered angular momentum takes non-zero values for the intermediate tunneling region (compare figure 28(b)).

As it turns out, the proper treatment using Wannier functions (and not their harmonic approximation) leads to tunneling-induced restoration of degeneracy and results in time-reversal symmetry breaking (Sowiński *et al* 2013a). The picture is quite different in the oversimplified harmonic approximation—even for deep lattices.

## 6. Hubbard models with dynamical spin

### 6.1. Mutual interactions of atomic magnets

Weak dipolar interactions of magnetic moments of atoms, such as chromium, erbium, or dysprosium, introduce some additional effects that are present only if the spins of the atoms are free. Then (as opposed to the case for frozen spins aligned along the direction of an external magnetic field), the dipole–dipole interactions couple the spins of the two particles to their orbital motion. As dipole–dipole interactions conserve

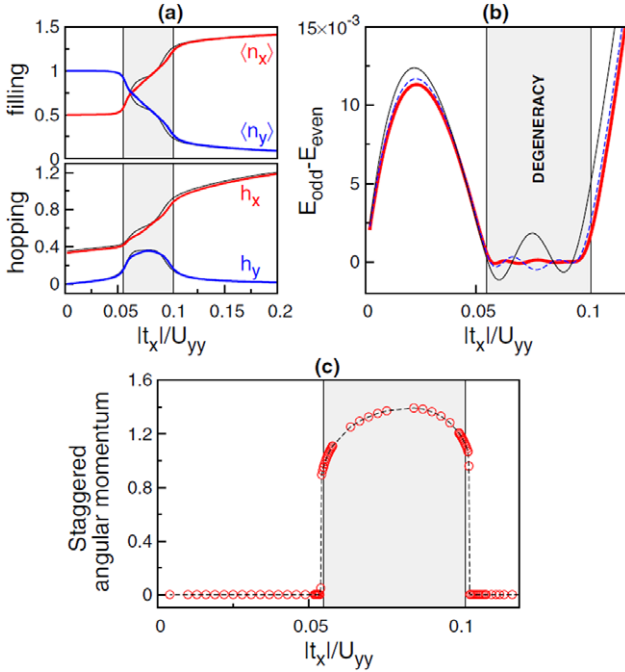


**Figure 28.** (a) Filling and hopping of the  $p_x$  (red line) and  $p_y$  (blue line) orbitals  $\nu = 3/2$  obtained with the ED method on a lattice with  $L = 6$  sites. The results agree with the corresponding results obtained for  $L = 4$  (thick black lines) and DMRG calculations (not shown, since they are practically indistinguishable from ED data). (b) The energy difference between the two ground states in even and odd subspaces of the eigenstates of the symmetry operator  $S$ . The energies are obtained with the ED method on the lattice with  $L = 4, 6$ , and  $8$  sites (thin black, dashed blue, and thick red lines, respectively). Note that corresponding lines cross the zero of energy  $L$  times. (c) Expectation value of the staggered angular momentum  $\hat{J}_z/L$  as a function of the tunneling obtained with the DMRG on the lattice with  $L = 64$  sites. A non-vanishing value of  $\hat{J}_z$  is present only in the region where the ground state is degenerate. In all figures the shaded region denotes the range of tunnelings where the ground state of the system is degenerate in the thermodynamic limit. Adapted from Sowiński *et al* (2013a).

the total angular momentum of interacting atoms, they do not conserve spin and orbital components separately. This simple observation leads directly to the Einstein-de Haas effect (Einstein and de Haas 1915, Kawaguchi *et al* 2006), which makes it possible to transfer spin to orbital angular momentum and vice versa. The effect is a macroscopic illustration of the fact that spin contributes to the total angular momentum of a system on the same footing as the orbital angular momentum, and it is the most spectacular manifestation of the spin dynamics driven by the dipolar interactions and coupled to the orbital motion.

In a more general case, when the axial symmetry condition is not met, the total angular momentum is not conserved. Spin-changing dipole-dipole interactions lead to a transfer of atoms from the ground to excited p or/and d states. In a lattice potential, such dipolar interactions with free spin couple the ground and excited bands of the lattice. Therefore, a very interesting class of Bose-Hubbard models appears naturally if spin-changing collisions are in play that do not conserve the total magnetization. The resulting necessity of taking

into account the excited bands, with their relative occupation resulting from the spin-changing dynamics, significantly enriches the Bose-Hubbard physics.

A number of interesting phases of matter have been predicted theoretically in the context of orbital quantum states in optical lattices. One of the core objectives is the theoretical prediction of conditions under which quantum states with excited Wannier states, in particular those with finite orbital angular momentum, can be realized on demand in the optical lattice. Here, mutual dipolar interactions appear to be very good candidates for yielding the controlled production of chosen quantum states in higher bands.

An important feature of dipole-dipole interactions in the optical lattice is their high selectivity—there are very clear selection rules which allow one to transfer angular momentum between certain, clearly defined spatial quantum states. These selection rules follow directly from the spatial symmetries of the system and energy conservation (Gawryluk *et al* 2007, Świślocki *et al* 2011a). The resonant character of the spin dynamics was recently observed in de Paz *et al* (2013a). In this experiment, the first band excitations correspond to frequencies of  $\omega/2\pi \approx 100$  kHz, which corresponds to energies significantly exceeding the dipole-dipole interaction energy  $E_D/\hbar = 0.1$  kHz. The spin dynamics is possible only at the expense of the Zeeman energy if an external magnetic field is applied. The external magnetic field becomes therefore a very important ‘knob’ triggering the dynamics and allowing one to select the final band excitation. A theoretical prediction of the resonant values of this external magnetic field in realistic experimental situations is quite difficult, because the spatial shape of the wavefunction is modified by the presence of contact interactions between atoms (Pietraszewicz *et al* 2013).

The resonant magnetic field is typically of the order of tens or hundreds of microgauss, making the observation of the Einstein-de Haas effect difficult at present. Since dipole-dipole interactions are very weak, the resonances are also very narrow. This means that experimental realization needs high precision. On the other hand, it guarantees that dipolar coupling is highly selective. By choosing an appropriate value of the magnetic field, one can tune the transition of atoms to a particular spatial state. Indeed, controlling dipolar interactions is the crucial point in working with dipolar systems. Such a control has been recently achieved in chromium condensates (Pasquiou *et al* 2010). It was shown that the external static magnetic field strongly influences the dipolar relaxation rate—there are a range of magnetic field intensities where this relaxation rate is strongly reduced, allowing for the accurate determination of the  $S = 6$  scattering length for chromium atoms. In Pasquiou *et al* (2011), a two-dimensional optical lattice and a static magnetic field are used to control the dipolar relaxation into higher lattice bands. In this work, evidence for the existence of the relaxation threshold with respect to the intensity of the magnetic field is shown. As the authors of Pasquiou *et al* (2011) claim, such an experimental setup might lead to the observation of the Einstein-de Haas effect. In the recent experiment of the same group (de Paz *et al* 2013a), the resonant demagnetization of chromium atoms in a 3D optical lattice was demonstrated.

In the following, we focus on a model system with on-site axial symmetry. The model discussed will show generic features of Bose–Hubbard systems with dipole–dipole interaction under conditions of free magnetization.

### 6.2. The many-body Hamiltonian

To describe interacting bosons of spin  $S$ , it is convenient to introduce the spinor field operator  $\hat{\psi}_m(\mathbf{r})$  annihilating particles in the state  $m_S$  ( $m_S = -S, \dots, S$ ). Then the many-body Hamiltonian can be divided into three parts:

$$\hat{H} = \hat{H}_0 + \hat{H}_C + \hat{H}_D. \quad (99)$$

The first part is the single-particle Hamiltonian and it has the following form:

$$\hat{H}_0 = \int d\mathbf{r} \sum_m \hat{\psi}_m^\dagger(\mathbf{r}) \left( \frac{\mathbf{p}^2}{2m} + V_{\text{ext}}(\mathbf{r}) - \gamma \mathbf{B} \cdot \mathbf{S} \right) \hat{\psi}_m(\mathbf{r}), \quad (100)$$

where, as before,  $m$  is the mass of the atom,  $\mathbf{S} = (S_x, S_y, S_z)$  is an algebraic vector composed of spin matrices in the appropriate representation, and  $\gamma$  is the gyromagnetic coefficient. We again take the external potential of the optical lattice  $V_{\text{ext}}$  in a quasi-two-dimensional arrangement (23). The last term in (100) is responsible for the linear Zeeman shift due to a uniform magnetic field  $\mathbf{B}$ . In what follows, we assume that the field is directed along the  $z$  axis and that it is weak enough for neglect of the quadratic Zeeman effect.

The short-range interactions of dipolar atoms are typically described by a pseudopotential. It can be written in a very general form (Ho 1998, Ohmi and Machida 1998, Santos and Pfau 2006):

$$\hat{H}_C = \frac{1}{2} \int d\mathbf{r} \sum_{s=0}^{2S} g_s \hat{\mathcal{P}}_s(\mathbf{r}), \quad (101)$$

where the  $\hat{\mathcal{P}}_s$  are projector operators, on different total spins, and  $g_s$  is the  $s$  wave scattering length for a total spin  $s$  and is given by  $g_s = 4\pi\hbar^2 a_s/M$ .

The long-range dipolar Hamiltonian can be written as

$$\hat{H}_D = \frac{\gamma^2}{2} \int d\mathbf{r} d\mathbf{r}' : \frac{\hat{h}_D(\mathbf{r}, \mathbf{r}')}{|\mathbf{r} - \mathbf{r}'|^3} :, \quad (102)$$

with the Hamiltonian density  $\hat{h}_D(\mathbf{r}, \mathbf{r}')$  (in the normal order as indicated by  $: \dots :$ ) of the form

$$\hat{h}_D(\mathbf{r}, \mathbf{r}') = \hat{\mathbf{F}}(\mathbf{r}) \cdot \hat{\mathbf{F}}(\mathbf{r}') - 3[\hat{\mathbf{F}}(\mathbf{r}) \cdot \mathbf{n}][\hat{\mathbf{F}}(\mathbf{r}') \cdot \mathbf{n}]. \quad (103)$$

Here,  $\hat{\mathbf{F}} = (\hat{F}_x, \hat{F}_y, \hat{F}_z)$  is an algebraic vector defined by  $\hat{\mathbf{F}}(\mathbf{r}) = \sum_{ij} \hat{\psi}_i^\dagger(\mathbf{r}) S_{ij} \hat{\psi}_j(\mathbf{r})$ , and  $\mathbf{n}$  is the unit vector in the direction of  $\mathbf{r} - \mathbf{r}'$ . Introducing ladder operators for the spin degree of freedom:

$$\hat{F}_\pm(\mathbf{r}) = \hat{F}_x(\mathbf{r}) \pm i\hat{F}_y(\mathbf{r}), \quad (104)$$

one can rewrite the density of the dipolar Hamiltonian as

$$\begin{aligned} \hat{h}_D(\mathbf{r}, \mathbf{r}') &= \frac{(1-3n_z^2)}{4} [4\hat{F}_z(\mathbf{r}')\hat{F}_z(\mathbf{r}) - \hat{F}_+(\mathbf{r}')\hat{F}_-(\mathbf{r}) - \hat{F}_-(\mathbf{r}')\hat{F}_+(\mathbf{r})] \\ &- \frac{3}{4}(n_x - in_y)^2 \hat{F}_+(\mathbf{r}')\hat{F}_+(\mathbf{r}) - \frac{3}{4}(n_x + in_y)^2 \hat{F}_-(\mathbf{r}')\hat{F}_-(\mathbf{r}) \\ &- \frac{3}{2}n_z(n_x - in_y)(\hat{F}_+(\mathbf{r}')\hat{F}_z(\mathbf{r}) + \hat{F}_z(\mathbf{r}')\hat{F}_+(\mathbf{r})) \\ &- \frac{3}{2}n_z(n_x + in_y)(\hat{F}_-(\mathbf{r}')\hat{F}_z(\mathbf{r}) + \hat{F}_z(\mathbf{r}')\hat{F}_-(\mathbf{r})). \end{aligned} \quad (105)$$

The form of (105) facilitates a physical interpretation of all terms. The first line represents dipolar interactions that do not lead to a change of the total magnetization of the field: the  $z$  components of the spin remain unchanged for both interacting atoms, or the  $z$  component of one atom decreases by 1 while the  $z$  component of the second atom increases by 1. The second line collects terms describing processes where both interacting atoms simultaneously flip the  $z$  axis projection of their spin: both by +1 or both by -1. Notice that the respective terms are multiplied by the phase factor  $(n_x \mp in_y)^2$ . This corresponds to a change of the projection of the orbital angular momentum for the atoms in their center of mass frame by -2 or 2 quanta. The last two lines describe processes in which the spin of one interacting atom is unchanged while the  $z$  axis component of the spin of the other atom changes by  $\pm 1$ . This spin-flipping term is multiplied by the phase factor  $n_z(n_x \mp in_y)$ , which signifies the change of the  $z$  projection of the relative orbital angular momentum of the interacting atoms by  $\mp 1$ . Evidently, the dipolar interactions conserve the  $z$  projection of the total angular momentum of the interacting atoms.

### 6.3. A two-component model system with a dynamical spin variable

The simplest model of the extended Bose–Hubbard system with a dynamical spin variable was discussed in Pietraszewicz *et al* (2012). In that model, realistic experimental parameters for chromium atoms of spin 3 confined in the 2D optical lattice were used. A significant simplification of the full many-body physics originates in choosing, at each lattice site  $(x_i, y_i)$ , only two basis wavefunctions  $\psi_a$  and  $\psi_b$  of the form

$$\begin{aligned} \psi_a(x, y, z) &= \mathcal{W}_0(x)\mathcal{W}_0(y)\mathcal{G}(z), \\ \psi_b(x, y, z) &= \frac{1}{\sqrt{2}} [\mathcal{W}_1(x)\mathcal{W}_0(y) + i\mathcal{W}_0(x)\mathcal{W}_1(y)] \mathcal{G}(z). \end{aligned} \quad (106)$$

The function  $\mathcal{G}(z) = \sqrt[4]{\Omega_z/\pi} \exp(-z^2\Omega_z/2)$  is the ground state wavefunction of the 1D harmonic oscillator in the  $z$  direction, and the functions  $\mathcal{W}_0(x)$  and  $\mathcal{W}_1(x)$  are the ground and the first excited Wannier states. In this way,  $\psi_a$  and  $\psi_b$  form a single-particle basis of the two-component system. This basis allows one to account for the resonant transfer of atoms between  $m_S = 3, l = 0$  and  $m_S = 2, l = 1$  states in the presence of a magnetic field aligned along the  $z$  axis. The lowest energy state  $\psi_a(x, y, z)$  is effectively coupled to the excited state with one quantum of orbital angular momentum  $\psi_b(x, y, z)$ . The state is a single-site analogue of a harmonic oscillator state  $\sim (x + iy) \exp[-(x^2 + y^2)/2 - z^2\omega_z/2]$ . The single-particle energies of the two basis states are denoted by  $E_a$  and  $E_b$  respectively.

The weakness of the dipolar interactions allows one to select the subspace of the two basis states. There are several channels of binary dipolar collisions leading to different excited Wannier states. However, one can choose the desired channel by means of a proper adjustment of the resonant external magnetic field, as shown in Świłocki *et al* (2011b). The energy difference between atoms in the ground and in the excited Wannier states is much larger than the dipolar energy, which is the smallest energy scale in the problem (except in the case of vanishing tunneling):  $E_{\text{dip}} = 10^{-4} E_r \ll E_b - E_a \sim E_r$ . However, at the resonant magnetic field  $B_0$ ,  $E_a - g\mu_B B_0 = E_b$ , the two energies are equal, and efficient spin transfer between the components appears on a typical time scale:  $\hbar/E_{\text{dip}} \simeq 10^{-2}$  s ( $\mu_B$  above is the Bohr magneton, while  $g$  is the Landé factor). The characteristic width of the resonances is small (Gawryluk *et al* 2011), of the order of  $E_{\text{dip}} \approx g\mu_B B$ , i.e.  $B \approx 100 \mu\text{G}$ .

Therefore, a two-component system is realized with the  $a$  component corresponding to atoms in the  $m_S = 3$  and  $l = 0$  state, while atoms in the  $b$  component have  $m_S = 2$  and  $l = 1$ . The single-site basis states are  $|n_a, n_b\rangle$ , where  $n_\alpha$  is the number of atoms in the  $\alpha$  component ( $\alpha = a, b$ ). The Hamiltonian of the system reads

$$\hat{H}_{\text{BH}} = \sum_i \left[ (E_a - g\mu_B B) \hat{a}_i^\dagger \hat{a}_i + E_b \hat{b}_i^\dagger \hat{b}_i + U_{ab} \hat{a}_i^\dagger \hat{b}_i^\dagger \hat{a}_i \hat{b}_i \right. \\ \left. + \frac{U_a}{2} \hat{a}_i^{\dagger 2} \hat{a}_i^2 + \frac{U_b}{2} \hat{b}_i^{\dagger 2} \hat{b}_i^2 + D(\hat{b}_i^{\dagger 2} \hat{a}_i^2 + \hat{a}_i^{\dagger 2} \hat{b}_i^2) \right] \\ - \sum_{\langle i,j \rangle} [t_a \hat{a}_i^\dagger \hat{a}_j + t_b \hat{b}_i^\dagger \hat{b}_j]. \quad (107)$$

The values of the parameters depend on the lattice height  $V_0$  and the confining frequency  $\Omega_z$ .  $U_a$ ,  $U_b$ ,  $U_{ab}$  are the contact interaction energies plus the part of the dipolar energy which has the same form as the corresponding contact term, and  $D$  is the on-site dipolar coupling of the two components, while  $t_a$  and  $t_b$  are tunneling energies (note that  $t_a > 0$  while  $t_b < 0$ ). This way, we arrive at a Hamiltonian that is an interesting modification of the standard Bose–Hubbard model.

Magnetic dipole–dipole interactions are very weak. Thus, in the above Hamiltonian the dipole–dipole interactions between atoms at neighboring sites are neglected. The on-site contact interactions  $U_a$ ,  $U_b$ , and  $U_{ab}$  cannot change the total spin (Pasquiou *et al* 2011, Kawaguchi and Ueda 2012), and the dipolar two-body interactions are much smaller than the contact ones. Therefore, one can keep only those dipolar terms that lead to spin dynamics. The structure of the Hamiltonian is general for a two-component system with two spin species coupled by the dipole–dipole interactions of atomic magnetic moments, and can easily be adopted to more realistic situations of lattice potentials that are not axially symmetric and anharmonic. The main modification will be in choosing different single-particle basis states.

However, two comments are in order.

- (a) The particular choice of the basis states was tailored to account for two-atom spin-flipping processes as selected through a proper adjustment of the magnetic field. Moreover, the chosen basis accounts for either two atoms

in the  $m_S = 3$  ground state or two atoms in the  $m_S = 2$  and  $p_x + ip_y$  orbital state with one quantum of orbital angular momentum. We neglected coupling of the ground state atoms to the state with one atom in the ground state with  $m_S = 2$  and the second in the  $m_S = 2$   $d$  band state with two quanta of orbital angular momentum. This approximation is justified if a small energy shift of  $p$  and  $d$  bands is taken into account while the on-site potential remains axially symmetric.

- (b) The two-atom orbital  $p_x + ip_y$  and  $m_S = 2$  state is coupled by the contact interaction to the state with one atom in  $p_x + ip_y$  with  $m_S = 1$  and the second in  $p_x + ip_y$  with  $m_S = 3$ . This coupling can be suppressed due to the energy conservation by a slight shift of the  $m_S = 2$  state for example.

Accounting for both of the above-mentioned processes would require choosing not two, but rather three or four single-particle basis states. This would lead to multi-component Bose–Hubbard systems.

#### 6.4. Novel ground state phases

To get a flavor of the physics described by the above model, one can limit the considerations to a small occupation of each lattice site with not more than one particle per single site on average. We assume a resonant magnetic field with  $E_a - g\mu_B B_0 = E_b$ . This requires adjusting the magnetic field in accordance with the lattice depth:  $B_0 = B_0(V_0)$ .

The dipolar interactions couple ground and excited Wannier states due to the tunneling in a higher order process even for a low density. The transfer between  $|1, 0\rangle$  and  $|0, 1\rangle$  states is realized as a sequence of adding an atom to the  $a$  component at a given single site  $|1, 0\rangle \rightarrow |2, 0\rangle$  via tunneling, followed by the dipolar transfer of both  $a$  species atoms to the excited Wannier state  $|2, 0\rangle \rightarrow |0, 2\rangle$ , and finally the tunneling that removes one  $b$  component atom from the site,  $|0, 2\rangle \rightarrow |0, 1\rangle$ . In this way, the two states are coupled provided that the tunneling is non-zero.

Thermodynamically stable phases of the system may be found following the standard mean-field approach of Fisher *et al* (1989). Assuming a translationally invariant ground state (since the Hamiltonian (107) enjoys that symmetry), and introducing superfluid order parameters for both components,  $\phi_{(a)} = \langle a_i \rangle$  and  $\phi_{(b)} = \langle b_i \rangle$ , as well as the chemical potential  $\mu$ , the mean-field Hamiltonian of the system is a sum of single-site Hamiltonians,  $\hat{H}_0 + \hat{H}_I$ , with

$$\hat{H}_0 = -\mu(\hat{a}^\dagger \hat{a} + \hat{b}^\dagger \hat{b}) + \frac{1}{2} U_a \hat{a}^\dagger \hat{a}^\dagger \hat{a} \hat{a} + \frac{1}{2} U_b \hat{b}^\dagger \hat{b}^\dagger \hat{b} \hat{b} \\ + U_{ab} \hat{a}^\dagger \hat{b}^\dagger \hat{a} \hat{b} + D(\hat{b}^\dagger \hat{b}^\dagger \hat{a} \hat{a} + \hat{a}^\dagger \hat{a}^\dagger \hat{b} \hat{b}), \quad (108)$$

$$\hat{H}_I = -zt_a \phi_{(a)}^* \hat{a} - zt_b \phi_{(b)}^* \hat{b} + \text{h.c.}, \quad (109)$$

with site indices omitted and  $z$  being the coordination number (for a 2D square lattice,  $z = 4$ ). The Hamiltonian  $\hat{H}_0 + \hat{H}_I$  does not conserve the number of particles: it describes a single site coupled to a particle reservoir. The order parameters  $\phi_{(a)}$  and  $\phi_{(b)}$  vanish in the MI phase and hopping of atoms vanishes.

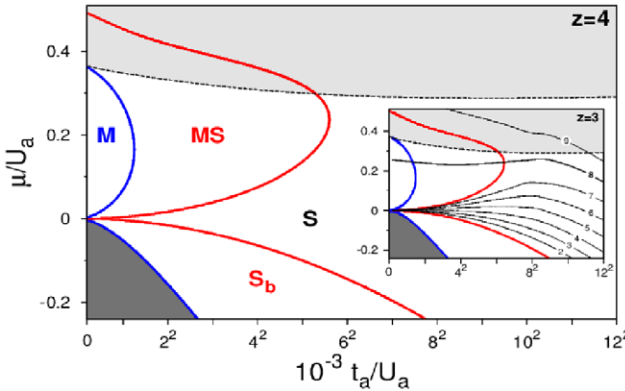


**Figure 29.** Phase diagram for a 2D square lattice at the resonance ( $z = 4$ ). The regions are: M—Mott insulator with one particle in an equal superposition of  $a$  and  $b$  states; MS—superfluid in  $a$  and  $b$  components ( $b$  dominated) and Mott insulator in the orthogonal superposition; S—superfluid phase of superposition of  $a$  and  $b$  components;  $S_b$ —superfluid in the  $b$  component. The inset shows the diagram for  $z = 3$ , together with the chemical potential  $\mu(N)$  for a given number of particles obtained from exact diagonalization. The lines, from bottom to top, correspond to occupation equal to  $N = 2, \dots, 9$ , as indicated. For  $\mu > U_b$  (the light gray region), the ground state of the system is a two-particle state. Therefore, in this regime the phases shown are thermodynamically unstable. They are stable, however, with respect to one-particle hopping. This figure is from Pietraszewicz *et al* (2012).

Close to the boundary, on the SF side,  $\phi_{(a)}$  and  $\phi_{(b)}$  can be treated as small parameters in the perturbation theory.

The single-site ground state becomes unstable if the mean field  $\phi_{(a)}$  or  $\phi_{(b)}$  is different from zero. The self-consistency condition

$$\phi_{(c)} = \lim_{\beta \rightarrow \infty} \text{Tr} [\hat{c} e^{-\beta(H_0+H_l)}] / Z(\beta), \quad (110)$$

where  $c = a, b$ , allows one to find the mean fields numerically. In the lowest order, the set of equation (110) becomes linear and homogeneous. Thus, non-zero solutions for  $\phi_{(c)}$  are obtained from the necessary condition of a vanishing determinant of (110). This yields the lobes shown in figure 29.

In the limit  $\beta \rightarrow \infty$ , the partition function reduces to the single contribution of the lowest energy state,  $Z(\beta) = e^{-\beta E_0}$ . For  $\mu < U_b < U_a$ , the sole contribution to equation (110) comes from eigenstates of the Hamiltonian with zero, one, and two particles.

The single-site ground state is the  $|0, 0\rangle$  vacuum state (the dark gray region in figure 29) for  $\mu < 0$  and small tunnelings. With increasing tunneling (and fixed  $\mu$ ), particles appear in the superfluid vortex  $b$  phase (labeled as  $S_b$  in figure 29). Only at larger tunnelings do some atoms appear in the  $a$  component, and both ‘standard’ and  $p_x + ip_y$  orbital superfluids coexist ( $S$ ).

The situation becomes richer for  $0 < \mu < U_b$ . At the resonance,  $B = B_0$ , the ground state is degenerate if tunnelings are neglected: the states  $|1, 0\rangle$  and  $|0, 1\rangle$  have the same energy:  $E_0 = -\mu$ . This degeneracy is lifted for non-zero tunnelings. Additionally, the position of the resonance is shifted then towards smaller magnetic fields. The effective Hamiltonian in the resonant region possesses a single-site ground state that is a superposition of the two components:  $|g\rangle = \alpha_1 |1, 0\rangle - \alpha_2$

$|0, 1\rangle$ . While crossing the resonance, the ground state switches from  $|1, 0\rangle$  to  $|0, 1\rangle$ . Exactly at resonance,  $\alpha_1 = \alpha_2 = 1/\sqrt{2}$ . A perturbative analysis allows one to estimate the width of the resonance  $\Delta B$  to be  $g\mu_B |\Delta B| \approx 10^{-6} E_r$  for  $V_0 = 25 E_r$ . For a shallower lattice,  $V_0 = 10 E_r$ , the resonant region is broader:  $g\mu_B |\Delta B| \approx 10^{-3} E_r$ . Unfortunately, due to its small width, the resonance can be hardly accessible, particularly for small tunnelings. Away from the resonance, the standard phase diagrams for the  $a$  and  $b$  components emerge.

In figure 29, we show regions of stability of the different possible phases of the system at resonance, i.e. when  $|g\rangle = (|1, 0\rangle - |0, 1\rangle)/\sqrt{2}$ . The system is in the Mott insulating phase (M) with one atom per site for small tunnelings. Still, every atom is in a superposition of the ground and the vortex Wannier states. At the border of the Mott lobe (blue line), equation (110) allows for non-zero solutions for  $\phi_{(a)}$  and  $\phi_{(b)}$ . Expressing  $\hat{H}_l$  in terms of the composite bosonic operators  $\hat{A}^\dagger = (\kappa_a \hat{a}^\dagger + \kappa_b \hat{b}^\dagger)$  and  $\hat{B}^\dagger = (-\kappa_b \hat{a}^\dagger + \kappa_a \hat{b}^\dagger)$ , where  $\kappa_a^2 + \kappa_b^2 = 1$ , allows one to diagonalize  $\hat{H}_l$ , with the coefficients  $\kappa_i$  depending on the tunnelings  $t_a$  and  $t_b$ . These composite operators create an atom in two orthogonal superpositions of  $a$  and  $b$  states. At the border of the Mott phase, the mean value of the operator  $\hat{B}$  is different from zero, and a non-vanishing superfluid component,  $\Psi_B = -\kappa_b \phi_{(a)} + \kappa_a \phi_{(b)}$ , appears in the MS region. The ratio  $(\kappa_b/\kappa_a)^2 \approx 0.02$  is small at the edge of stability of the Mott insulator. Therefore,  $\hat{B}^\dagger \approx \hat{b}^\dagger$ , i.e. the superfluid  $\Psi_B$  is dominated by the orbital  $b$  component. On the other hand, in the region discussed the mean field corresponding to the  $\hat{A}^\dagger \approx \hat{a}^\dagger$  operator vanishes. The system is therefore in an equal superposition of the Mott insulating and superfluid phases. The Mott phase is dominated by the  $a$  component and the superfluid phase consists mainly of the  $b$  particles. Both components, however, contain a small minority of the remaining species.

The system undergoes yet another phase transition for larger tunnelings, as equation (110) allows for another non-zero mean field. At this transition, the departure of the mean value of  $\hat{A}$  from zero defines the border of the ‘bigger’ lobe, and the Mott component of the ground Wannier state becomes unstable. The additional mean field  $\Psi_A = \kappa_a \phi_{(a)} + \kappa_b \phi_{(b)}$  appears in the (S) region. As before,  $(\kappa_b/\kappa_a)^2 \approx 0.06$  is small. The  $a$  species dominates the  $\Psi_A$  superfluid component. Both  $\Psi_A$  and  $\Psi_B$  superfluids exist in the (S) region.

Qualitative support for the above mean-field findings is obtained from a direct inspection of the true many-body ground state, obtained by exact diagonalization of the many-body Hamiltonian in a small  $2 \times 4$  rectangular plaquette with periodic boundary conditions for total number of particles  $N = 1, \dots, 10$ . For such a small system, each site has three neighbors, i.e.  $z = 3$ , and the resonance condition is obtained by finding the magnetic field for which the  $a$  and  $b$  species are *equally populated*. In the inset of figure 29, the exact results are compared with the mean-field results for  $z = 3$ . The lines correspond to the constant number of particles per site obtained from the relation  $\mu(N) = [E_0(N+1) - E_0(N-1)]/2$ . In that way, one may trace the phases that the system enters while adiabatically changing the tunneling at fixed particle

number. The M and MS phases can be reached with one particle per site only (eight particles in the plaquette).

It is also worthwhile to consider the hopping averages, defined as the mean values of the following hopping operators:  $h_a = \sum_{\langle j \rangle} \langle \hat{a}_j^\dagger \hat{a}_i \rangle$  and  $h_b = \sum_{\langle j \rangle} \langle \hat{b}_j^\dagger \hat{b}_i \rangle$ . They annihilate a particle at a given site and put it in a neighboring site, and may be thought of as the number-conserving analogues of the mean fields  $\phi_{(a)}$  and  $\phi_{(b)}$ , which in exact diagonalizations without symmetry-breaking terms always vanish. In figure 30, the hoppings for the case of one particle per site are shown. For large tunnelings, both  $a$  and  $b$  hoppings are large—the components are in the superfluid phase. On entering the MS phase at  $t_a/U_a \simeq 0.064$ , the hopping of the  $a$  component rapidly decreases while the hopping of the  $b$  phase remains large—the system enters a Mott insulator form dominated by the  $a$  component superimposed with a superfluid form dominated by the  $b$  component. At  $t_a/U_a \simeq 0.002$ , both hoppings tend to zero—the system enters the Mott phase with equal occupation of the two species. These results confirm the findings based on the mean-field approach.

The effective two-state model studied exhibits a number of exotic phases. One might think that the model Hamiltonian crucially depends on the assumed axial symmetry and harmonicity of a single lattice site, which is justified in deep lattices only (Collin *et al* 2010, Martikainen 2011, Pietraszewicz *et al* 2013). Including an anharmonic correction requires some modification, but the structure of the system Hamiltonian remains the same in many cases. In a potential that is anharmonic and not axially symmetric, the vortex-like final state is no longer an eigenstate of the Hamiltonian. Anharmonicity and anisotropy combined with contact interactions lead to a fine structure of two-body energies in the lattice site. The vortex state is split into three two-particle states which can be *separately* addressed through an appropriate choice of the magnetic field. Therefore, a two-state structure of the Hamiltonian becomes generic for the systems studied. The model discussed here describes the whole class of two-state systems with dipole–dipole interactions and free magnetization, under the resonance condition of equal energies of the two coupled states.

## 7. 1D and 2D models of the Salerno type: the mean-field and quantum versions

### 7.1. Introduction

A natural part of the analysis of Bose–Hubbard models is the consideration of their mean-field limit, which corresponds to classical lattice models described by discrete nonlinear Schrödinger (DNLS) equations (see, e.g. the recent works Mishmash and Carr 2009, Barbiero and Salasnich 2014 and references therein). In particular, Mishmash and Carr (2009) highlighted the correspondence between the two descriptions of a system of ultracold bosons in a one-dimensional optical lattice potential: (1) using the discrete nonlinear Schrödinger equation, a discrete mean-field theory approach, and (2) using the Bose–Hubbard Hamiltonian, a discrete quantum-field

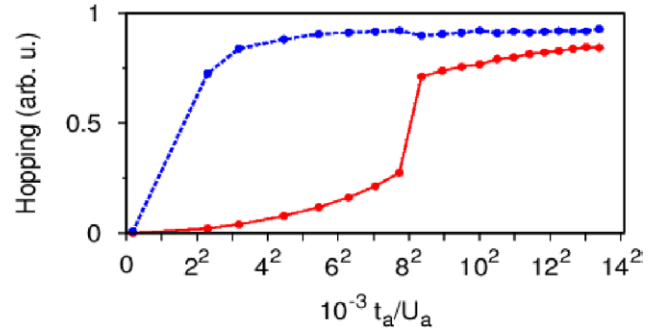


**Figure 30.** Hopping for the lowest energy state in a  $2 \times 4$  plaquette obtained from exact diagonalization. Upper line— $b$  component; lower line— $a$  component. This figure is from Pietraszewicz *et al* (2012).

theory approach. This discussion includes, in particular, the formation of solitons.

In this vein, the mean-field limit of the non-standard Bose–Hubbard models, whose characteristic feature is a nonlinear coupling between adjacent sites of the underlying lattice, is represented by classical lattice models featuring a similar nonlinear interaction between nearest-neighbor sites. They form a class of systems known as *Salerno models* (SMs). In the one-dimensional (1D) form, the SM was first introduced by Mario Salerno in 1992 (Salerno 1992) as a combination of the integrable *Ablowitz–Ladik* (AL) system (Ablowitz and Ladik 1976) and the non-integrable DNLS equation. The former system is a remarkable mathematical model, but it does not have straightforward physical implementations, while the DNLS equations find a large number of realizations, especially in nonlinear optics and Bose–Einstein condensates (see section 2.1). For this reason, the DNLS equation has been a subject of numerous analytical, numerical, and experimental studies, many of which were summarized in the book (Kevrekidis 2009). The objective of the present section is to introduce the mean-field (classical) and quantum versions of the SM in one and two dimensions (in fact, the quantum version is considered only in 1D), and survey results obtained for localized modes (discrete solitons) in the framework of 1D and 2D realizations of the mean-field version. An essential peculiarity of the SM is the non-standard form of the Poisson bracket in its classical form, and, accordingly, the specific form of the commutation relations in its quantum version. These features are, as a matter of fact, another manifestation of the non-standard character of Hubbard models with nonlinear coupling between adjacent sites.

### 7.2. One-dimensional Salerno models and discrete solitons

**7.2.1. The formulation of the model.** It is well known that, while the straightforward discretization of the 1D nonlinear Schrödinger equation is non-integrable, there is a special form of the discretization, namely, the AL model, which retains the integrability, and admits generic exact solutions for standing and moving solitons, as well as exact solutions for collisions between them (Ablowitz and Ladik 1976). Unlike the exceptional case of the analytically solvable AL model, discrete

solitons in non-integrable systems are looked for in a numerical form, or (sometimes) by means of the variational approximation (Papacharalampous *et al* 2003, Malomed *et al* 2012). Nevertheless, there are some specially devised 1D non-integrable models for which *particular* exact soliton solutions can be found, too (Kevrekidis 2003, Malomed *et al* 2006, Oxtoby and Barashenkov 2007).

As the DNLS and AL equations differ in the type of the nonlinear terms (on-site or intersite ones), and converge to a common continuum limit in the form of the ordinary integrable nonlinear Schrödinger equation, a combined discrete model may be naturally introduced, mixing the cubic terms of both types. Known as the SM (Salerno 1992), the 1D version of this combined system is based on the following discrete equation:

$$i\frac{d}{dt}\Phi_n = -(\Phi_{n+1} + \Phi_{n-1})(1 + \mu|\Phi_n|^2) - 2\nu|\Phi_n|^2\Phi_n, \quad (111)$$

where  $\Phi_n$  is the complex classical field variable at the  $n$ th site of the lattice, while real coefficients  $\mu$  and  $\nu$  account for the nonlinearities of the AL and DNLS types, respectively. The celebrated integrable AL equation proper corresponds to  $\nu = 0$ :

$$i\frac{d}{dt}\Phi_n = -(\Phi_{n+1} + \Phi_{n-1})(1 + \mu|\Phi_n|^2). \quad (112)$$

In equation (111) with  $\nu \neq 0$ , negative  $\nu$  can be made positive by means of the *staggering transformation*,  $\Phi_n \equiv (-1)^n \tilde{\Phi}_n^*$  (the asterisk stands for the complex conjugation), and then one may fix  $\nu \equiv +1$ , by way of a rescaling:  $\tilde{\Phi}_n \equiv \Phi_n / \sqrt{|\nu|}$ . Therefore, a natural choice is to fix  $\nu \equiv +1$ , unless one wants to consider the AL model per se, with  $\nu = 0$ . In contrast to that, the sign of the coefficient  $\mu$ , which characterizes the relative strength of the nonlinear AL coupling between the nearest neighbors, *cannot* be altered. In particular, the AL model with  $\nu = 0$  and  $\mu < 0$  has no (bright) soliton solutions.

The SM equation (111), as well as its AL counterpart (112), conserve the total norm, differing from the ‘naive’ expression relevant in the case of the DNLS equation:

$$\mathcal{N}_{\text{DNLS}} = \sum_n |\Phi_n|^2. \quad (113)$$

For both equations (111) and (112), the conserved norm is (Ablowitz and Ladik 1976, Cai *et al* 1996, Rasmussen *et al* 1997)

$$\mathcal{N} = \frac{1}{\mu} \sum_n \ln(|1 + \mu|\Phi_n|^2|). \quad (114)$$

Note that expression (114) does not depend on  $\nu$ . Therefore, it is identical for the SM and AL models, carrying over into the simple expression (113) in the limit of  $\mu \rightarrow 0$ .

The other dynamical invariant of equation (111), in addition to the norm, is its Hamiltonian, that, like the norm, has a somewhat tricky form (Cai *et al* 1996, Rasmussen *et al* 1997) (which has its consequences for the identification of the symplectic structure of the SM and its quantization, see below):

$$\mathcal{H} = - \sum_n \left[ (\Phi_n \Phi_{n+1}^* + \Phi_{n+1} \Phi_n^*) + \frac{2}{\mu} |\Phi_n|^2 \right] + \frac{2}{\mu} \mathcal{N}, \quad (115)$$

where the above normalization,  $\nu = +1$ , is adopted. In the limiting case of the DNLS equation,  $\mu \rightarrow 0$ , the expansion of Hamiltonian (115) in powers of  $\mu$  yields the usual expression for the DNLS equation:

$$\mathcal{H}_{\text{DNLS}} = - \sum_n \left[ (\Phi_n \Phi_{n+1}^* + \Phi_{n+1} \Phi_n^*) + |\Phi_n|^4 \right]. \quad (116)$$

The Hamiltonian of the AL proper can be obtained from the general expression (115) by taking the limit  $\mu \rightarrow \infty$ , which produces a simple expression (Ablowitz and Ladik 1976):

$$\mathcal{H}_{\text{AL}} = - \sum_n (\Phi_n \Phi_{n+1}^* + \Phi_{n+1} \Phi_n^*). \quad (117)$$

**7.2.2. Solitons** The AL equation (112) gives rise to exact solutions for (bright) solitons in the case of self-focusing nonlinearity,  $\mu > 0$ . Then, one may set  $\mu \equiv +1$  by means of the obvious rescaling, and the exact soliton solutions take the following form:

$$\Phi_n(t) = (\sinh \beta) \operatorname{sech} [\beta(n - \xi(t))] \exp [i\alpha(n - \xi(t)) - i\varphi(t)], \quad (118)$$

where  $\beta$  and  $\alpha$  are arbitrary real parameters that determine the soliton’s amplitude,  $A \equiv \sinh \beta$ , its velocity,  $V$ , and its intrinsic frequency,  $\Omega$ :

$$V \equiv \frac{d\xi}{dt} = \frac{2 \sinh \beta}{\beta} \sin \alpha, \\ \Omega \equiv \frac{d\varphi}{dt} = -2 \left[ (\cos \alpha) \cosh \beta + \alpha \sin \alpha \frac{\sinh \beta}{\beta} \right]. \quad (119)$$

The SM with  $\nu = +1$  (as fixed above) and  $\mu > 0$ , i.e. with *non-competing* on-site and intersite self-focusing nonlinearities, was studied in a number of works; see Cai *et al* (1996), (1997), Dmitriev *et al* (2003) and Rasmussen *et al* (1997) and references therein. It has been demonstrated that equation (111) gives rise to static and, sometimes, moving (Cai *et al* 1997) solitons at all positive values of  $\mu$ . In particular, one non-trivial problem is the mobility of the discrete solitons in the DNLS limit, which corresponds to  $\mu = 0$  (Ablowitz *et al* 2002, Papacharalampous *et al* 2003).

The SM based on equation (111) with  $\mu < 0$  features *competing nonlinearities*, the terms corresponding to  $\nu = +1$  and  $\mu < 0$  representing the self-focusing and defocusing cubic interactions, respectively. In the 1D setting, the SM with  $\mu < 0$  was introduced in Gomez-Gardeñes *et al* (2006b). In that work, it was demonstrated that this version of the SM gives rise to families of quiescent discrete solitons, which are looked for as

$$\Phi_n(t) = e^{-i\omega t} U_n, \quad (120)$$

with negative frequency  $\omega$  and real amplitudes  $U_n$  (unlike the complex solutions for moving solitons (118) in the AL model), of two different types. One family represents ordinary discrete solitons, which are similar to quiescent solitons in the SM with

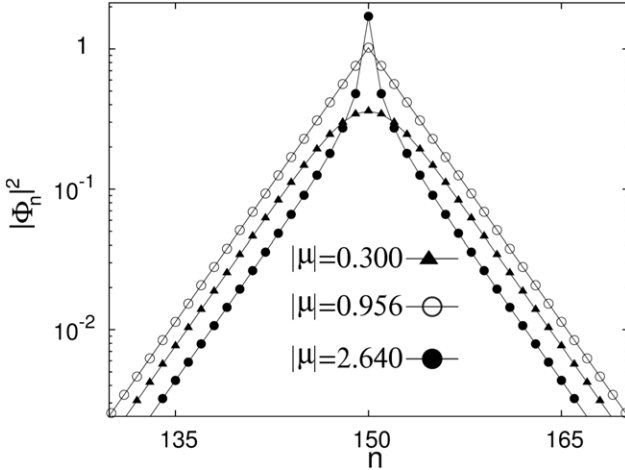


**Figure 31.** Examples of three different kinds of discrete solitons, shown on the logarithmic scale at  $\omega = -2.091$ , in the one-dimensional Salerno model (111) with competing nonlinearities: an ordinary (smooth) soliton at  $\mu = -0.3$ , a peakon at  $\mu = -0.956$ , and a cuspon at  $\mu = -2.64$ . This figure is from Gomez-Gardeñes *et al* (2006b).

$\mu \geq 0$ , where  $\mu = 0$  corresponds to the DNLS equation, while the other family represents *cuspons*, that are characterized by a higher curvature of their profile at the center than in the exponentially decaying tails; see typical examples in figure 31. At the border between the ordinary solitons and the cuspons, a special discrete soliton appears, in the form of a *peakon*, which is also shown in figure 31. In the continuum limit of equation (111) (Gomez-Gardeñes *et al* 2006b) with  $\mu < 0$  (see below), a peakon solution is available in an exact analytical form (130), while cuspons do not exist in that limit. The stability of the discrete solitons in the SM with the competing nonlinearities was also investigated in Gomez-Gardeñes *et al* (2006b), with the conclusion that only a small subfamily of the ordinary solitons is unstable, while all cuspons, including the peakon, are stable.

For fixed  $\mu = -0.884$ , the soliton families are illustrated in figure 32, which shows the norm (114) as a function of  $|\omega|$ . The plot clearly demonstrates that the ordinary solitons and cuspons are separated by the peakon. Except for the part of the family of ordinary solitons with the negative slope,  $dN/d(|\omega|) < 0$ , which is marked in figure 32, the solitons are stable. In particular, the peakon and the cuspons are completely stable modes. The instability of the portion of the family of ordinary solitons with  $dN/d(|\omega|) < 0$  agrees with the prediction from the Vakhitov–Kolokolov (VK) criterion, which gives a necessary stability condition in the form of  $dN/d\omega < 0$ . The VK criterion applies to the ordinary solitons, but is irrelevant for the cuspons.

**7.2.3. Bound states of the discrete solitons and their stability.** Spatially symmetric (even) and antisymmetric (odd) states of discrete solitons were also constructed in the framework of equation (111); see examples of bound peakons in figure 33. It is known that antisymmetric bound states of discrete solitons in the DNLS equation are stable, while the symmetric ones are not (Kapitula *et al* 2001, Pelinovsky *et al* 2005). The same is true for bound states of ordinary discrete solitons

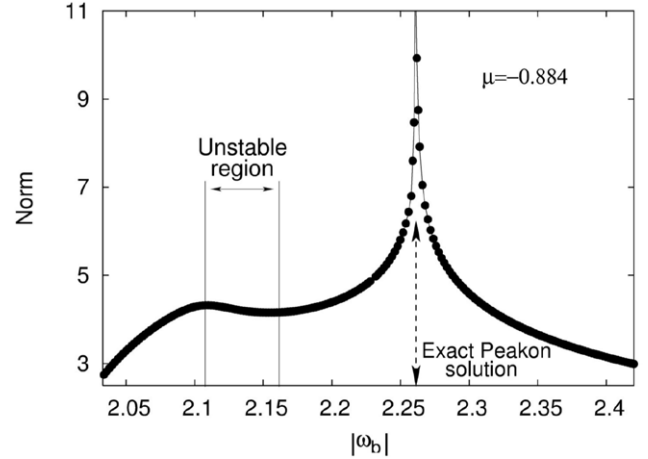


**Figure 32.** The norm of the discrete quiescent solitons, in the Salerno model with competing nonlinearities, versus the frequency (here the frequency is denoted as  $\omega_b$ , instead of  $\omega$ ), for  $\mu = -0.884$ . This figure is from Gomez-Gardeñes *et al* (2006b).

in the SM. However, the situation is *exactly opposite* for the cuspons: their symmetric bound states are stable, while the antisymmetric ones are unstable.

### 7.3. The two-dimensional Salerno model and discrete solitons

The 2D version of the SM was introduced in Gomez-Gardeñes *et al* (2006a). It is based on the following equation (cf equation (111)):

$$i \frac{d}{dt} \Phi_{n,m} = - \left[ (\Phi_{n+1,m} + \Phi_{n-1,m}) + C(\Phi_{n,m+1} + \Phi_{n,m-1}) \right] \\ \times \left( 1 + \mu |\Phi_{n,m}|^2 \right) - 2 |\Phi_{n,m}|^2 \Phi_{n,m}, \quad (121)$$

where the same normalization as above,  $\nu = +1$ , is imposed. In this notation,  $C$  accounts for a possible anisotropy of the 2D lattice ( $C = 1$  and  $C = 0$  correspond, respectively, to the isotropic 2D lattice and its 1D counterpart; see equation (111)). Accordingly, the variation of  $C$  from 0 to 1 opens the way for considering the *dimensionality crossover* from 1D to 2D.

Similarly to the 1D version of the SM, equation (121) conserves the norm and Hamiltonian (see equations (114) and (115)):

$$\mathcal{N}_{2D} = \frac{1}{\mu} \sum_{m,n} \ln \left( \left| 1 + \mu |\Phi_{n,m}|^2 \right| \right), \quad (122)$$

$$\mathcal{H}_{2D} = - \sum_{n,m} \left[ (\Phi_{n,m} \Phi_{n+1,m}^* + \Phi_{n+1,m} \Phi_{n,m}^*) \right. \\ \left. C (\Phi_{n,m} \Phi_{n,m+1}^* + \Phi_{n,m+1} \Phi_{n,m}^*) + \frac{2}{\mu} |\Phi_{n,m}|^2 \right] + \frac{2}{\mu} \mathcal{N}_{2D}. \quad (123)$$

Fundamental 2D solitons are looked for in the same form as their 1D counterparts (120):

$$\Phi_{mn}(t) = e^{-i\omega t} U_{mn}. \quad (124)$$

In the most interesting case of the competing nonlinearities,  $\mu < 0$ , the general properties of the solitons are similar to those

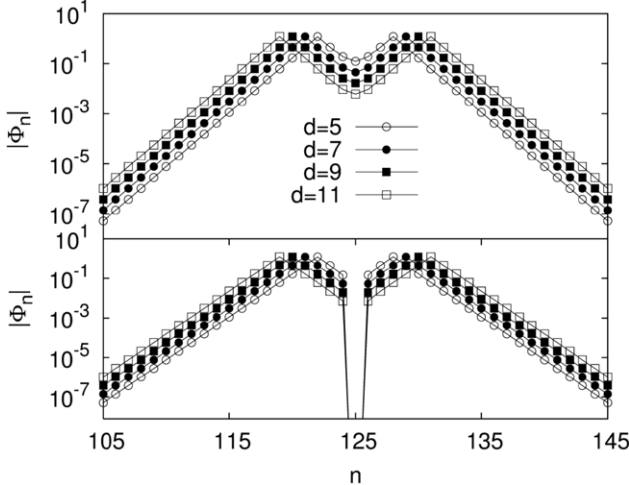


**Figure 33.** Profiles of typical symmetric (top) and antisymmetric (bottom) bound states of two peakons are shown, on a logarithmic scale, for  $\omega = -3.086$  and  $\mu = -0.645$ . This figure is from Gomez-Gardeñes *et al* (2006b).

outlined above in the framework of the 1D version of the SM. There are ordinary solitons, which have regions of stability and instability (the stability border depends on  $C$ ), and cuspons, which are entirely stable. Examples of 2D solitons of both types are displayed in figure 34. The families of ordinary solitons and cuspons are separated by 2D peakons, which are stable, too. Spatially antisymmetric bound states of the 2D ordinary solitons and symmetric bound states of the 2D cuspons are stable, while the bound states with the opposite parities are unstable—this is also similar to the situation for the 1D model.

In addition to the fundamental solitons, the 2D model with the competing nonlinearities supports solitary vortices, of two different types: on-site-centered and off-site-centered ones (also called ‘rhombuses’ and ‘squares’), which have narrow stability regions (the stability was investigated in Gomez-Gardeñes *et al* (2006a) only for vortex solitons with topological charge 1). Examples of the vortices are displayed in figure 35. In the two-dimensional SM with non-competing nonlinearities, unstable vortices turn into fundamental solitons, losing their vorticity (obviously, the angular momentum is not conserved in the lattice system). However, in the SM with the competing nonlinearities, unstable stationary vortices transform into *vortical breathers*, which are persistent oscillating localized modes that keep their vorticity.

#### 7.4. The continuum limit of the 1D and 2D Salerno models

**7.4.1. One dimension.** The continuum limit of the discrete equation (111) deserves separate consideration. This limit was introduced in Gomez-Gardeñes *et al* (2006b) by defining  $\Phi(x, t) \equiv e^{2it}\Psi(x, t)$ , and using the truncated Taylor expansion,  $\Psi_{n \pm 1} \approx \Psi \pm \Psi_x + (1/2)\Psi_{xx}$ , where  $\Psi$  is here treated as a function of the continuous coordinate  $x$ , which coincides with  $n$  when it takes integer values. Then, the continuum counterpart of equation (111) is

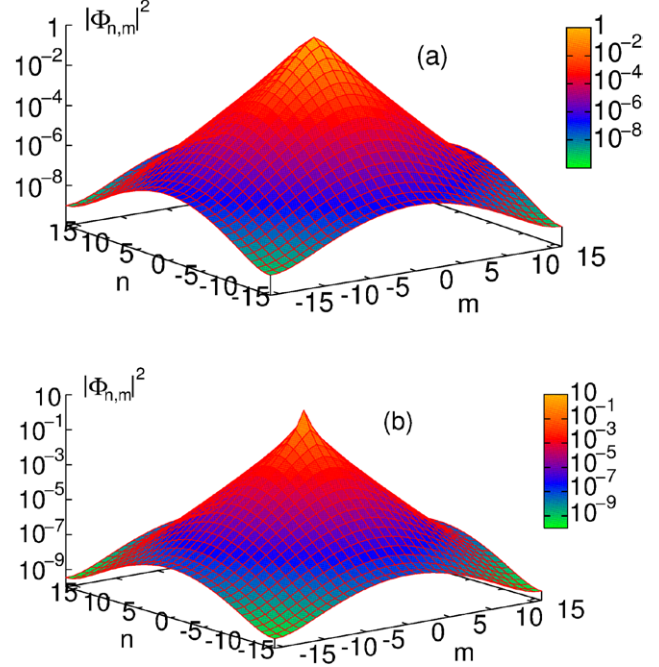


**Figure 34.** Profiles of discrete solitons in the isotropic ( $C = 1$ ) 2D Salerno model with competing nonlinearities, found for frequency  $\omega = -4.22$ : (a) a regular soliton at  $\mu = -0.2$ ; (b) a cusp at  $\mu = -0.88$ . This figure is from Gomez-Gardeñes *et al* (2006a).

$$i\Psi_t = -2(1-|\mu|)|\Psi|^2\Psi - (1-|\mu||\Psi|^2)\Psi_{xx}, \quad (125)$$

where one sets  $\nu = +1$  and  $\mu < 0$  as above (i.e. the system with competing nonlinearities is considered). Equation (125) conserves the norm and Hamiltonian, which can be derived as the continuum limit of expressions (114) and (115):

$$\mathcal{N}_{\text{cont}} = \frac{1}{\mu} \int_{-\infty}^{+\infty} dx \ln (|1-|\mu||\Psi|^2|), \quad (126)$$

$$\mathcal{H}_{\text{cont}} = \int_{-\infty}^{+\infty} dx \left[ |\Psi_x|^2 + 2\left(\frac{1}{|\mu|} - 1\right)|\Psi|^2 \right] + \frac{2}{\mu} \mathcal{N}_{\text{cont}}. \quad (127)$$

Soliton solutions to equation (125) can be looked for as  $\Psi = e^{-i\omega t}U(x)$ , with the real function  $U$  obeying the equation

$$\frac{d^2U}{dx^2} = -\frac{\omega + 2(1-|\mu|)U^2}{1-|\mu|U^2}U, \quad (128)$$

which may give rise to solitons, provided that  $|\mu| < 1$ . The absence of solitons at  $|\mu| > 1$  implies that (bright) solitons do not exist in the continuum limit if the continual counterpart of the self-defocusing intersite nonlinearity is stronger than the on-site self-focusing nonlinearity. For  $|\mu| < 1$ , the solitons exist in the following frequency band:

$$0 < -\omega < (1/|\mu|) - 1. \quad (129)$$

Solitons can be found in an explicit form near edges of the band (129). At small  $|\omega|$ , an approximate soliton solution is  $U(x) \approx \sqrt{|\omega|/(1-|\mu|)} \operatorname{sech}(\sqrt{2|\omega|}x)$ , while precisely at the opposite edge of the band, at  $-\omega = 1/|\mu| - 1$ , i.e. an exact

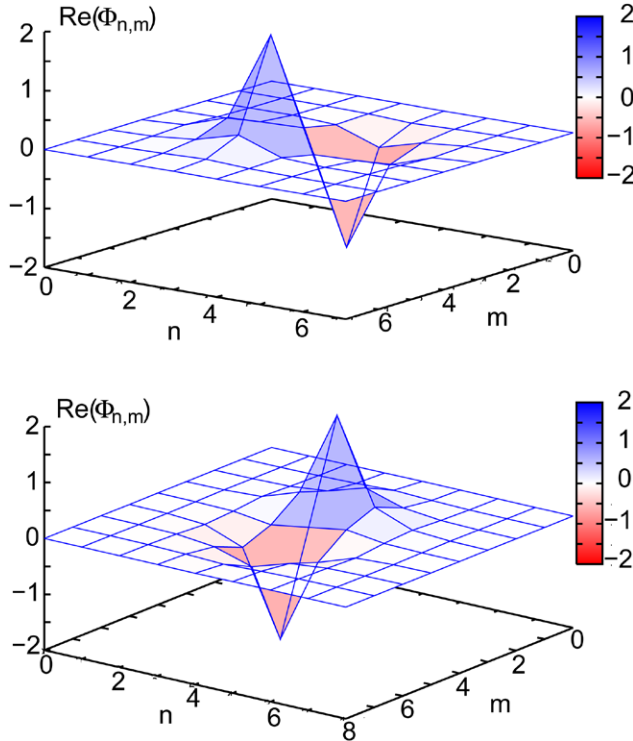


**Figure 35.** Examples of stable discrete vortices with topological charge 1 in the 2D Salerno model with competing nonlinearities. Profiles of the real part of the ‘vortex square’ and ‘vortex rhombus’ modes are shown in the top and bottom panels, respectively. Both solutions are found for  $\mu = -0.4$  and  $\omega = -7.0$ . This figure is from Gomez-Gardeñes *et al* (2006a).

solution is available, in the form of a *peakon* (this time, in the continuum model):

$$U_{\text{peakon}} = \left(1/\sqrt{|\mu|}\right) \exp\left(-\sqrt{(1/|\mu|)-1}|x|\right). \quad (130)$$

The term ‘peakon’ implies that solution (130) features a jump of the derivative at the central point. The norm (126) of the peakon is  $\pi^2/\left[6\sqrt{|\mu|}(1-|\mu|)\right]$ , and its energy is finite, too.

**7.4.2. Two dimensions.** The continuum limit of equation (121) may be defined by proceeding from discrete coordinates,  $(n, m)$ , to continuous ones,  $(x, y) \equiv (n/\sqrt{\alpha}, m/\sqrt{C\alpha})$ , and defining  $\Phi_{n,m} \equiv \Psi(x, y)\exp(2(1+C)it)$ :

$$i\Psi_t + (1+\mu|\Psi|^2)(\Psi_{xx} + \Psi_{yy}) + 2[(1+C)\mu + 1]|\Psi|^2\Psi = 0; \quad (131)$$

see equation (125). Note that this equation always has the isotropic form. The dispersive nonlinear term in equation (131),  $\mu|\Psi|^2(\Psi_{xx} + \Psi_{yy})$ , prevents the collapse, for both positive and negative  $\mu$ . Therefore, the *quasi-collapse*, which is known in other discrete systems (Laedke *et al* 1994), is not expected in the two-dimensional discrete SM either.

### 7.5. The Hamiltonian structure of the 1D model, and its quantization

**7.5.1. The classical version.** The specific form of Hamiltonian (115) of the SM makes the Poisson brackets in this system

different from the standard form (Cai *et al* 1996, Rasmussen *et al* 1997). Namely, for a pair of arbitrary functions of the discrete field variables,  $B(\Phi_n, \Phi_n^*)$ ,  $C(\Phi_n, \Phi_n^*)$ , the Poisson brackets are written as

$$\{B, C\} = i \sum_n \left( \frac{\partial B}{\partial \Phi_n} \frac{\partial C}{\partial \Phi_n^*} - \frac{\partial B}{\partial \Phi_n^*} \frac{\partial C}{\partial \Phi_n} \right) (1 + \mu |\Phi_n|^2), \quad (132)$$

the last factor being the non-standard feature. In particular, the brackets of the variables  $\Phi_n$  and  $\Phi_n^*$  themselves are

$$\begin{aligned} \{\Phi_n, \Phi_m^*\} &= i(1 + \mu |\Phi_n|^2) \delta_{nm}, \\ \{\Phi_n, \Phi_m\} &= \{\Phi_n^*, \Phi_m^*\} = 0. \end{aligned} \quad (133)$$

One can attempt to define, instead of the dynamical variables  $\Phi_n$ , another set:

$$\chi_n \equiv f(|\Phi_n|^2) \Phi_n, \quad (134)$$

such that they will obey the usual commutation relations:

$$\{\chi_n, \chi_m^*\} = i\delta_{mn}, \{\chi_n, \chi_m\} = 0, \quad (135)$$

instead of the ‘exotic’ ones (133). Substituting ansatz (134) into equation (135), and making use of definition (132), one arrives at the following equation for the function  $f(x)$ , which ensures that the Poisson brackets for the new variables take the standard form of equation (135):

$$2xf \frac{df}{dx} + f^2 = \frac{1}{1 + \mu x}. \quad (136)$$

One solution of equation (136) is  $f(x) = \sqrt{|\ln(1 + \mu x)|/(\mu x)}$ . Thus, the new set of canonical variables (134) is

$$\chi_n = \sqrt{\frac{|\ln(1 + \mu |\Phi_n|^2)|}{\mu |\Phi_n|^2}} \Phi_n. \quad (137)$$

The definition (137) may be inverted, to express  $\Phi_n$  in terms of  $\chi_n$ :

$$\begin{aligned} |\Phi_n|^2 &= \mu^{-1} \left[ \exp(\mu |\chi_n|^2) - 1 \right], \\ \Phi_n &= \sqrt{\frac{\exp(\mu |\chi_n|^2) - 1}{\mu |\chi_n|^2}} \chi_n. \end{aligned} \quad (138)$$

Making use of equations (138), the norm (114) and Hamiltonian (115) can be written in terms of the new canonical variables as

$$\mathcal{N} = \sum_n |\chi_n|^2, \quad (139)$$

$$\begin{aligned} \mathcal{H} = \sum_n &\left\{ -\left( \mathcal{A}_{n,n+1} (\chi_n \chi_{n+1}^* + \chi_{n+1} \chi_n^*) \right) \right. \\ &\left. - \frac{2}{\mu^2} \left[ \exp(\mu |\chi_n|^2) - 1 \right] \right\} + \frac{2}{\mu} \mathcal{N}, \end{aligned} \quad (140)$$

with the shorthand notation

$$\mathcal{A}_{n,n+1} = \sqrt{\frac{\left[\exp(\mu|\chi_n|^2) - 1\right]\left[\exp(\mu|\chi_{n+1}|^2) - 1\right]}{\mu^2 |\chi_n|^2 |\chi_{n+1}|^2}}. \quad (141)$$

Finally, equation (111) (with  $\nu \equiv 1$ ), if rewritten in terms of the variables  $\chi_n$ , may be represented in the standard Hamiltonian form, with the usual Poisson brackets:

$$i \frac{d\chi_n}{dt} = \frac{\partial \mathcal{H}}{\partial \chi_n^*}, \quad (142)$$

where Hamiltonian  $\mathcal{H}$  is taken as per equation (140).

**7.5.2. The quantum version of the Salerno model.** The SM was actually introduced from the very beginning in its quantum form (Salerno 1992). As usual, the quantization of the classical model is performed by replacing the canonically conjugate variables,  $\Phi_n$  and  $\Phi_n^*$ , by the creation and annihilation operators:

$$\Phi_n \rightarrow \hat{\Phi}_n, \Phi_n^* \rightarrow \hat{\Phi}_n^\dagger. \quad (143)$$

This correspondence replaces the classical deformed Poisson algebra (133) by the following deformed Heisenberg algebra:

$$[\hat{\Phi}_n, \hat{\Phi}_m^\dagger] = \hbar(1 + \mu\hat{\Phi}_n^\dagger\hat{\Phi}_n)\delta_{nm}, \quad (144)$$

$$[\hat{\Phi}_n, \hat{\Phi}_m] = [\hat{\Phi}_n^\dagger, \hat{\Phi}_m^\dagger] = 0.$$

These operators act on the standard Fock states as follows:

$$\hat{\Phi}_n^\dagger|N_n\rangle = \sqrt{\mu^{-1}[(1 + \hbar\mu)^{N+1} - 1]}|N_n + 1\rangle, \quad (145)$$

$$\hat{\Phi}_n^\dagger|N_n\rangle = \sqrt{\mu^{-1}[(1 + \hbar\mu)^{N+1} - 1]}|N_n - 1\rangle.$$

Further, the operator of the total number of particles is constructed as the quantum counterpart of the classical expression (114) for the total norm:

$$\hat{\mathcal{N}} = \frac{1}{\ln(1 + \hbar\mu)} \sum_n \ln(1 + \mu\hat{\Phi}_n^\dagger\hat{\Phi}_n). \quad (146)$$

It acts on the global Fock's state as the proper number operator:  $\hat{\mathcal{N}}|N\rangle = N|N\rangle$  (Salerno 1992).

The quantum Hamiltonian can be derived directly from its classical counterpart (115):

$$\hat{\mathcal{H}} = - \sum_n \left[ \hat{\Phi}_n^\dagger(\hat{\Phi}_{n-1} + \hat{\Phi}_{n+1}) + \frac{2}{\mu}\hat{\Phi}_n^\dagger\hat{\Phi}_n \right] + \frac{2}{\mu}\hat{\mathcal{N}}. \quad (147)$$

This Hamiltonian and commutation relations (144) lead to the Heisenberg equation of motion,  $i d\hat{\Phi}_n/dt = [\hat{\Phi}_n, \hat{\mathcal{H}}]$ , which can be derived in a straightforward way from the classical SM equation (111), replacing the classical variables by their quantum counterparts as per equations (143), yielding

$$i \frac{d\hat{\Phi}_n}{dt} = -(1 + \mu\hat{\Phi}_n^\dagger\hat{\Phi}_n)(\hat{\Phi}_{n-1} + \hat{\Phi}_{n+1}) - 2\hat{\Phi}_n^\dagger\hat{\Phi}_n^2. \quad (150)$$

The transformation of the classical canonical variables as per equation (138), which ‘rectifies’ the deformed Poisson brackets (133) into their standard form (135), suggests performing a similar canonical transformation in the quantum SM, which is indeed possible. The transformation is carried out as follows:

$$\hat{\Phi}_n^\dagger = \hat{F}_n\hat{\chi}_n^\dagger, \hat{\Phi}_n = \chi_n\hat{F}_n,$$

$$\hat{F}_n \equiv \sqrt{\frac{(1 + \hbar\mu)^{\chi_n^\dagger\chi_n} - 1}{\mu\chi_n^\dagger\chi_n}}. \quad (149)$$

The operators  $\chi_n^\dagger$  and  $\chi_n$ , unlike the original ones,  $\hat{\Phi}_n^\dagger$  and  $\hat{\Phi}_n$ , obey the usual commutation relations

$$[\hat{\chi}_n, \hat{\chi}_m] = [\hat{\chi}_n^\dagger, \hat{\chi}_m^\dagger] = 0, [\hat{\chi}_n, \hat{\chi}_m^\dagger] = \delta_{nm} \quad (150)$$

(see equations (144)), and they act on the Fock states in the usual way:

$$\hat{\chi}_n^\dagger|N_n\rangle = (N_n + 1)|N_n + 1\rangle, \quad (151)$$

$$\hat{\chi}_n|N_n\rangle = N_n|N_n - 1\rangle; \quad (152)$$

see equations (145). Further, the operator (146) of the total number of particles also takes the usual form in terms of these  $\hat{\chi}_n^\dagger$  and  $\hat{\chi}_n$ :  $\hat{\mathcal{N}} = \sum_n \hat{\chi}_n^\dagger\chi_n$  (see equation (146)), while the Hamiltonian, expressed in terms of  $\hat{\chi}_n^\dagger$  and  $\hat{\chi}_n$ , is a counterpart of its classical form (140):

$$\hat{\mathcal{H}} = - \sum_n \left\{ \hat{F}_n\hat{\chi}_n^\dagger(\hat{\chi}_{n+1}\hat{F}_{n+1} + \hat{\chi}_{n-1}\hat{F}_{n-1}) \right\} + \frac{2}{\mu}\hat{\mathcal{N}}, \quad (153)$$

$$+ \frac{2}{\mu^2}[(1 + \hbar\mu)^{\hat{\chi}_n^\dagger\hat{\chi}_n} - 1] \} + \frac{2}{\mu}\hat{\mathcal{N}}, \quad (154)$$

where the operators  $\hat{F}_n$  are defined in equation (149).

Finally, it is worthwhile mentioning that quantum counterparts of the classical solitons, which were reported in the classical (mean-field) versions of the SM with non-competing and competing nonlinearities in Cai *et al* (1996), (1997), Rasmussen *et al* (1997), Dmitriev *et al* (2003) and Gomez-Gardeñes *et al* (2006b), have not been constructed yet.

## 8. Conclusions

We have shown, for a number of selected cases, that the standard Hubbard model for fermions and its bosonic counterpart, the Bose–Hubbard model, even supplemented with nearest-neighbor interactions (extended models), are often insufficient for quantitatively describing the physics of ultracold atoms in optical lattices. While Hubbard was aware of additional terms contributing to tunneling in a nonlinear, density-dependent (interaction-based) fashion, it was Hirsch and co-workers who stressed the importance of these terms (also called bond-charge interactions) in the condensed-matter context. For some reason, it has only been in the last few years that the community investigating ultracold atoms has become aware of that fact—starting from the then puzzling observations of a shift of the Mott-superfluid border for Bose–Fermi mixtures. The density-induced tunneling effects become especially important for long-range (e.g. dipolar) interactions, although they may significantly contribute also for contact interactions, provided that these are sufficiently strong.

With increasing interaction strength the higher bands become important, which one can easily understand, since the Wannier functions are originally constructed for a periodic, interaction-free, single-particle potential. For sufficiently strong interactions, however, different Bloch bands become coupled. One may be tempted to try to treat the problem by using multi-band expansions—an approach that is doomed to failure due to the strongly increased complexity. Moreover, the tunneling between highly excited, extended Wannier states cannot be restricted to just nearby sites—and the advantage of a tight-binding approximation is, in some way, lost.

For moderate contact interactions, an effective approach is possible, described in detail in section 4. A possible prediagonalization of the on-site many-body Hamiltonian forms a convenient many-body ‘dressed’ basis. After expressing the tunnelings in that basis, one is led to an effective single-band Hamiltonian with population-dependent coefficients, thus obtaining effective three-body, four-body, etc, terms. The importance of these terms has already been verified for Bose–Fermi mixtures as well as in collapse and revival experiments. Clearly, however, for sufficiently strong interactions one expects problems with that approach, and the general solution is not yet known.

For longer-range dipolar interactions, the problems are even more severe. Due to the nature of the dipolar interactions, the integrals (65) increase in value for higher Bloch bands. As soon as the interaction couples to higher bands, the multi-orbital approach presented above for contact interactions ceases to converge. At present, there is no known solution to this problem. One possible way of attacking it is to cease to use the Wannier localized basis for higher excited bands, and to work directly with the Bloch functions (Dutta *et al* 2014). Yet there exist other potential problems for realistic polar molecules—e.g. the high density of rovibrational molecular states, which may lead to the formation of long-lived molecular complexes as described in Mayle *et al* (2013). That effect will lead to a loss of molecules and potentially may limit the density of molecules in an optical lattice.

All of these effects may complicate the treatment of ultracold atoms in optical lattices, but they also generate a manifold of novel quantum phenomena not present in the standard Hubbard model. Despite the recent progress, there is still much to be learnt about interacting ultracold atoms and molecules in optical lattice potentials. There are a lot of questions arising beyond the standard Hubbard model.

## Acknowledgments

All of us would like to acknowledge long-term collaboration with ICFO. We thank R Chhajlany and P Grzybowski for discussions and critical reading of the manuscript. D-SL thanks O Jürgensen and K Sengstock for stimulating discussions. This work was supported by the Polish National Science Center within projects Nos DEC-2012/04/A/ST2/00088 (OD and JZ), DEC-2011/01/D/ST2/02019 (TS) and DEC-2012/04/A/ST2/00090 (MG). PH and ML acknowledge support from EU IP SIQS. PH was also supported by SFB FoQuS (FWF Project No. F4006-N16) and ERC synergy grant UQUAM. ML acknowledges financial support

from Spanish Government Grants TOQATA (FIS2008-01236) and FOCUS, EU STREP EQuaM, and ERC Advanced Grants QUAGATUA and OSYRIS. ML and JZ also acknowledge support from the EU Horizon 2020-FET QUIC. D-SL acknowledges funding by the Deutsche Forschungsgemeinschaft (grants SFB 925 and GRK 1355).

## Appendix A. Multi-orbital dressing of off-site processes

As briefly described in sections 4.5 and 4.6, the transformation to a dressed band which incorporates higher orbital contributions allows treating multi-orbital Hamiltonians effectively with single-band methods. In the following, it is shown how a two-site operator, such as that for the tunneling, can be represented and computed within the dressed band approach following Bissbort *et al* (2012), Jürgensen *et al* (2012), Lühmann *et al* (2012). First, we turn to the representation of operators in the dressed band using the ground state  $\Psi(n)$  of the  $n$ -particle on-site problem (74). Within a single-orbital treatment, any tight-binding two-site operator can be decomposed into the form

$$\hat{O}_{\text{SO}} = A \hat{O}_L \hat{O}_R, \quad (\text{A.1})$$

with an amplitude  $A$  and operators  $O_i$  consisting of creation/annihilation operators  $\hat{b}_i^\dagger / \hat{b}_i$  on the left (L) or right (R) site, e.g. the single-particle tunneling  $-\hat{J} \hat{b}_L^\dagger \hat{b}_R$ . The multi-orbitally dressed band (indicated by a tilde) is constructed with creation and annihilation operators that fulfill the usual relations

$$\begin{aligned} \tilde{b}_i |\Psi(n)\rangle_i &= \sqrt{n} |\Psi(n-1)\rangle_i, \\ \tilde{b}_i^\dagger |\Psi(n)\rangle_i &= \sqrt{n+1} |\Psi(n+1)\rangle_i. \end{aligned} \quad (\text{A.2})$$

Note that by construction, the states  $\Psi(n)$  are still orthogonal with respect to the particle number  $n$ , and therefore the particle number operator in Wannier and dressed bases are equivalent:  $\tilde{n}_i = \tilde{b}_i^\dagger \tilde{b}_i = \hat{n}_i$ . Formally, by replacing in  $\hat{O}_L$  and  $\hat{O}_R$  the operators  $\hat{b}_i^\dagger / \hat{b}_i$  with their dressed counterparts  $\tilde{b}_i^\dagger / \tilde{b}_i$ , the operator

$$\tilde{O} = \tilde{O}_L \tilde{O}_R \tilde{A}_{\hat{n}_R, \hat{n}_L} \quad (\text{A.3})$$

of the dressed band is constructed. Here, the indices of  $\tilde{A}$  have operator form, which expresses that  $\tilde{A}$  is projected to the respective occupation-number-dependent amplitude  $\tilde{A}_{n_R, n_L}$  (see equation (81)).

While the definitions for the interaction-dressed band are given above, the actual problem is to compute the dressed band amplitudes  $\tilde{A}_{n_R, n_L}$  that effectively include all orbital processes. In general, a multi-orbital two-site operator can be decomposed as

$$\hat{O}_{\text{MO}} = \sum_{\{\alpha\}, \{\beta\}} A^{\{\alpha\}, \{\beta\}} \hat{O}_L^{\{\alpha\}} \hat{O}_R^{\{\beta\}}, \quad (\text{A.4})$$

where the summation is over all possible sets of orbitals  $\{\alpha\} = \{\alpha_1, \alpha_2, \dots\}$  and  $\{\beta\} = \{\beta_1, \beta_2, \dots\}$ ,  $A^{\{\alpha\}, \{\beta\}}$  is the amplitude, and  $\hat{O}_i^{\{\alpha\}}$  consists of creation and annihilation operators  $\hat{b}_i^{\alpha_k\dagger}$  and  $\hat{b}_i^{\alpha_k}$  at site  $i$  in the orbital  $\alpha_k$ . For the multi-orbital tunneling

$$t_{\text{MO}} = - \sum_{\alpha} t^{\alpha} \hat{b}_{\text{L}}^{\alpha\dagger} \hat{b}_{\text{R}}^{\alpha}, \quad (\text{A.5})$$

the operators on the left and the right site,  $\hat{O}_{\text{L}}^{\alpha} = \hat{b}_{\text{L}}^{\alpha\dagger}$  and  $\hat{O}_{\text{R}}^{\beta} = \hat{b}_{\text{R}}^{\beta\dagger}$ , depend only on single orbitals,  $\{\alpha\} = \alpha$  and  $\{\beta\} = \beta$ , with an orbital-conserving amplitude  $A^{\alpha, \beta} = - t^{\alpha} \delta_{\alpha, \beta}$ . The effective amplitude  $\tilde{A}_{n_{\text{R}}, n_{\text{L}}}$  is obtained from the matrix element  $\langle \Psi_{\text{F}} | \hat{O}_{\text{MO}} | \Psi_{\text{I}} \rangle$ , where  $\Psi_{\text{I}}(n_{\text{L}}, n_{\text{R}})$  denotes the initial and  $\Psi_{\text{F}} = \Psi(n_{\text{L}'}, n_{\text{R}'})$  the final state of the process. The occupation-dependent amplitude includes the summation over all multi-orbital processes. Since the states are products of the individual lattice sites,  $|\Psi(n_{\text{L}})\rangle |\Psi(n_{\text{R}})\rangle$ , the effective amplitude  $\tilde{A}$  decomposes into individual site contributions:

$$\begin{aligned} \tilde{A}_{n_{\text{R}}, n_{\text{L}}} = \frac{1}{N} \sum_{\{\alpha\}, \{\beta\}} A^{\{\alpha\}, \{\beta\}} & \langle \Psi(n'_{\text{L}}) | \hat{O}_{\text{L}}^{\{\alpha\}} | \Psi(n_{\text{L}}) \rangle \\ & \times \langle \Psi(n'_{\text{R}}) | \hat{O}_{\text{R}}^{\{\beta\}} | \Psi(n_{\text{R}}) \rangle. \end{aligned} \quad (\text{A.6})$$

The prefactor  $N = \langle \Psi_{\text{F}} | \hat{O}_{\text{L}} \hat{O}_{\text{R}} | \Psi_{\text{I}} \rangle$  is needed for the correct normalization, e.g.  $N = \sqrt{n_{\text{L}}(n_{\text{R}} + 1)}$  for the tunneling process. Since  $\hat{O}_i^{\{\alpha\}}$  acts on the single-site multi-orbital Wannier basis,  $\tilde{A}_{n_{\text{R}}, n_{\text{L}}}$  can be evaluated using the on-site coefficients of the many-particle state (75).

## References

- Ablowitz M J and Ladik J F 1976 Nonlinear differential-difference equations and Fourier analysis *J. Math. Phys.* **17** 1011
- Ablowitz M J, Musslimani Z H and Biondini G 2002 Methods for discrete solitons in nonlinear lattices *Phys. Rev. E* **65** 026602
- Alba E, Fernandez-Gonzalvo X, Mur-Petit J, Pachos J K and Garcia-Ripoll J J 2011 Seeing topological order in time-of-flight measurements *Phys. Rev. Lett.* **107** 235301
- Albus A, Illuminati F and Eisert J 2003 Mixtures of bosonic and fermionic atoms in optical lattices *Phys. Rev. A* **68** 023606
- Alon O E, Streltsov A I and Cederbaum L S 2005 Zoo of quantum phases and excitations of cold bosonic atoms in optical lattices *Phys. Rev. Lett.* **95** 030405
- Amadon J C and Hirsch J E 1996 Metallic ferromagnetism in a single-band model: effect of band filling and coulomb interactions *Phys. Rev. B* **54** 6364
- Anderlini M, Lee P J, Brown B L, Sebby-Strabley J, Phillips W D and Porto J V 2007 Controlled exchange interaction between pairs of neutral atoms in an optical lattice *Nature* **448** 452
- Ashcroft N W and Mermin N D 1976 *Solid State Physics* (Philadelphia, PA: Saunders)
- Aspuru-Guzik A and Walther P 2012 Photonic quantum simulators *Nat. Phys.* **8** 285–91
- Auerbach A 1994 *Interacting Electrons and Quantum Magnetism* (New York: Springer)
- Bakr W S, Preiss P M, Tai M E, Ma R, Simon J and Greiner M 2011 Interaction-induced orbital excitation blockade of ultracold atoms in an optical lattice *Nature* **480** 500–3
- Banerjee D, Bögli M, Dalmonte M, Rico E, Stebler J, Wiese U-J and Zoller P 2013 Atomic quantum simulation of U(N) and SU(N) non-abelian lattice gauge theories *Phys. Rev. Lett.* **110** 125303
- Baranov M A 2008 Theoretical progress in many-body physics with ultracold dipolar gases *Phys. Rep.* **464** 71
- Barbiero L and Salasnich L 2014 Quantum bright solitons in a quasi-1D optical lattice *Phys. Rev. A* **89** 063605
- Barbiero L, Malomed B A and Salasnich 2014 Quantum bright solitons in the Bose–Hubbard model with site-dependent repulsive interactions *Phys. Rev. A* **90** 063611
- Batrouni G G, Hébert F and Scalettar R T 2006 Supersolid phases in the one-dimensional extended soft-core bosonic Hubbard model *Phys. Rev. Lett.* **97** 087209
- Best T, Will S, Schneider U, Hackermüller L, van Oosten D, Bloch I and Lühmann D S 2009 Role of interactions in  $^{87}\text{Rb}$ – $^{40}\text{K}$  Bose–Fermi mixtures in a 3D optical lattice *Phys. Rev. Lett.* **102** 030408
- Bissbort U, Deuretzbacher F and Hofstetter W 2012 Effective multibody-induced tunneling and interactions in the Bose–Hubbard model of the lowest dressed band of an optical lattice *Phys. Rev. A* **86** 023617
- Blatt R and Roos C F 2012 Quantum simulations with trapped ions *Nat. Phys.* **8** 277–84
- Bloch I, Dalibard J and Nascimbène S 2012 Quantum simulations with ultracold quantum gases *Nat. Phys.* **8** 267–76
- Bloch I, Dalibard J and Zwerger W 2008 Many-body physics with ultracold gases *Rev. Mod. Phys.* **80** 885
- Bogoliubov N 1947 On the theory of superfluidity *J. Phys.* **11** 23
- Borovkova O V, Kartashov Y V, Torner L and Malomed B A 2011 Bright solitons from defocusing nonlinearities *Phys. Rev. E* **84** 035602
- Browaeys A, Häffner H, McKenzie C, Rolston S L, Helmerson K and Phillips W D 2005 Transport of atoms in a quantum conveyor belt *Phys. Rev. A* **72** 053605
- Büchler H P 2010 Microscopic derivation of Hubbard parameters for cold atomic gases *Phys. Rev. Lett.* **104** 090402
- Büchler H P, Demler E, Lukin M, Micheli A, Prokof’ev N, Pupillo G and Zoller P 2007 Strongly correlated 2D quantum phases with cold polar molecules: controlling the shape of the interaction potential *Phys. Rev. Lett.* **98** 060404
- Busch T, Englert B G, Rzążewski K and Wilkens M 1998 Two cold atoms in a harmonic trap *Found. Phys.* **28** 549
- Cai D, Bishop A R and Grønbæk Jensen N 1996 Perturbation theories of a discrete, integrable nonlinear Schrödinger equation *Phys. Rev. E* **53** 4131
- Cai D, Bishop A R and Grønbæk Jensen N 1997 Resonance in the collision of two discrete intrinsic localized excitations *Phys. Rev. E* **56** 7246
- Cai Z and Wu C 2011 Complex and real unconventional Bose–Einstein condensations in high orbital bands *Phys. Rev. A* **84** 033635
- Campbell G K, Mun J, Boyd M, Medley P, Leanhardt A E, Marcassa L G, Pritchard D E and Ketterle W 2006 Imaging the Mott insulator shells by using atomic clock shifts *Science* **313** 649–52
- Cao L, Brouzos I, Zöllner S and Schmelcher P 2011 Interaction-driven interband tunneling of bosons in the triple well *New J. Phys.* **13** 033032
- Capogrosso-Sansone B, Trefzger C, Lewenstein M, Zoller P and Pupillo G 2010 Quantum Phases of Cold Polar Molecules in 2D Optical Lattices *Phys. Rev. Lett.* **104** 125301
- Carrasquilla J, Manmana S. R and Rigol M 2013 Scaling of the gap, fidelity susceptibility, and bloch oscillations across the superfluid-to-mott-insulator transition in the 1D Bose–Hubbard model *Phys. Rev. A* **87** 043606
- Cazalilla M A, Citro R, Giamarchi T, Orignac E and Rigol M 2011 One dimensional bosons: from condensed matter systems to ultracold gases *Rev. Mod. Phys.* **83** 1405–66
- Cetoli A and Lundh E 2010 Reentrant transition of bosons in a quasiperiodic potential *Eur. Phys. Lett.* **90** 46001
- Chen Y P, Hitchcock J, Dries D, Junker M, Welford C and Hulet R G 2008 Phase coherence and superfluid-insulator transition in a disordered Bose–Einstein condensate *Phys. Rev. A* **77** 033632
- Chern G-W and Wu C 2011 Orbital ice: An exact Coulomb phase on the diamond lattice *Phys. Rev. E* **84** 061127
- Chin C, Grimm R, Julienne P and Tiesinga E 2010 Feshbach resonances in ultracold gases *Rev. Mod. Phys.* **82** 1225
- Chiofalo M L, Polini M and Tosi M P 2000 Collective excitations of a periodic bose condensate in the Wannier representation *Eur. Phys. J. D* **11** 371

- Chu S 1998 Nobel Lecture: The manipulation of neutral particles *Rev. Mod. Phys.* **70** 685
- Cirac J I and Zoller P 2004 New frontiers in quantum information with atoms and ions *Phys. Today* **57** 38
- Cirac J I and Zoller P 1995 Quantum computations with cold trapped ions *Phys. Rev. Lett.* **74** 4091
- Cohen-Tannoudji C 1998 Nobel Lecture: Manipulating atoms with photons *Rev. Mod. Phys.* **70** 707
- Collin A, Larson J and Martikainen J P 2010 Quantum states of p-band bosons in optical lattices *Phys. Rev. A* **81** 023605
- Corboz P, Evenly G, Verstraete F and Vidal G 2010a Simulation of interacting fermions with entanglement renormalization *Phys. Rev. A* **81** 010303
- Corboz P, Jordan J and Vidal G 2010b Simulation of fermionic lattice models in 2D with projected entangled-pair states: next-nearest neighbor hamiltonians *Phys. Rev. B* **82** 245119
- Cornell E A and Wieman C E 2002 Nobel Lecture: Bose-Einstein condensation in a dilute gas, the first 70 years and some recent experiments *Rev. Mod. Phys.* **74** 875
- Cramer M, Ospelkaus S, Ospelkaus C, Bongs K, Sengstock K and Eisert J 2008 Do mixtures of bosonic and fermionic atoms adiabatically heat up in optical lattices? *Phys. Rev. Lett.* **100** 140409
- Cramer M 2011 Interaction-dependent temperature effects in Bose-Fermi mixtures in optical lattices *Phys. Rev. Lett.* **106** 215302
- Dalibard J, Gerbier F, Juzeliūnas G and Öhberg P 2011 Colloquium: Artificial gauge potentials for neutral atoms *Rev. Mod. Phys.* **83** 1523
- Dalla Torre E G, Berg E and Altman E 2006 Hidden order in 1d bose insulators *Phys. Rev. Lett.* **97** 260401
- Daley A J and Simon J 2013 Effective three-body interactions via photon-assisted tunneling in an optical lattice arXiv:1311.1783[cond-mat.quant-gas]
- Daley A J, Taylor J M, Diehl S, Baranov M and Zoller P 2009 Atomic three-body loss as a dynamical three-body interaction *Phys. Rev. Lett.* **102** 040402
- Dalmonte M, Di Dio M, Barbiero L and Ortolani F 2011 Homogeneous and inhomogeneous magnetic phases of constrained dipolar bosons *Phys. Rev. B* **83** 155110
- Damski B and Zakrzewski J 2006 Mott-insulator phase of the one-dimensional Bose-Hubbard model: A high-order perturbative study *Phys. Rev. A* **74** 043609
- Deng X and Santos L 2011 Entanglement spectrum of 1D extended Bose-Hubbard models *Phys. Rev. B* **84** 085138
- de Paz A, Chotia A, Maréchal E, Pedri P, Vernac L, Gorceix O and Laburthe-Tolra B 2013a Resonant demagnetization of a dipolar Bose-Einstein condensate in a 3D optical lattice *Phys. Rev. A* **87** 051609
- de Paz A, Sharma A, Chotia A, Maréchal E, Huckans J H, Pedri P, Santos L, Gorceix O, Vernac L and Laburthe-Tolra B 2013b Nonequilibrium quantum magnetism in a dipolar lattice gas *Phys. Rev. Lett.* **111** 185305
- Dmitriev S V, Kevrekidis P G, Malomed B A and Frantzeskakis D J 2003 Two-soliton collisions in a near-integrable lattice system *Phys. Rev. E* **68** 056603
- Doggen E V H, Korolyuk A, Törmä P and Kinnunen J J 2014 One-dimensional fermi polaron in a combined harmonic and periodic potential *Phys. Rev. A* **89** 053621
- Dutta O, Eckardt A, Hauke P, Malomed B and Lewenstein M 2011 Bose-Hubbard model with occupation-dependent parameters *New J. Phys.* **13** 023019
- Dutta O, Przysiezna A and Zakrzewski J 2014a Spontaneous magnetization and anomalous Hall effect in an emergent Dice lattice arXiv:1405.2565
- Dutta O, Lewenstein M and Zakrzewski J 2014b Many body population trapping in ultracold dipolar gases *New J. Phys.* **16** 052002
- Eckardt A, Hauke P, Soltan-Panahi P, Becker C, Sengstock K and Lewenstein M 2010 Frustrated quantum antiferromagnetism with ultracold bosons in a triangular lattice *Europhys. Lett.* **89** 10010
- Eckardt A and Lewenstein M 2010 Controlled hole doping of a Mott insulator of ultracold fermionic atoms *Phys. Rev. A* **82** 011606
- Eckardt A, Weiss C and Holthaus M 2005 Superfluid-Insulator Transition in a Periodically Driven Optical Lattice *Phys. Rev. Lett.* **95** 260404
- Einstein A and de Haas W J 1915 Experimenteller nachweis der ampèreschen molekularströme *Verh. Deutsch. Phys. Ges.* **17** 152–70, 203
- Ejima S, Lange F, Fehske H, Gebhard F and Münster K z 2013 One-dimensional Bose-Hubbard model with local three-body interactions *Phys. Rev. A* **88** 063625
- Elstner N and Monien H 1999 Dynamics and thermodynamics of the Bose-Hubbard model *Phys. Rev. B* **59** 12184
- Essler F H L, Frahm H, Göhmann F, Klümper A and Korepin V E 2005 *The 1D Hubbard Model* (Cambridge: Cambridge University Press)
- Ferlaino F, D'Errico C, Roati G, Zaccanti M, Inguscio M, Modugno G and Simoni A 2006 Feshbach spectroscopy of a K-Rb atomic mixture *Phys. Rev. A* **73** 040702
- Feynman R P 1986 Quantum mechanical computers *Found. Phys.* **16** 507
- Fisher M E and Selke W 1980 Infinitely Many Commensurate Phases in a Simple Ising Model *Phys. Rev. Lett.* **44** 1502
- Fisher M P A, Weichman P B, Grinstein G and Fisher D S 1989 Boson localization and the superfluid-insulator transition *Phys. Rev. B* **40** 546
- Gawryluk K, Bongs K and Brewczyk M 2011 How to observe dipolar effects in spinor Bose-Einstein condensates *Phys. Rev. Lett.* **106** 140403
- Gawryluk K, Brewczyk M, Bongs K and Gajda M 2007 Resonant Einstein-de Haas effect in a rubidium condensate *Phys. Rev. Lett.* **99** 130401
- Georges A, Kotliar G, Krauth W and Rozenberg M J 2013 Dynamical mean-field theory of strongly correlated fermion systems and the limit of infinite dimensions *Rev. Mod. Phys.* **340** 13
- Gersch H A and Knollman G C 1963 Quantum cell model for bosons *Phys. Rev.* **129** 959–67
- Giorgini S, Pitaevskii L P and Stringari S 2008 Theory of ultracold atomic Fermi gases *Rev. Mod. Phys.* **80** 1215
- Gligorić G, Maluckov A, Hadzievski L and Malomed B A 2013 Discrete localized modes supported by an inhomogeneous defocusing nonlinearity *Phys. Rev. E* **88** 032905
- Goldman N, Juzeliunas G, Ohberg P and Spielman I B 2014 Light-induced gauge fields for ultracold atoms *Rep. Prog. Phys.* **77** 126401
- Goldman N, Satija I, Nikolic P, Bermudez A, Martin-Delgado M A, Lewenstein M and Spielman I B 2010 Realistic Time-Reversal Invariant Topological Insulators with Neutral Atoms *Phys. Rev. Lett.* **105** 255302
- Gomez-Gardeñes J, Malomed B A, Floria L M and Bishop A R 2006a Solitons in the Salerno model with competing nonlinearities *Phys. Rev. E* **74** 036607
- Gomez-Gardeñes J, Malomed B A, Floria L M and Bishop A R 2006b Solitons in the Salerno model with competing nonlinearities *Phys. Rev. E* **73** 036608
- Goyal K, Reichenbach I and Deutsch I 2010 P-wave optical feshbach resonances in Yb-171 *Phys. Rev. A* **82** 062704
- Greif D, Uehlinger T, Jotzu G, Tarruell L and Esslinger T 2013 Short-range quantum magnetism of ultracold fermions in an optical lattice *Science* **340** 1307–10
- Greiner M, Mandel O, Esslinger T, Hänsch T W and Bloch I 2002 Quantum phase transition from a superfluid to a Mott insulator in a gas of ultracold atoms *Nature* **415** 39
- Gribakin G F and Flambaum V V 1993 Calculation of the scattering length in atomic collisions using the semiclassical approximation *Phys. Rev. A* **48** 546
- Grimm R, Weidmüller M and Ovchinnikov Y B 2000 Optical dipole traps for neutral atoms *Adv. At. Mol. Opt. Phys.* **42** 95

- Gross E P 1961 Structure of a quantized vortex in boson systems *Nuovo Cimento* **20** 454
- Grzybowski P R and Chhajlany R W 2012 Hubbard-I approach to the Mott transition *Phys. Status Solidi B* **249** 2231
- Guinea F and Schön G 1988 Quantum fluctuations in normal metal-superconductor and superconductor-normal metal-superconductor devices *Physica B* **152** 165
- Guinea F 1988a Phenomenological description of a superconductor with an anisotropic order parameter *Physica C* **153-5** 673
- Guinea F 1988b Real space renormalization group study of Cu-O planes with coulomb repulsion *Physica C* **153-5** 1231
- Günter K, Stöferle T, Moritz H, Köhl M and Esslinger T 2005 P-wave interactions in low-dimensional fermionic gases *Phys. Rev. Lett.* **95** 230401
- Günter K, Stöferle T, Moritz H, Köhl M and Esslinger T 2006 Bose-Fermi mixtures in a three-dimensional optical lattice *Phys. Rev. Lett.* **96** 180402
- Gu S J, Deng S S, Li Y Q and Lin H Q 2004 Locally critical quantum phase transitions in strongly correlated metals *Phys. Rev. Lett.* **93** 086402
- Hasan M Z and Kane C L 2010 Colloquium: topological insulators *Rev. Mod. Phys.* **82** 3045
- Hauke P, Cucchietti F M, Tagliacozzo L, Deutsch I and Lewenstein M 2012a Can one trust quantum simulators? *Rep. Prog. Phys.* **75** 082401
- Hauke P *et al* 2012b Non-abelian gauge fields and topological insulators in shaken optical lattices *Phys. Rev. Lett.* **109** 145301
- Hauke P, Zhao E, Goyal K, Deutsch I H, Liu W V and Lewenstein M 2011 Orbital order of spinless fermions near an optical feshbach resonance *Phys. Rev. A* **84** 051603
- Hazzard K R A and Mueller E J 2010 On-site correlations in optical lattices: band mixing to coupled quantum hall puddles *Phys. Rev. A* **81** 031602
- Heinze J, Götz S, Krauser J S, Hundt B, Fläschner N, Lühmann D S, Becker C and Sengstock K 2011 Multiband spectroscopy of ultracold fermions: observation of reduced tunneling in attractive Bose-Fermi mixtures *Phys. Rev. Lett.* **107** 135303
- Hirsch J E 1984 Charge-density-wave to spin-density-wave transition in the extended Hubbard model *Phys. Rev. Lett.* **53** 2327
- Hirsch J E 1989 Bond-charge repulsion and hole superconductivity *Physica C* **158** 326
- Hirsch J E 1994 Inapplicability of the Hubbard model for the description of real strongly correlated electrons *Physica B* **199** 200366
- Ho T L 1998 Spinor Bose condensates in optical traps *Phys. Rev. Lett.* **81** 742-5
- Houck A A, Türeci H E and Koch J 2012 On-chip quantum simulation with superconducting circuits *Nat. Phys.* **8** 292-9
- Huang B and Wan S 2010 Bose-Hubbard phase transition with two- and three-body interaction in a magnetic field *Phys. Lett. A* **374** 4364-8
- Hubbard J 1963 Electron correlations in narrow energy bands *Proc. R. Soc. A* **276** 238-57
- Hubbard J 1978 Generalized Wigner lattices in one dimension and some applications to tetracyanoquinodimethane (TCNQ) salts *Phys. Rev. B* **17** 494
- Imriska J, Iazzi M, Wang L, Gull E, Greif D, Uehlinger T, Jotzu G, Tarruell L, Esslinger T and Troyer M 2014 Thermodynamics and magnetic properties of the anisotropic 3D Hubbard model *Phys. Rev. Lett.* **112** 115301
- Isachsen A and Girvin S M 2005 Multiflavor bosonic Hubbard models in the first excited Bloch band of an optical lattice *Phys. Rev. A* **72** 053604
- Jaksch D, Briegel H J, Cirac J I, Gardiner C W and Zoller P 1999 Entanglement of atoms via cold controlled collisions *Phys. Rev. Lett.* **82** 1975
- Jaksch D, Bruder C, Cirac J I, Gardiner C W and Zoller P 1998 Cold bosonic atoms in optical lattices *Phys. Rev. Lett.* **81** 3108
- Jaksch D and Zoller P 2005 Entanglement of atoms via cold controlled collisions *Ann. Phys.* **315** 52
- Johnson P R, Tiesinga E, Porto J V and Williams C J 2009 Effective three-body interactions of neutral bosons in optical lattices *New J. Phys.* **11** 093022
- Jördens R, Strohmaier N, Günter K, Moritz H and Esslinger T 2008 A Mott insulator of fermionic atoms in an optical lattice *Nature* **455** 204
- Jürgensen O, Meinert F, Mark M J, Nägerl H C and Lühmann D S 2014 Observation of density-induced tunneling *Phys. Rev. Lett.* **113** 193003
- Jürgensen O, Sengstock K and Lühmann D S 2012 Density-induced processes in quantum gas mixtures in optical lattices *Phys. Rev. A* **86** 043623
- Kapitula T, Kevrekidis P G and Malomed B A 2001 Stability of multiple pulses in discrete systems *Phys. Rev. E* **63** 036604
- Kawaguchi Y, Saito H and Ueda M 2006 Einstein-de Haas effect in dipolar Bose-Einstein condensates *Phys. Rev. Lett.* **96** 080405
- Kawaguchi Y and Ueda M 2012 Spinor Bose-Einstein condensates *Phys. Rep.* **520** 253-381
- Ketterle W 2002 Nobel lecture: When atoms behave as waves: Bose-Einstein condensation and the atom laser *Rev. Mod. Phys.* **74** 1131
- Kevrekidis P G 2003 On a class of discretizations of Hamiltonian nonlinear partial differential equations *Physica D* **183** 68
- Kevrekidis P G 2009 *The Discrete Nonlinear Schrödinger Equation: Mathematical Analysis, Numerical Computations, and Physical Perspectives* (Berlin: Springer)
- Khaliullin G 2005 Orbital order and fluctuations in Mott insulators *Prog. Theor. Phys. Suppl.* **160** 155
- Kitagawa T, Berg E, Rudner M and Demler E 2010 Topological characterization of periodically driven quantum systems *Phys. Rev. B* **82** 235114
- Kivelson S, Su W P, Schrieffer J R and Heeger A J 1987 Missing bond-charge repulsion in the extended Hubbard model: effects in polyacetylene *Phys. Rev. Lett.* **58** 1899
- Köhl M, Moritz H, Stöferle T, Günter K and Esslinger T 2005 Fermionic atoms in a three dimensional optical lattice: observing fermi surfaces, dynamics, and interactions *Phys. Rev. Lett.* **94** 080403
- Kohn W 1959 Analytic properties of bloch waves and wannier functions *Phys. Rev.* **115** 809-21
- Krutitsky K V 2015 Ultracold bosons with short-range interaction in regular optical lattices arXiv:1501.03125
- Kugel K I and Khomskii D I 1982 The Jahn-Teller effect and magnetism: transition metal compounds *Sov. Phys.—Usp.* **25** 231
- Kühner T D and Monien H 1998 Phases of the one-dimensional Bose-Hubbard model *Phys. Rev. B* **58** R14741
- Kühner T D, White S R and Monien H 2000 One-dimensional Bose-Hubbard model with nearest-neighbor interaction *Phys. Rev. B* **61** 12474
- Kuklov A B 2006 Unconventional strongly interacting Bose-Einstein condensates in optical lattices *Phys. Rev. Lett.* **97** 110405
- Laedke E W, Spatschek K H and Turitsyn S K 1994 Stability of Discrete Solitons and Quasicollapse to Intrinsically Localized Modes *Phys. Rev. Lett.* **73** 1055
- Lahaye T, Menotti C, Santos L, Lewenstein M and Pfau T 2009 The physics of dipolar bosonic quantum gases *Rep. Prog. Phys.* **72** 126401
- Landau L D and Lifshitz E M 1987 *Quantum Mechanics* (New York: Pergamon)
- Larson J, Collin A and Martikainen J P 2009 Multiband bosons in optical lattices *Phys. Rev. A* **79** 033603
- Lee P A, Nagaosa N and Wen X G 2006 Doping a Mott insulator: Physics of high-temperature superconductivity *Rev. Mod. Phys.* **78** 17

- Lee P A 2008 From high temperature superconductivity to quantum spin liquid: progress in strong correlation physics *Rep. Prog. Phys.* **71** 012501
- Lee Y-W and Yang M-F 2010 Superfluid-insulator transitions in attractive Bose–Hubbard model with three-body constraint *Phys. Rev. A* **81** 061604
- Lewenstein M and Liu W V 2011 Optical lattices: Orbital dance *Nat. Phys.* **7** 101
- Lewenstein M, Sanpera A, Ahufinger V, Damski B, Sen De A and Sen U 2007 Ultracold atomic gases in optical lattices: mimicking condensed matter physics and beyond *Adv. Phys.* **56** 243
- Lewenstein M, Sanpera A and Ahufinger V 2012 *Ultracold Atoms in Optical Lattices: Simulating Many-Body Quantum Systems* (Oxford: Oxford University Press)
- Liberto M D, Creffield C E, Japaridze G I and Smith C M 2014 Quantum simulation of correlated-hopping models with fermions in optical lattices *Phys. Rev. A* **89** 013624
- Lignier H, Sias C, Ciampini D, Singh Y, Zenesini A, Morsch O and Arimondo E 2007 Dynamical Control of Matter-Wave Tunneling in Periodic Potentials *Phys. Rev. Lett.* **99** 220403
- Liu W. V and Wu C 2006 Atomic matter of nonzero-momentum Bose-Einstein condensation and orbital current order *Phys. Rev. A* **74** 013607
- Li Y, Lieb E H and Wu C 2014 Exact results on itinerant ferromagnetism in multi-orbital systems on square and cubic lattices *Phys. Rev. Lett.* **112** 217201
- Li J, Yu Y, Dudarev A M and Niu Q 2006 Interaction broadening of wannier functions and mott transitions in atomic BEC *New J. Phys.* **8** 154
- Li X, Zhang Z and Liu V W 2012 Time-Reversal Symmetry Breaking of p-Orbital Bosons in a One-Dimensional Optical Lattice *Phys. Rev. Lett.* **108** 175302
- Li X, Zhao E and Liu W V 2013 Topological states in a ladder-like optical lattice containing ultracold atoms in higher orbital bands *Nat. Commun.* **4** 1523
- Łącki M, Damski B and Zakrzewski J 2014 Numerical studies of ground-state fidelity of the Bose–Hubbard model *Phys. Rev. A* **89** 033625
- Łącki M, Delande D and Zakrzewski J 2013 Dynamics of cold bosons in optical lattices: effects of higher bloch bands *New J. Phys.* **15** 013062
- Łącki M and Zakrzewski J 2013 Fast dynamics for atoms in optical lattices *Phys. Rev. Lett.* **110** 065301
- Lühmann D S, Bongs K, Sengstock K and Pfannkuche D 2008 Self-trapping of bosons and fermions in optical lattices *Phys. Rev. Lett.* **101** 050402
- Lühmann D S, Jürgensen O and Sengstock K 2012 Multi-orbital and density-induced tunneling of bosons in optical lattices *New J. Phys.* **14** 033021
- Lutchyn R M, Tewari S and Das Sarma S 2009 Loss of superfluidity by fermions in the boson Hubbard model on an optical lattice *Phys. Rev. A* **79** 011606
- Maik M, Hauke P, Dutta O, Lewenstein M and Zakrzewski J 2013 Density-dependent tunneling in the extended Bose–Hubbard model *New J. Phys.* **15** 113041
- Major J, Łącki M and Zakrzewski J 2014 Reexamination of the variational Bose–Hubbard model *Phys. Rev. A* **89** 043626
- Malomed B A, Fujioka J, Espinosa-Cerón A, Rodríguez R F and González S 2006 Moving embedded lattice solitons *Chaos* **16** 013112
- Malomed B A, Kaup D J and Van Gorder R A 2012 Unstaggered-staggered solitons in two-component discrete nonlinear Schrödinger lattices *Phys. Rev. E* **85** 026604
- Mark M J, Haller E, Lauber K, Danzl J G, Daley A J and Nägerl H C 2011 Precision measurements on a tunable mott insulator of ultracold atoms *Phys. Rev. Lett.* **107** 175301
- Mark M J, Haller E, Lauber K, Danzl J G, Janisch A, Büchler H P, Daley A J and Nägerl H C 2012 Preparation and spectroscopy of a metastable mott-insulator state with attractive interactions *Phys. Rev. Lett.* **108** 215302
- Martikainen J P 2011 Dynamical instability and loss of P-band bosons in optical lattices *Phys. Rev. A* **83** 013610
- Marzari N, Mostofi A, Yates J, Suza I and Vanderbilt D 2012 Maximally localized Wannier functions: Theory and applications *Rev. Mod. Phys.* **84** 1419
- Marzari N and Vanderbilt D 1997 Maximally localized generalized Wannier functions for composite energy bands *Phys. Rev. B* **56** 12847
- Mathy C J M, Huse D A and Hulet R G 2012 Enlarging and cooling the Néel state in an optical lattice *Phys. Rev. A* **86** 023606
- Mayle M, Quéméner G, Ruzic B P and Bohn J L 2013 Scattering of ultracold molecules in the highly resonant regime *Phys. Rev. A* **87** 012709
- Mazzarella G, Giampaolo S M and Illuminati F 2006 Extended Bose–Hubbard model of interacting bosonic atoms in optical lattices: from superfluidity to density waves *Phys. Rev. A* **73** 013625
- Mazza L, Rizzi M, Lewenstein M and Cirac J I 2010 Emerging bosons with three-body interactions from spin-1 atoms in optical lattices *Phys. Rev. A* **82** 043629
- Meinert F, Mark M J, Kirilov E, Lauber K, Weinmann P, Daley A J and Nägerl H C 2013 Quantum quench in an atomic 1D ising chain *Phys. Rev. Lett.* **111** 053003
- Menotti C, Trefzger C and Lewenstein M 2007 Metastable states of a gas of dipolar bosons in a 2d optical lattice *Phys. Rev. Lett.* **98** 235301
- Mering A and Fleischhauer M 2011 Multiband and nonlinear hopping corrections to the 3D Bose–Fermi–Hubbard model *Phys. Rev. A* **83** 063630
- Mikelsons K and Freericks J K 2011 Density-wave patterns for fermionic dipolar molecules on a square optical lattice: mean-field-theory analysis *Phys. Rev. A* **83** 043609
- Mishmash R V and Carr L D 2009 Ultracold atoms in 1D optical lattices: mean field, quantum field, computation, and soliton formation *Math. Comput. Simul.* **80** 7322
- Mishra T, Pai R V, Ramanan S, Luthra M. S and Das B P 2009 Supersolid and solitonic phases in the 1D extended Bose–Hubbard model *Phys. Rev. A* **80** 043614
- Miyatake S, Inaba K and Suga S-i 2009 Color-selective Mott transition and color superfluid of three-component fermionic atoms with repulsive interaction in optical lattices *Physica C* **470** S916
- Montvay I and Münster G 1997 *Quantum Fields of a Lattice* (Cambridge: Cambridge University Press)
- Mott N F 1949 The Basis of the Electron Theory of Metals, with Special Reference to the Transition Metals *Proc. Phys. Soc. A* **62** 416
- Müller T, Fölling S, Widera A and Bloch I 2007 State preparation and dynamics of ultracold atoms in higher lattice orbitals *Phys. Rev. Lett.* **99** 200405
- Nasu K 1983 Extended Peierls–Hubbard model for 1D  $n$ -sites  $n$ -electrons system. 1 phase diagram by mean field theory *J. Phys. Soc. Japan* **52** 3865
- Ohmi T and Machida K 1998 Bose-Einstein Condensation with Internal Degrees of Freedom in Alkali Atom Gases *J. Phys. Soc. Japan* **67** 1822
- Ölschläger M, Kock T, Wirth G, Ewerbeck A, Morais Smith C and Hemmerich A 2013 Interaction-induced chiral  $p_x \pm ip_y$  superfluid order of bosons in an optical lattice *New J. Phys.* **15** 083041
- Ölschläger M, Wirth G and Hemmerich A 2011 Unconventional superfluid order in the f band of a bipartite optical square lattice *Phys. Rev. Lett.* **106** 015302
- Ölschläger M, Wirth G, Kock T and Hemmerich A 2012 Topologically induced avoided band crossing in an optical checkerboard lattice *Phys. Rev. Lett.* **108** 075302
- Ospelkaus C, Ospelkaus S, Humbert L, Ernst P, Sengstock K and Bongs K 2006a Ultracold Heteronuclear Molecules in a 3D Optical Lattice *Phys. Rev. Lett.* **97** 120402

- Ospelkaus S, Ospelkaus C, Wille O, Succo M, Ernst P, Sengstock K and Bongs K 2006b Localization of bosonic atoms by fermionic impurities in a 3D optical lattice *Phys. Rev. Lett.* **96** 180403
- Oxtoby O F and Barashenkov I V 2007 Moving solitons in the discrete nonlinear Schrödinger equation *Phys. Rev. E* **76** 036603
- Papacharalampous I E, Kevrekidis P G, Malomed B A and Frantzeskakis D J 2003 Moving solitons in the discrete nonlinear Schrödinger equation *Phys. Rev. E* **68** 046604
- Pasquiou B, Bismut G, Beaufils Q, Crubellier A, Maréchal E, Pedri P, Vernac L, Gorceix O and Laburthe-Tolra B 2010 Control of dipolar relaxation in external fields *Phys. Rev. A* **81** 042716
- Pasquiou B, Bismut G, Maréchal E, Pedri P, Vernac L, Gorceix O and Laburthe-Tolra B 2011 Spin relaxation and band excitation of a dipolar Bose–Einstein condensate in 2D optical lattices *Phys. Rev. Lett.* **106** 015301
- Pelinovsky D E, Kevrekidis P G and Frantzeskakis D J 2005 Stability of discrete solitons in nonlinear Schrödinger lattices *Physica D* **212** 1
- Phillips W D 1998 Nobel Lecture: Laser cooling and trapping of neutral atoms *Rev. Mod. Phys.* **70** 721
- Pietraszewicz J, Sowiński T, Brewczyk M, Lewenstein M and Gajda M 2013 Spin dynamics of two bosons in an optical lattice site: a role of anharmonicity and anisotropy of the trapping potential *Phys. Rev. A* **88** 013608
- Pietraszewicz J, Sowiński T, Brewczyk M, Zakrzewski J, Lewenstein M and Gajda M 2012 Two-component Bose–Hubbard model with higher-angular-momentum states *Phys. Rev. A* **85** 053638
- Pilati S and Troyer M 2012 Bosonic superfluid-insulator transition in continuous space *Phys. Rev. Lett.* **108** 155301
- Pitaevskii L P 1961 Vortex Lines in an Imperfect Bose Gas Sov. Phys.—JETP **13** 451
- Pitaevskii L and Stringari S 2003 *Bose–Einstein Condensation* (Oxford: Clarendon)
- Pollet L, Kollath C, Schollwock U and Troyer M 2008 Mixture of bosonic and spin-polarized fermionic atoms in an optical lattice *Phys. Rev. A* **77** 023608
- Przysiężna A, Dutta O and Zakrzewski J 2015 Rice–Mele model with topological solitons in an optical lattice *New J. Phys.* **17** 013018
- Radzhivsky L and Sheehy D E 2010 Imbalanced Feshbach–resonant Fermi gases *Rep. Prog. Phys.* **73** 076501
- Raghu S, Qi X L, Honerkamp C and Zhang S C 2008 Topological Mott insulators *Phys. Rev. Lett.* **100** 156401
- Rapp A, Deng X and Santos L 2012 Ultracold lattice gases with periodically modulated interactions *Phys. Rev. Lett.* **109** 203005
- Rapp A, Hofstetter W and Zaránd G 2008 Trionic phase of ultracold fermions in an optical lattice: A variational study *Phys. Rev. B* **77** 144520
- Rapp A, Zaránd G, Honerkamp C and Hofstetter W 2007 Color Superfluidity and “Baryon” Formation in Ultracold Fermions *Phys. Rev. Lett.* **98** 160405
- Rasmussen K O, Cai D, Bishop A R and Grønbech Jensen N 1997 Dynamics of nonlinear localized states on finite discrete chains *Phys. Rev. E* **55** 6161
- Regal C A, Ticknor C, Bohn J L and Jin D S 2003 Tuning p-wave interactions in an ultracold Fermi gas of atoms *Phys. Rev. Lett.* **90** 053201
- Robaszkiewicz S, Micnas R and Chao K A 1981 Thermodynamic properties of the extended Hubbard model with strong intraatomic attraction and an arbitrary electron density *Phys. Rev. B* **23** 1447
- Rossini D and Fazio R 2012 Phase diagram of the extended Bose–Hubbard model *New J. Phys.* **14** 065012
- Sachdev S 1999 *Quantum Phase Transitions* (Cambridge: Cambridge University Press)
- Safavi-Naini A, von Stecher J, Capogrosso-Sansone B and Rittenhouse S T 2012 First-order phase transitions in optical lattices with tunable three-body onsite interaction *Phys. Rev. Lett.* **109** 135302
- Sakmann K, Streltsov A I, Alon O E and Cederbaum L S 2009 Exact quantum dynamics of a bosonic josephson junction *Phys. Rev. Lett.* **103** 220601
- Sakmann K, Streltsov A I, Alon O E and Cederbaum L S 2010 Quantum dynamics of attractive versus repulsive bosonic josephson junctions: Bose–Hubbard and full-Hamiltonian results *Phys. Rev. A* **82** 013620
- Sakmann K, Streltsov A I, Alon O E and Cederbaum L S 2011 Optimal time-dependent lattice models for nonequilibrium dynamics *New J. Phys.* **13** 043003
- Salerno M 1992 A new method to solve the quantum Ablowitz–Ladik system *Phys. Lett. A* **162** 381
- Santos L and Pfau T 2006 Spin-3 chromium Bose–Einstein condensates *Phys. Rev. Lett.* **96** 1–4
- Schaff J F, Akdeniz Z and Vignolo P 2010 Localization–delocalization transition in the random dimer model *Phys. Rev. A* **81** 041604
- Schmidt K P, Dorier J and Läuchli A M 2008 Solids and supersolids of three-body interacting polar molecules on an optical lattice *Phys. Rev. Lett.* **101** 150405
- Schneider U, Hackermüller L, Will S, Best T, Bloch I, Costi T A, Helmes R W, Rasch D and Rosch A 2008 Metallic and Insulating Phases of Repulsively Interacting Fermions in a 3D Optical Lattice *Science* **322** 1520
- Schunck C H, Zwierlein M W, Stan C A, Raupach S M F, Ketterle W, Simoni A, Tiesinga E, Williams C J and Julienne P S 2005 Feshbach resonances in fermionic 6Li *Phys. Rev. A* **71** 045601
- Sengupta P, Pryadko L P, Alet F, Troyer M and Schmid G 2005 Supersolids versus Phase Separation in Two-Dimensional Lattice Bosons *Phys. Rev. Lett.* **94** 207202
- Si Q M, Rabello S, Ingerson K and Smith J L 2001 Locally critical quantum phase transitions in strongly correlated metals *Nature* **418** 804
- Singh M, Dhar A, Mishra T, Pai R V and Das B P 2012 Three-body on-site interactions in ultracold bosonic atoms in optical lattices and superlattices *Phys. Rev. A* **85** 051604
- Silva-Valencia J and Souza A M C 2012 Superfluid-to-Mott insulator transition of bosons with local three-body interactions *Eur. Phys. J. B* **85** 161
- Silva-Valencia J and Souza A M C 2011 First Mott lobe of bosons with local two- and three-body interactions *Phys. Rev. A* **84** 065601
- Soltan-Panahi P, Lühmann D S, Struck J, Windpassinger P and Sengstock K 2012 Quantum phase transition to unconventional multi-orbital superfluidity in optical lattices *Nat. Phys.* **8** 71
- Sowiński T 2014 One-dimensional Bose–Hubbard model with pure three-body interactions *Cent. Eur. J. Phys.* **12** 473
- Sowiński T 2012a Creation on Demand of Higher Orbital States in a Vibrating Optical Lattice *Phys. Rev. Lett.* **108** 165301
- Sowiński T 2012b Exact diagonalization of the one dimensional Bose–Hubbard model with local 3-body interactions *Phys. Rev. A* **85** 065601
- Sowiński T, Chhajlany R W, Dutta O, Tagliacozzo L and Lewenstein M 2013b Violation of the universality hypothesis in ultra-cold atomic systems
- Sowiński T and Chhajlany R W 2014 Mean-field approaches to the Bose–Hubbard model with three-body local interaction *Phys. Scr.* **2014** 014038
- Sowiński T, Dutta O, Hauke P, Tagliacozzo L and Lewenstein M 2012 Dipolar molecules in optical lattices *Phys. Rev. Lett.* **108** 115301
- Sowiński T, Łącki M, Dutta O, Pietraszewicz J, Sierant P, Gajda M, Zakrzewski J and Lewenstein M 2013a Tunneling-induced restoration of the degeneracy and the time-reversal symmetry breaking in optical lattices *Phys. Rev. Lett.* **111** 215302
- Stojanovic V M, Wu C, Liu W V and Das Sarma S 2008 Incommensurate superfluidity of bosons in a double-well optical lattice *Phys. Rev. Lett.* **101** 125301

- Strack R and Vollhardt D 1993 Hubbard model with nearest-neighbor and bond-charge interaction: exact ground-state solution in a wide range of parameters *Phys. Rev. Lett.* **70** 2637
- Straeter C and Eckardt A 2014 Orbital-driven melting of a bosonic MOTT insulator arXiv:1407.7421
- Struck J, Ölschläger C, Le Targat R, Soltan-Panahi P, Eckardt A, Lewenstein M, Windpassinger P and Sengstock K 2011 Quantum simulation of frustrated magnetism in triangular optical lattices *Science* **333** 996
- Struck J, Simonet J and Sengstock K 2014 Spin-orbit coupling in periodically driven optical lattices *Phys. Rev. A* **90** 031601
- Sun K, Liu W V, Hemmerich A and Sarma S D 2012 Topological semimetal in a fermionic optical lattice *Nat. Phys.* **8** 67
- Świsłocki T, Sowiński T, Brewczyk M and Gajda M 2011a Creation of topological states of a Bose-Einstein condensate in a square plaquette of four optical traps *Phys. Rev. A* **84** 023625
- Świsłocki T, Sowiński T, Pietraszewicz J, Brewczyk M, Lewenstein M, Zakrzewski J and Gajda M 2011b Tunable dipolar resonances and Einstein-de Haas effect in a  $^{87}\text{Rb}$ -atom condensate *Phys. Rev. A* **83** 063617
- Tagliacozzo L, Celi A, Orland P, Mitchell M W and Lewenstein M 2013a Simulation of non-abelian gauge theories with optical lattices *Nat. Commun.* **4** 2615
- Tagliacozzo L, Celi A, Zamora A and Lewenstein M 2013b Optical abelian lattice gauge theories *Ann. Phys.* **330** 160–91
- Thalhammer G, Theis M, Winkler K, Grimm R and Denschlag J H 2005 Inducing an optical Feshbach resonance via stimulated Raman coupling *Phys. Rev. A* **71** 033403
- Theis M, Thalhammer G, Winkler K, Hellwig M, Ruff G, Grimm R and Denschlag J H 2004 Tuning the Scattering Length with an Optically Induced Feshbach Resonance *Phys. Rev. Lett.* **93** 123001
- Tokura Y and Nagaosa N 2000 Orbital physics in transition-metal oxides *Science* **288** 462
- Tóth T A, Läuchli A M, Mila F and Penc K 2010 Three-sublattice ordering of the SU(3) Heisenberg model of three-flavor fermions on the square and cubic lattices *Phys. Rev. Lett.* **105** 265301
- Trefzger C, Menotti C, Capogrosso-Sansone B and Lewenstein M 2011 Ultracold dipolar gases in 2D optical lattices *J. Phys. B* **44** 193001
- Trombettoni A and Smerzi A 2001 Discrete Solitons and Breathers with Dilute Bose-Einstein Condensates *Phys. Rev. Lett.* **86** 2355
- Trombettoni A and Smerzi A 2003 Nonlinear tight-binding approximation for Bose-Einstein condensates in a lattice *Phys. Rev. A* **68** 023613
- Trotzky S, Chen Y A, Flesch A, McCulloch I, Schollwöck U, Eisert J and Bloch I 2012 Probing the relaxation towards equilibrium in an isolated strongly correlated one-dimensional Bose gas *Nat. Phys.* **8** 325
- Troyer M and Wiese U J 2005 Computational complexity and fundamental limitations to fermionic quantum Monte Carlo simulations *Phys. Rev. Lett.* **94** 170201
- Uehlinger T, Jotzu G, Messer M, Greif D, Hofstetter W, Bissbort U and Esslinger T 2013 Artificial graphene with tunable interactions *Phys. Rev. Lett.* **111** 185307
- van Oosten D, van der Straten P and Stoof H T C 2001 Quantum phases in an optical lattice *Phys. Rev. A* **63** 053601
- Vignolo P, Akdeniz Z and Tosi M P 2003 Transmittivity of a Bose-Einstein condensate on a lattice: interference from period doubling and the effect of disorder *J. Phys. B: At. Mol. Opt. Phys.* **36** 4535
- Voigt A, Taglieber M, Costa L, Aoki T, Wieser W, Hänsch T W and Dieckmann K 2009 Ultracold heteronuclear Fermi-Fermi molecules *Phys. Rev. Lett.* **102** 020405
- Wall M L and Carr L D 2013 Dipole-dipole interactions in optical lattices do not follow an inverse cube power law *New J. Phys.* **15** 123005
- Will S, Best T, Schneider U, Hackermüller L, Lühmann D S and Bloch I 2010 Time-resolved observation of coherent multi-body interactions in quantum phase revivals *Nature* **465** 197
- Windpassinger P and Sengstock K 2013 Engineering novel optical lattices *Rep. Prog. Phys.* **76** 086401
- Wirth G, Ölschlägel M and Hemmerich A 2010 Evidence for orbital superfluidity in the P-band of a bipartite optical square lattice *Nat. Phys.* **7** 147
- Wiese U-J 2013 Ultracold quantum gases and lattice systems: Quantum simulation of lattice gauge theories *Ann. der Phys.* **525** 777–96
- Wu C, Bergman D, Balents L and Das Sarma S 2007 Flat bands and Wigner crystallization in the honeycomb optical lattice *Phys. Rev. Lett.* **99** 070401
- Wu C 2008b Orbital ordering and frustration of p-band Mott insulators *Phys. Rev. Lett.* **100** 200406
- Wu C 2009 Unconventional Bose-Einstein condensations beyond the “No-node” theorem *Mod. Phys. Lett. B* **23** 1
- Xiong B and Fischer U R 2013 Interaction-induced coherence among polar bosons stored in triple-well potentials *Phys. Rev. A* **88** 063608
- Zhang J, van Kempen E G M, Bourdel T, Khaykovich L, Cubizolles J, Chevy F, Teichmann M, Tarruell L, Kokkelmans S J J M F and Salomon C 2004 P-wave Feshbach resonances of ultracold  $^6\text{Li}$  *Phys. Rev. A* **70** 030702
- Zhao E and Liu W 2008 Orbital order in Mott insulators of spinless p-band fermions *Phys. Rev. Lett.* **100** 160403
- Zhou K, Liang Z and Zhang Z 2010 Quantum phases of a dipolar Bose-Einstein condensate in an optical lattice with three-body interaction *Phys. Rev. A* **82** 013634
- Zohar E, Ignacio Cirac J and Reznik B 2013 Cold atom quantum simulator for SU(2) Yang-Mills lattice gauge theory *Phys. Rev. Lett.* **110** 125304
- Zöllner S, Meyer H D and Schmelcher P 2008 Few-boson dynamics in double wells: from single-atom to correlated pair tunneling *Phys. Rev. Lett.* **100** 040401
- Zurek W H 2003 Decoherence, einselection, and the quantum origins of the classical *Rev. Mod. Phys.* **75** 715
- Zwerger W 2003 Mott-Hubbard transition of cold atoms in optical lattices *J. Opt. B* **5** S9